Mathematical modeling of liver tumor

William Weens

Mathematical modeling of liver tumor

THÈSE DE DOCTORAT

présentée et soutenue publiquement le 21 septembre 2012
pour l'obtention du grade de

Docteur de l'Université Pierre et Marie Curie

Spécialité Mathématiques Appliquées

par

William WEENS

Composition du jury

Rapporteurs :	Pr. Mark A.J.CHAPLAIN	
	Pr. Vitaly VOLPERT	
Examinateurs :	Pr. Benoît PERTHAME	Président
	Pr. Dirk DRASDO	Directeur de thèse
	Pr. Bertrand MAURY	
	Pr. Pierre NASSOY	

Résumé

Comme démontré récemment pour la régénération du foie après un dommage causé par intoxication, l'organisation et les processus de croissance peuvent être systématiquement analysés par un protocole d'expériences, d'analyse d'images et de modélisation [43]. Les auteurs de [43] ont quantitativement caractérisé l'architecture des lobules du foie, l'unité fonctionnelle fondamentale qui constitue le foie, et en ont conçu un modèle mathématique capable de prévoir un mécanisme jusqu'alors inconnu de division ordonnée des cellules. La prédiction du modèle fut ensuite validée expérimentalement. Dans ce travail, nous étendons ce modèle à l'échelle de plusieurs lobules sur la base de résultats expérimentaux sur la carcinogénèse dans le foie [15]. Nous explorons les scénarios possibles pouvant expliquer les différents phenotypes de tumeurs observés dans la souris. Notre modèle représente les hépatocytes, principal type de cellule dans le foie, comme des unités individuels avec un modèle à base d'agents centré sur les cellules et le système vasculaire est representé comme un réseau d'objets extensibles. L'équation de Langevin qui modélise le mouvement des objets est calculée par une discrétisation explicite. Les intéractions mécaniques entre cellules sont modélisées avec la force de Hertz ou de JKR. Le modèle est paramétré avec des valeurs mesurables à l'échelle de la cellule ou du tissue et ses résultats sont directement comparés avec les résultats expérimentaux.

Dans une première étape fondamentale, nous étudions si les voies de transduction du signal de Wnt et Ras peuvent expliquer les observations de [15] où une proliferation instantannée dans les souris mutées est observée seulement si 70% des hépatocytes sont dépourvues d'*APC*. Dans une deuxième étape, nous présentons une analyse de sensibilité du modèle sur la rigidité de la vasculature et nous la mettons en relation avec un phenotype de tumeur (observé expérimentalement) où les cellules tumorales sont bien différentiées. Nous intégrons ensuite dans une troisième étape la destruction de la vasculature par les cellules tumorales et nous la mettons en relation avec un autre phénotype observé expérimentalement caractérisé par l'absence de vaisseaux sanguins. Enfin, dans la dernière étape de notre étude nous montrons que des effets qui sont détectables dans les petits nodules tumoraux et qui reflètent les propriétés des cellules tumorales, ne sont plus présents dans la forme ou dans le phenotype des tumeurs d'une taille excédant la moitié de celle d'un lobule.

Abstract

As recently demonstrated for liver regeneration after drug-induced damage, organization and growth processes can be systematically analyzed by a process chain of experiments, image analysis and modeling [43]. The authors of [43] were able to quantitatively characterize the architecture of liver lobules, the repetitive functional building blocks of liver, and turn this into a quantitative mathematical model capable to predict a previously unrecognized order mechanism. The model prediction could subsequently be experimentally validated. Here, we extend this model to the multi-lobular scale, guided by experimental findings on carcinogenesis in liver [15]. We explore the possible scenarios leading to the different tumor phenotypes experimentally observed in mouse. Our model considers the hepatocytes, the main cell type in liver, as individual units with a single cell based model and the blood vessel system as a network of extensible objects. Model motion is computed based on explicit discretized Langevin equation and cell interactions are either Hertz or JKR forces. The model is parameterized by measurable values on the cell and tissue scale and its results are directly compared to the experimental findings.

In a fundamental first step we study if Wnt and Ras signaling pathways can explain the observation of [15], that instantaneous proliferation in mutated mice can only be observed if around 70% of the hepatocytes become *APC* depleted. In a second step, we show a sensitivity analysis of the model on the vessel stiffness and relate it to a tumor phenotype (experimentally observed) where the tumor cells are well differentiated. We integrate in a third step the destruction of vasculature by tumor cells to relate it to another experimentally observed tumor phenotype characterized by the absence of blood vessels. Finally, in the last step we show that effects that are detectible for small tumor nodules and reflect properties of the tumor cells, are not reflected in the tumor shape or phenotype at tumor sizes exceeding half of the lobule size.

Contents

Introduction

> "Biological experiments are expensive and depend on many parameters that are mostly difficult to control and test in isolation. As a complementary method, mathematical modeling and *in silico* experiments are a good candidate to help explore the behavior of the individual tissue cells along with investigating their response to environmental cues" [47]

What is Systems Biology ?

Systems biology is a new branch of science that wants to embed a not so new idea: "the whole is more than the sum of its parts". Aristotle in his *Metaphysics* has already developed this idea. Life is a good example to illustrate this concept. Intuitively, living organisms seem to be more than a sum of atoms. Some properties of life are not contained in atoms but emerge from complex interactions. This is what systems biology aims at understanding: emergent properties. To study such complex systems with all possible interactions, systems biology requires gathering knowledge and skills from many disciplines. A new paradigm has been suggested to face this task: Holism. Holism purpose is to include in the study the different interactions, for different scales, from different scientific fields. This new methodology is opposed to the traditional reductionist method theorized by René Descartes [53, 77]. Reductionism consists in splitting problems in small parts supposed being solvable independently. Reductionism opponents think that unlikely this method is unable to catch global properties coming from the union of small sub-problems and thus miss the emergent properties. In other words, reductionism is criticized because it takes apart and over simplifies. This simplification is believed to fail with complex systems.

Computers are stupid

Holism suggests thinking differently in order to embrace the problems but does not give so far a clear description to do it. Denis Noble, one of the pioneers in systems biology gave a list of holistic principles for systems biology [67]. These principles need to be interpreted in order to be applied in daily scientific work especially if one works with computers. Today, no programming language exists for the holistic point of view. Computers are stupid and they need to reduce problems even more than it is needed for the human brain [10].

Computer programs represent reductionism approach at its climax: numbers are truncated, memory, time and space are finite and discretized, and operations must be ordered – two actions are never performed at the same time, not like in reality. One immediate benefit from this imposed and drastic reduction is that programs are logically speaking consistent. From the results of simulations, causes and consequences may be logically connected and classified more easily because the translation of a model into a program is rigorous – computers cannot deal with ambiguities. Moreover computers don't prevent models to exhibit emergent properties even with very simple programs [12]. Finally, we may add an authority argument and recall that holism has been developed recently and does not benefit from success of its reductionist concurrent that helped science to build its actual knowledge since centuries. For those reasons, we decided to work traditionally even if the field is emergent. Hoping that we would not bore the reader hungry of brilliant novelties, we think we chose the safer path for scientific work.

What we know about reality

The following discussion about perception of reality is not proper to our scientific domain but we think it is important to emphasize how blind systems biology is to the reality problems it deals with. The main reason of the distance between reality and perception comes from the nature of observables. A single cell may have dozens of thousands of proteins interacting with each other.

Speaking about huge numbers, John D. Barrow in [5] suggests talking not about astronomic numbers anymore but biological numbers. For instance, he shows by a little computation that a neuron may have possibly interactions with 10^{180} other neurons remembering that the number of atoms in the universe is 10^{80}. This vertiginous figure explains the huge variability that exists in experimental biology. Since the end of the 20^{th} century, scientists are equipped with a new weapon: computers and their increasing computation power. Even if computational power will always remain insufficient to reach the numbers quoted by Barrow, computers proved their ability to help in classifying huge amount of data. In order to get a chance of understanding so complex systems, a large quantity of results should be produced. The variability of the experimental data should be smoothed by the large amount and their systematical analysis. Particular cases and new concepts should emerge from the contradictory data. In other words, quantity is supposed to counter complexity of life. Systematic analysis has become possible thanks to computers and systems biology as an inter-disciplinary field takes advantage of this tool. Probably, it is the way around and we could ask if computing power itself did not create systems biology? At least, computers have made systems biology feasible.

How to deal with complex systems?

By simulating situations with different assumptions, it is possible to test hypotheses, to discard some and keep the more plausible ones. Simulations can help directly to understand complex systems but also indirectly by guiding experimentalist in the multitude

(a) Reality can be complicated and complex. Most of the time, we could get only truncated screenshots of it from different situations.

(b) Experiments can give only a certain resolution of this reality which starts already to mislead the analysis

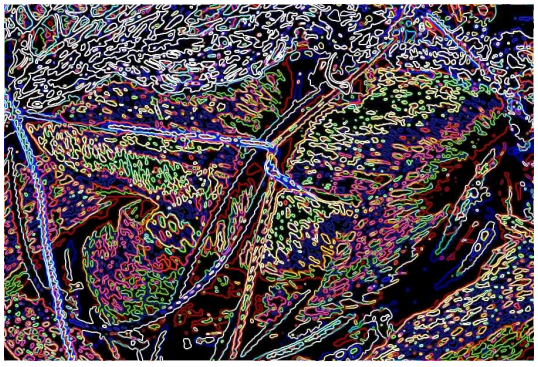

(c) Mathematical modeling or idealization even fully detailed cannot be more than an approximation of the observations.

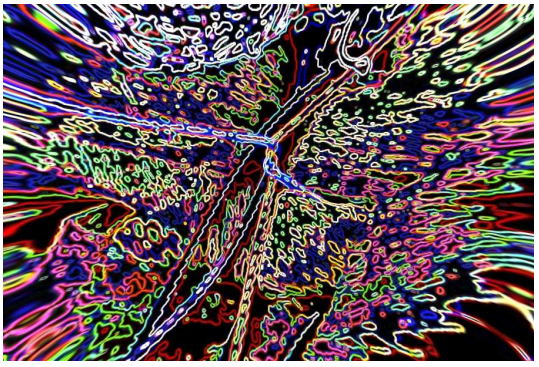

(d) Simulation deforms the model by the numerical assumptions needed for the computation.

Figure 1: Schematic illustration of the reality seen through the eye of a modeler. If inputs of the model were images of entwined fisher nets, we schematize what would be the model idealization of it. (Image from photo-libre.fr freely distorted)

of paths they may choose. Simulations should be seen as catalyzers for understanding faster real cases. Simulations reduce the number of possibilities without need for additional experiments. Thanks to this virtual tool, Science saves of course time and money but also the lives of animals[1]. The field is new but already yielded a substantial amount of success. We did not start from scratch but walked in the steps of our predecessors. The model presented in this work have been largely inspired by others, all applied to biological problems [29, 27, 68, 73, 82, 2]. In particular, the first stone of the modeling of angiogenesis can be find in [4] that largely inspired our way to consider the vascular network. Interested reader about angiogenesis can refer to [63, 61], also important papers in the mathematical modeling of angiogenesis. We especially refer to previous work of our team and published in [43]. For those reasons, we selected the simulation approach to deal with complex systems. This work invested a lot of effort to build a tool capable to

[1] all important issues to get European founds

properly simulate different models.

The final simulation result of one model is not enough to provide any reasonable argument to make conclusions about reality (see fig. 1). The only way is to proceed through numbers and repetitions. Iterations over experiments and simulations eliminate artifacts, dissociate particular and general, and distinguish errors and fluctuations of the measurements. Only after several iterations can the modeler emphasize relevant mechanisms and suggest new experiments to demonstrate his purpose. The loop process can be summarized by the following scheme (see fig. 2).

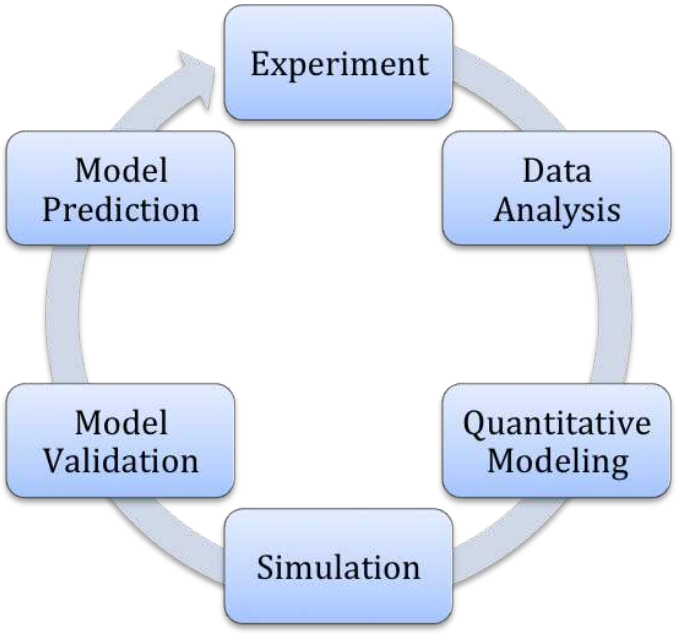

Figure 2: Process loop: A pilot experiment starts the chain. This experiment leads, at the end of the cycle, to new experiments to confirm the explanation. Most of the time, predictions are open. Several possibilities still exist. After some iterations of this process chain, the number should decrease to lead to reliable explanations of the experiment.

We described in details the methodology of our work and some parts can be trivial. As a new and inter-disciplinary branch of science, the methodology is still under development and we decided to emphasize on this part of our work because organization in systems biology is needed not only to be efficient but also simply to be able to accomplish our task.

Organization of the thesis

The work presented here is at the crossroads of many scientific domains. To help the reader, we supplemented this document with a glossary and an appendix.

The first chapter presents a brief review of Agent-Based Models (ABMs) to make the reader familiar with this model concept (a complete and recent review can be found in [50]). We present the assumptions that led to the physical and mathematical framework of the model. We introduce the model by explaining the choices (motivations and references) that led to adapt the model that way from the validated model published in [44, 41]. We describe the cell shape, motion, growth and death control, interactions with other cells, active movement, angular momentum and molecular transport.

In the second chapter, we describe algorithms and necessary components to simulate the agent-based model presented in the first chapter. Due to the complexity of the problem, many challenges had to be faced and the implementation occupied a large part of the working time. Technical description is developed in order to be reproducible: program language, libraries, algorithms, numerical schemes, parallelization and solvers. We show benchmarks that compare program efficiency of the sequential version to the parallel version. The choice of the programming language was guided by our needs, which are:

- Modularity: the model should be open to extensions without a full re-organization of the code.
- Collaborative: the code should be readable and understandable rapidly by collaborators.
- Fast: the simulations deal with a large number of elements. The program must be fast enough (optimized compilers, optimized algorithms).
- Robustness: A debugging method should be applicable on the code to ensure a minimum of implementation error.

The aims of the simulator are to compute the equations of the model with an initial input and to output and analyze the results. Many functions that simulate or analyze the model are too trivial and can be straight-forward programmed even though the time to include them in a code can be long. We present selected algorithms and numerical methods we used to compute the Langevin equation: numeral issues, numerical schemes, main algorithm, parallel sparse matrix solver and parallel contact detection.

In the third chapter, we present the main application of the model: the liver cancer. Despite the large efforts over the last decades, cancer is a leading cause of death. The complexity of the disease has now led to requests of support to the mathematical community [28]. Colnot et al. [15] have developed an interesting liver *in vivo* cancer mouse model. The model could explain some aspects of the human liver cancer but also pointed a number of questions. What could explain that hepatocyte proliferation is triggered only if 70% of the cells are *APC* depleted? What could explain that *APC* depletion leads to two distinct tumor phenotypes? How could distinguish different phenotype in early development? We adapted the model introduced above to address these questions by studying

the possible influence of different mechanisms on carcinogenesis by simulations with an *in silico* liver model. We detail the biological information necessary for this application, namely: the liver cancer, the mouse model, its data and questions, and the model specificities that we had to include to mimic possible scenarios of carcinogenesis in liver. This chapter also described additional model specifications and assumptions. We used the data extracted in [42] to build a representative sample of lobules. We describe the novelties introduced and split the results in five sections: In the first section, we present the results of an integrated model of the Wnt and β-catenin signal transduction pathways into the multi-cellular model. We perform the integration into a monolayer and choose the boundary condition in analogy to those in a liver lobule. In a fundamental first step we study if Wnt and Ras signaling pathways can explain the observation of [15], that instantaneous proliferation in $\mathrm{Apc}^{\mathrm{lox/lox}}$ mice can only be observed if around 70% of the hepatocytes become $\mathrm{Apc}^{-/-}$. The liver functions are dependent on the liver tissue organization. In this tissue, the vasculature plays a crucial role. In the second result section, we show a sensitivity analysis of the model on the vessel stiffness and relate it to the well-differentiated phenotype. In the mouse model, biologists observed poorly differentiated tumor after *APC* cell depletion. This tumor phenotype is characterized by the absence of blood vessels. We integrated this information by including destruction of vasculature by tumor cells and performed a sensitivity analysis that is shown in the third section. In above sections 2 and 3, we studied the emergence of different tumor phenotypes. We did not, however, study any mechanism affecting tumor symmetry, and how the tumor phenotype is expected to vary with tumor size beyond a nodule size. In the rat experimental model where tumors can be initiated in a controlled way, small tumors can be observed while in human patients at the time point of clinical manifestation, tumors are usually of centimeter size. The tumor shape at tumor initiation may reflect important information on the underlying mechanism. Hence it is important to know if effects that are detectible for small tumor nodules and reflect properties of the tumor cells, may still be reflected in the tumor shape or phenotype at tumor sizes exceeding the distance between the central and periportal vein. We show in the fourth section simulations focusing on those aspects. Finally in the last result section, we present simulations after various stimulation patterns. The possible number of combinations of assumptions is too large to be tested in its entirety. However, we performed many simulations to explore the most realistic configurations. We presented in previous sections the most concluding ones. To obtain them, many simulations had to be performed. The results presented in this section is a selection of results that guided the thinking and allowed us to present a straight forward reasoning and also to justify some affirmations in the argumentation line. Despite their modest influence on tumor growth, the stimulation patterns presented below permitted to understand the relevant mechanisms and discard the ones with small impact. Moreover, they obliged us to find new measurements and new strategies to reach the goals of the previous sections. We present the results here to show that our exploration was not restrained to only few mechanisms but covered a large span of possibilities.

The last chapter summarizes the results and present perspectives and other current applications of the model.

Chapter 1

Model description

La différence entre les théories des biologistes et celles des mathématiciens sur la biologie est la même qu'entre les théories d'éducation des enfants pour les personnes qui ont des enfants et ceux qui n'en ont pas.

IN TÜBINGEN, Sabine Colnot

1.1 Model framework

In brief:
This section presents briefly agent-based models to make the reader familiar with this model concept. A complete and recent review can be found in [50]. We introduce here the model (with equations) by explaining the choices (motivations and references) that leaded to adapt the model that way from validated model published in [44, 41].

1.1.1 Agent-based models

The biological problem we are interested in and that we present in a further chapter, takes place at the cell scale. In particular, its purpose is to understand the differences between several cell types where the differences are physical cell properties. Agent-based models (ABM) offer numerous advantages over continuum models for this type of problem. ABM are also called individual-based models. We prefer naming our objects *agents* because they are not individual neither indivisible (as etymology of "individual" suggests). Continuum models use locally averaged quantities (like cell density for instance) where

the discrete nature of the problems scaled at cell size becomes critical. Formally, it should be possible to translate most of ABM in continuum models for scales that are greater than cell scale. Even though, the translation remains a complicated issue [57].

ABM modeling nature – so called *bottom-up* approach – is such that each assumption on physics, biology or social can be explicitly incorporated. *Let there be the light*, and the light is. Naming the process, is modeling the process. ABM approach is intuitive and pertinent for cell scale model. It is naturally designed to study the impact of individual properties on populations. This is an enormous advantage to communicate with people from other disciplines. For instance, in biology, this is particularly useful when the question is to relate one single modification (in genotype or phenotype) in individual cell to the full population, which is an important aspect in cancer research.

The model is not the final aim, outputs are. The easiness with which a model can be exchanged, modified and simulated is important in the choice of the model type. Unfortunately, nothing comes for free and there is a price to pay for ABM. To be able to simulate properly a phenomenon, agent properties and interactions have to be known and modeled in detail. The more specific the situation is to simulate the more has to be included in the model. For instance, a simple model of cell motion needs a lot of information: model for the cell surface, cell deformation, cell/cell friction, etc. Comparatively, continuum approach would mean everything into a couple of equations. Other difficulties encountered by agent-based modelers are the time to program a valid simulator and in the case of a large number of agents the simulation time and its CPU time consumption. Coding optimization and using costly computer resources consumes a large part of the time (some figures about this issue are presented in the next chapter). Despite these aspects, the cost in time, in money and definitely in animal lives remains usually and easily under the cost of experiments.

Once the choice to use ABM is made, a wide range of possibilities is still available for the modeler. We distinguish two main families that cell-based model may belong to depending on: (i) if cell morphology is modeled, most of the time by sub-cellular elements and (ii) if agent are lattice-free or not, i.e. if model elements can move continuously or discretely in space. For further readings on the different models, see [20] and more recently [47] [1]. Every combination exists with its advantages and drawbacks, for instance Pott's models [34] include the morphology of the cell on lattice sites while [17] use deformable particles to off-lattice cells. Precise morphology description of the cell is useful if one is interested in cell sorting, whereas off-lattice model are practical to model physical forces among the agents [25]. For the latter reason and the liver model requirements, our model evolved naturally toward an off-lattice model at which we added an important mechanism for liver cells: we refined the cell morphology that is represented by two objects during the mitosis phase – when the cell divides. Moreover, we based our choice on validation in vitro in [44] and especially in vivo in the liver in [43].

[1] The authors of [47] summarized different cell-based models. A correction needs to be done on their review: cell-based Langevin dynamics does give access to biomechanics behavior. It is precisely the purpose of this model type as it will be shown later

1.1.2 Physical and mathematical model description

In brief:
We present here the assumptions that led to the physical and mathematical framework of the model. We describe the cell shape, motion, growth and death control, interaction with other cells, active movement, angular momentum and molecular transport.

Cell shape

In the model, a cell is represented by either a sphere or two spheres when it is in the mitosis phase (the dividing phase). We call each sphere of the dividing cell a sub-element, which gives to the cell a dumb-bell like shape. Each cell is assumed to be spherical after division with diameter L. To grow, a cell first doubles its volume (linearly in time) and then deforms into a dumb-bell during the mitosis phase. As the distance between the two parts of the dumb-bell increases, the radius of each sub-element decreases. Finally, the dumb-bell splits into two distinct cells with diameter L (see schematic illustration 1.1). This makes the model hybrid between a purely cell-based model and a subcellular-based model where the cell can really adopt different shapes. Here with two sub-elements during the mitosis, the cell is not symmetric. This imposes to define the initial axis of division. In the applications, this choice appeared to be crucial to determine tissue organization.

In the case of apoptosis, a special type of cell death (see below), a cell receives a signal and commits suicide rapidly compared to the cell-cycle duration. In about 30 minutes, the cell radius decreases to one third of the normal cell radius to become a so-called apoptotic core that is removed later. The model includes apoptosis, which needs additional parameters: apoptosis duration, removal duration, apoptotic core radius.

Cell growth and death control

In the model, each cell possesses its own cell cycle duration – the time needed by the cells to grow and divide. The cell-cycle duration is a random number selected with a Gaussian distribution probability around the biological mean value (generally cells divide in about 24 hours). This choice is justified by experiments where cell proliferation is desynchronized after few divisions. Cells have the ability to feel their environment through their cytoskeleton [45] and control their proliferation rates respect to the pressure they undergo on their surface. Experiments by [40] suggest that cells can be triggered to enter cell cycle arrest by external pressure. The model includes this cell capability. The cell decision to divide depends on the pressure exerted on the cell surface. In our model, we mainly modeled this dependency with pressure checkpoints rather than with nutrient control (liver is very well vascularized, so we assumed no nutrient limitation in this environment). Cell pressure is compared to a threshold value. If the cell pressure is less than this value then the cell enters its cell-cycle and starts to divide. Different functions and inputs can be used for instance in 3.2, the decision depends on regulatory factors. Figure 1.2 is the schematic

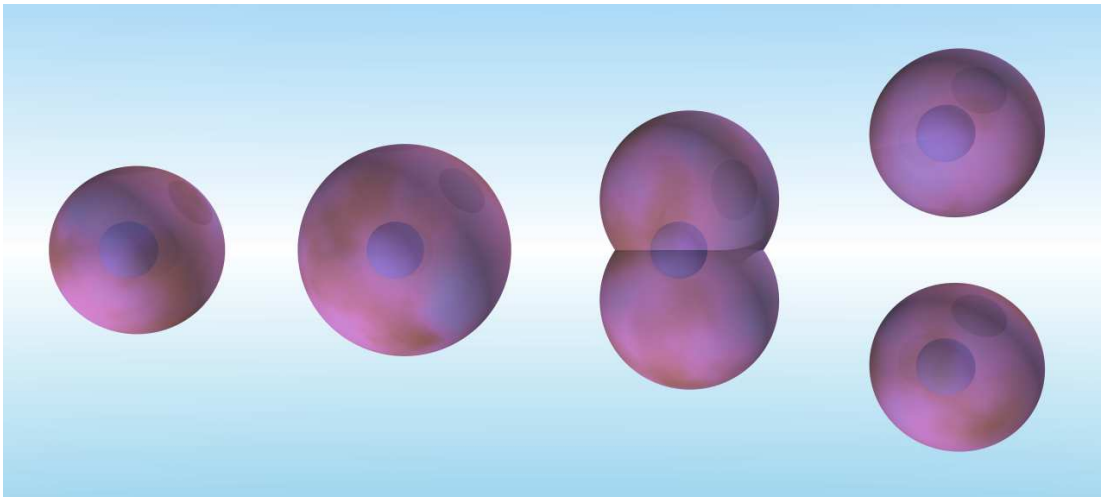

Figure 1.1: Division process: illustration of the cell division algorithm. A cell maintains its spherical shape during the first phase of the growth. During the mitosis, the sphere deforms into a dumb-bell to finally splits in two cells.

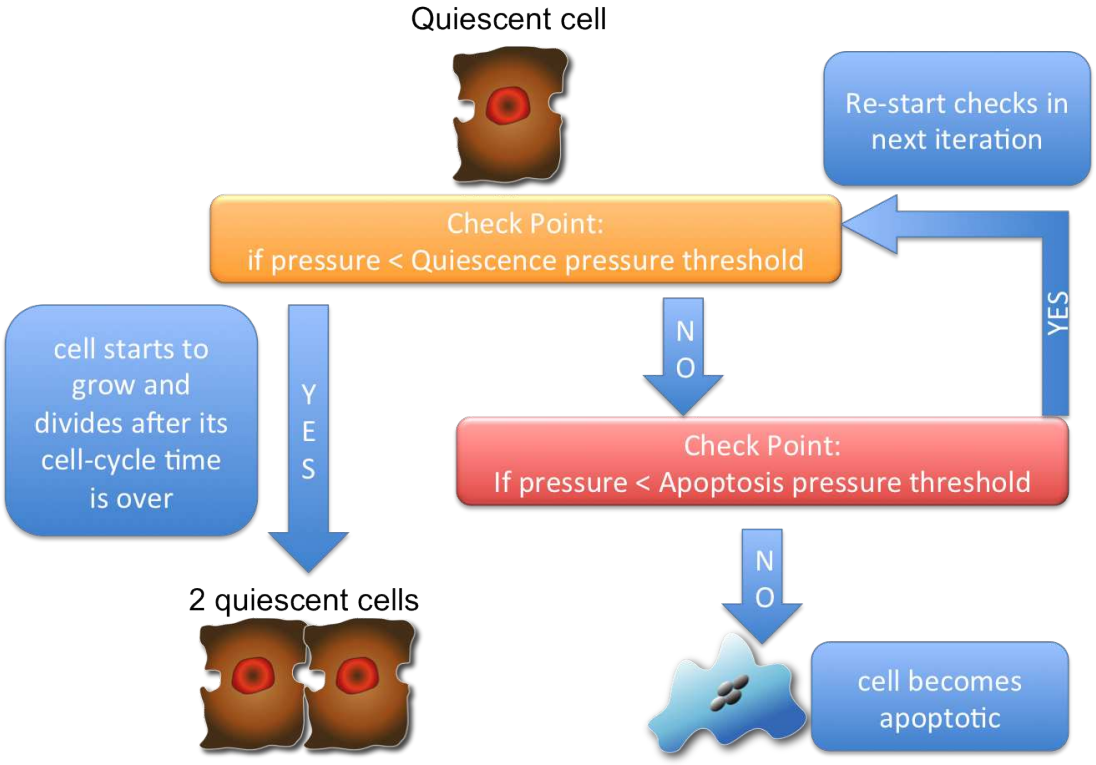

Figure 1.2: Growth control: We mainly used this growth control. After division, the cell is quiescent. Depending on the local pressure. The cell decides its cell-cycle entrance. If the pressure is too high, it could enter apoptosis.

illustration of the model used in liver applications. A cell can start to grow only if its pressure is below a certain threshold and can die (undergoes apoptosis, in biological denomination for this type of death, necrosis is not modeled) only if the pressure is above a certain threshold. These thresholds are called respectively biomechanical force for inhibition (BFI) and biomechanical force for apoptosis (BFA) (see pressure computation 1.1.3) When the cell shape is a dumb-bell: the pressure is the sum of the pressure exerted by external bodies on both sub-elements. We tested two models for the pressure measurement: we sum the positive pressure or positive and negative pressure (due to adhesion).

Cell Motion

As each cell is modeled individually, the motion is represented by a system of equations, one for each cell. When the cell is in a division process (dumb-bell shape represented by 2 spheres), the cell movement is driven by the sum of the forces on its two spherical sub-elements. When cells are not in a division process (spherical shape), the cell movement is driven by one sub-element. The sub-element movement indexed i is summarized in the following Langevin equation:

$$M_i \frac{d\underline{v}_i}{dt} + \underline{\underline{\Gamma}}_{cs} \frac{A_i^{cs}}{A_i} \underline{v}_i + \sum_j \underline{\underline{\Gamma}}_{cc} \frac{A_{ij}}{A_i} (\underline{v}_i^{ij} - \underline{v}_j^{ij}) + \underline{\underline{\gamma}}_r^{cs} \underline{\Omega}_i = \int_0^t K_m(t-t') \underline{v}(t') dt' + \sum_j \underline{F}_{ij} + \underline{F}_i^{\text{active}} \tag{1.1}$$

- Notation: underlined variables denote vectors, double underlined denote tensors, scalar variables are not underlined. Subscript or superscript index i or j allways refer to cell i or j.
- $\underline{v}_i$ is the speed of cell i, M_i its mass and so the term $M_i \frac{d\underline{v}_i}{dt}$ is the cell inertia.
- $\underline{\underline{\Gamma}}_{cs}$ is the friction tensor with the medium
- $\underline{\underline{\Gamma}}_{cc}$ is the cell-cell friction tensor.
- $\underline{\underline{\Gamma}}_{cs} \frac{A_i^{cs}}{A_i} \underline{v}_i$ is the cell friction force with the medium. $\frac{A_i^{cs}}{A_i}$ the contact area fraction of the cell with the substrate.
- $\sum_j \underline{\underline{\Gamma}}_{cc} \frac{A_{ij}}{A_i} (\underline{v}_i^{ij} - \underline{v}_j^{ij})$ is the cell/cell friction force where $\underline{v}_i^{ij} = \underline{v}_i + \underline{\Omega}_i \times \underline{r}_i^{ij}$ denotes the velocity of the cell i at the contact point between cells i and j, $\underline{r}_i^{ij}$ the vector from the center of mass of cell i to the contact area between cells i and j.
- $\underline{\underline{\gamma}}_r^{cs} \underline{\Omega}_i$ is the angular momentum.
- $\int_0^t K_m(t-t') \underline{v}(t') dt'$ is a memory term on individual history.
- $\sum_j \underline{F}_{ij}$ is the sum of pairwise forces with other cells.
- $\underline{F}_i^{\text{active}}$ is a random force that mimics the active cell movement.

This equation can be simplified with the following assumptions:

- Inertia term: $M_i \frac{d\underline{v}_i}{dt}$ can be neglected because the movement is dominated by friction.
- We drop the memory term: $\int_0^t K_m(t-t')\underline{v}(t')dt'$ because time scale is large compared to cell speed memory.

The equation becomes:

$$\underline{\underline{\Gamma}}_{cs}\frac{A_i^{cs}}{A_i}\underline{v}_i + \sum_j \underline{\underline{\Gamma}}_{cc}\frac{A_{ij}}{A_i}(\underline{v}_i^{ij} - \underline{v}_j^{ij}) + \underline{\underline{\gamma}}_r^{cs}\underline{\Omega}_i = \sum_j \underline{F}_{ij} + \underline{F}_i^{\text{active}}$$

We assume the substrate to be a homogeneous and isotropic viscous medium, which leads to take for cell-substrate (or sub-element/substrate) friction the Stokes equation for spheres (see [18, 21]): $\underline{\underline{\Gamma}}_{cs} = (6\pi\eta_0 r_i)\underline{\underline{I}}$ where $\underline{\underline{I}}$ is the unit tensor, r_i the sub-element radius and η_0 is the medium viscosity.

Cell-cell interaction

In [14], the authors show that attraction and repulsion between two cells can be modeled by an interaction energy V_{ij} taken from the Johnson-Kendall-Roberts (JKR) model [49] if the cytoskeleton is not disrupted – i.e. for small cell deformation. The JKR model describes the pairwise interaction between homogeneous isotropic elastic adhesive spheres (see review in [6]) and it takes into account hysteresis. Indeed, cell contact history is important. Once cells are in contact, it requires energy to detach them from each other (see figure 1.3 and 1.4). Thus:

> "The JKR model directly includes adhesion and relates the contact area to the elastic material properties and adhesion strength." [43]

Let's call F_{ij}^{JKR} the JKR force between cells i and j. We denote d_{ij} the distance between the centers of i and j. R_i, R_j, E_i, E_j,ν_i and ν_j, the respective radius, Young moduli and Poisson ratio of the cells. γ is a parameter that represents the adhesion strength. If $\gamma = 0$, the force can only be repulsive and is exactly the Hertz model [56]. We denotes $\delta = R_i + R_j - d_{ij}$, $\frac{1}{R_{ij}} = \frac{1}{R_i} + \frac{1}{R_j}$, $\frac{1}{E_{ij}} = \frac{3}{4}\left(\frac{1-\nu_i^2}{E_i} + \frac{1-\nu_i^2}{E_j}\right)$. Finally, the JKR force is implicitly given by the following relations:

$$\delta = \frac{a^2}{R_{ij}} - \sqrt{\frac{16\pi\gamma a}{3E_{ij}}} \tag{1.2}$$

$$a^3 = \frac{2R_{ij}}{E_{ij}}\left(F_{ij}^{JKR} + 3\pi\gamma R_{ij} + \sqrt{6\pi\gamma R_{ij}F_{ij}^{JKR} + (3\pi\gamma R_{ij})^2}\right) \tag{1.3}$$

Remarks:

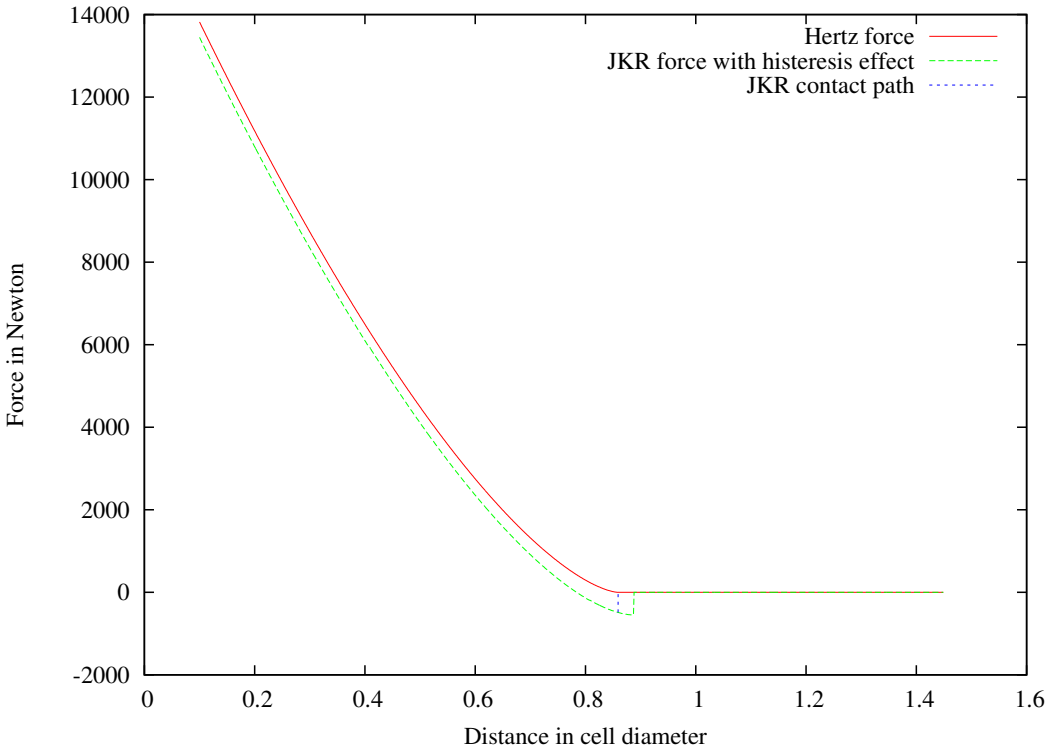

Figure 1.3: JKR force: Herzt and JKR force are qualitatively equivalent for elastic bodies in contact. JKR force models the adhesion and the histeresis effect. When bodies touch each other they adhere to each other (JKR contact path). Once in contact, the rupture of the adhesion occurs at a distance greater than the contact distance. This mimics the histeresis effect and relies on the contact history of the two adhesive elastic bodies.

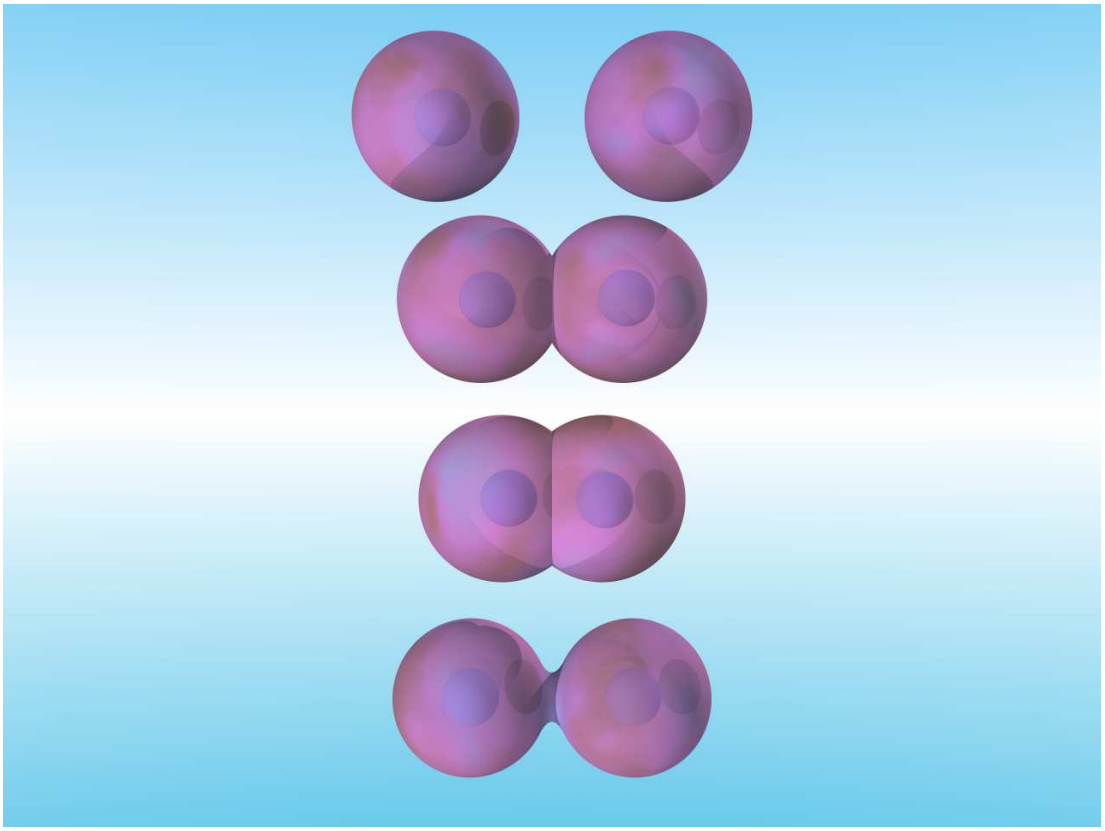

Figure 1.4: JKR force: (a) Two isolated cells have no interactions. (b) When they touch each other, they form spontaneously adhesive bonds, which results in an attractive force. (c) If cells are too close, the response is a repulsive force. (d) Once in contact, cells need to disrupt the bonds to detach, even if the distance among the two cell centers is greater than the sum of their radii.

- Blood vessels are modeled like connected cells. The interaction among these cells contains an additional elastic force: $F_{ij}^{elastic} = k(d_{ij} - d_{ij}^0)$ where k is the elastic coefficient of the force, d_{ij} the distance between the two elements and d_{ij}^0 the relaxed distance.
- The Young modulus of the vessel network is given by $E = \frac{k}{2\pi r}$ where k is the elastic coefficient and r the radius of the sinusoid.
- During the mitosis, a sub-element can be in contact with 2 sub-elements of the same cell. In this case, the interaction force is modulated with respect to the sub-element positions.

Active cell movement

For the active movement $\underline{F}_i^{\text{active}}$, we tested two different options. The uniformly distributed random movement for spherical objects :

$$\underline{F}_i^{\text{active}} = \sqrt{2\gamma^2 D}\underline{\eta}_i(t) \tag{1.4}$$

And in case of a pressure gradient, the active movement is also for spherical objects:

$$\underline{F}_i^{\text{active}} = (1 - \Theta[\underline{\nabla} p_i \underline{\eta}_i])\sqrt{2\gamma^2 D}\underline{\eta}_i(t) \tag{1.5}$$

$\underline{p}_i$ is the pressure of the cell i. $\underline{\eta}_i(t)$ active random movement of cell i: typically a vector of a white noise in 3D. $\Theta(x) = 1$ if $x \geq 0$ and becomes 0 otherwise (Heaviside function).

This second active force model takes into account the propensity for cells to move toward areas where the pressure is lower.

Cell surface of adhesion

Cell surface can be fully adhesive or only partially. In the latter case, the cell polarity is defined by a vector and an angle. The cell adhesive surface is defined by the intersection of the cell surface and the circular cones given by the vector and the angle. A cell adheres to another cell only if their two respective adhesive surfaces are in contact (see illustration 1.5). For dumb-bell cells, each sub-element has a polarity vector and a polarity angle. A cell adheres to a dividing cell if the adhesive surface of the cell is in contact with the adhesive surface of the closest sub-element of the dividing cell.

Angular momentum

The equation of the angular momentum $\underline{\Omega}_i$ of cell i is given by [21]:

$$\underline{\underline{\gamma}}_r^{cs}\underline{\Omega}_i = -\underline{\underline{\gamma}}_r^{cc}\sum_j \underline{r}_i^{ij} \times (\underline{v}_j^{ij} - \underline{v}_i^{ij}) + \frac{a_i}{2}\hat{\underline{a}}_i \times (\underline{F}_i^{(1)} - \underline{F}_i^{(2)}) + \hat{\underline{\tau}}_i^{\xi} \tag{1.6}$$

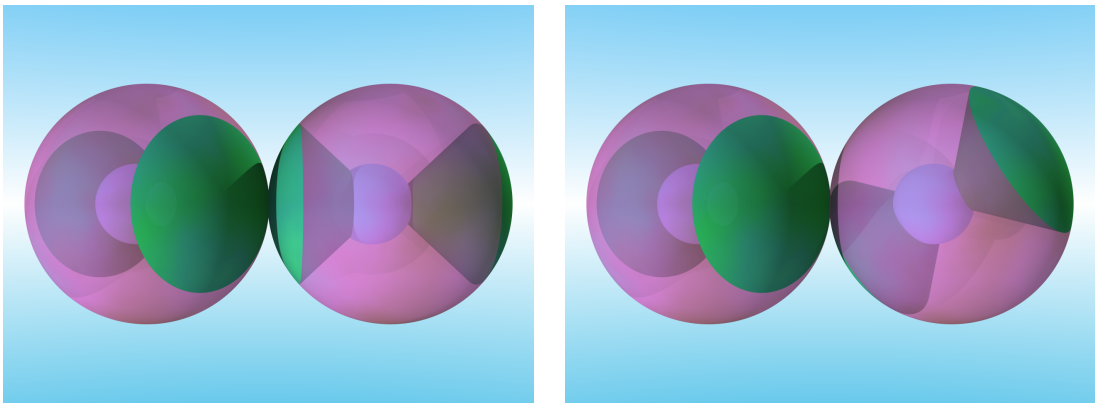

(a) 2 polar cells adhering to each other on their adhesive poles in contact.

(b) 2 polar cells not adhering, cells are in contact but not their adhesive poles.

Figure 1.5: Illustration of anisotropic cells. The green on the surface cell is the adhesive area of the cells. It is defined by 2 cones at each pole. A cell can adhere to another one only if both adhesive surfaces are in contact.

- $\underline{\underline{\gamma}}_r^{cs}\underline{\Omega}_i$ denotes the friction of cell i with the substrate due to its rotation.
- $-\underline{\underline{\gamma}}_r^{cc}\sum_j \underline{r}_i^{ij} \times (\underline{v}_j^{ij} - \underline{v}_i^{ij})$ denotes the cell-cell friction due to the rotation.
- $\frac{a_i}{2}\underline{\hat{a}}_i \times (\underline{F}_i^{(1)} - \underline{F}_i^{(2)})$ external torque on the cell i where $\underline{F}_i^{(1)}$ and $\underline{F}_i^{(2)}$ are the forces that act on the dumb-bell system (on the center of each spherical sub-element), a_i the length of the dumb-bell axis and $\underline{\hat{a}}_i$ the unit vector of this axis.
- $\underline{\hat{\tau}}_i^{\xi}$ is a random fluctuating torque.

We simplified with those assumptions:

- We started with the deterministic case and drop the random fluctuating torque $\underline{\hat{\tau}}_i^{\xi}$, the active movement $\underline{F}_i^{\text{active}}$ induces enough randomness in the system to relax it and to remove artificial situations.
- When cells are not polar, we don't consider cell rotation movement. When they are polar with use the metropolis algorithm of [22].

The equation becomes:

$$\underline{\underline{\gamma}}_r^{cs}\underline{\Omega}_i = \frac{a_i}{2}\underline{\hat{a}}_i \times (\underline{F}_i^{(1)} - \underline{F}_i^{(2)})$$

Molecular transport and diffusion

For some model applications, we have to couple biomechanics with local molecular concentration.

Linear and exponential approximation: *(for sinusoid morphogen attraction, see section 3.1.4)* Chemoattraction – the cell movement toward high chemoattractant concentration – is represented by an additional active force in the Langevin Equation: $F_i^{chemoattraction} = \chi \nabla c(x,t)$ where the function $c(x,t)$ is the molecule concentration at time t and at location x. We approximate the chemoattractant diffusion and consumption by a linear function (this approximation has been done for oxygen in [58]) or by an exponential function (exact solution in 1 dimension). The concentration is maximum at source location and 0 when distance is higher than the morphogen range.

Cell/Cell transport*(for Wnt and GF, see section 3.2)* To consider cell/cell molecule transport, we used an osmotic model of diffusion, which mimics the molecular exchanges from cell to cell via the surface contact of cell membranes with respect to the cell volume concentration. We assume homogenous concentration in cells, fixed cell volume, contact surfaces and distances at time t. The concentration is given by :

$$\frac{dc_i(t)}{dt} = \frac{D}{V_i} \sum_{j \in N(i)} \frac{s_{ij}(c_j(t) - c_i(t))}{d_{ij}} \tag{1.7}$$

where $N(i)$ is the set of indexed neighbors of cell i, s_{ij} the contact surface between cell i and cell j, V_i the volume of cell i, D the coefficient of diffusion for the considered molecule, d_{ij} the distance among cell i and cell j.

In case of fixed cells and full space discretization, equation 1.7 is the finite volume discretization used to solve the classic equation of diffusion:

$$\frac{\partial c(x,t)}{\partial t} = D\Delta c(x,t) \tag{1.8}$$

Cells follow the Langevin equation of motion and grow, so volumes, positions and contact surfaces evolve in time.

1.1.3 Measures available

As explained above, agent-based models provide a practical framework to include and extract data. The model gives access to all individual values of cells at any point in time, which is not possible in experiments. It is also possible to average individual values over several agents to obtain other observables. To understand the figure results, we listed below the available measures in the model.

Cell number

The cell number is accessible at all time points. It is also possible to specify the cell type or properties: tumorous, active, quiescent, apoptotic, etc.

Pressure

Two models of pressure computation have been used. Pressure P equals either the sum of forces exerted by cells in contact on the cell (equation 1.9) or the sum of positive forces exerted by cell in contact on the cell (equation 1.10), divided by contact surface between cells.

$$P = \Sigma_j \frac{F_{ij}^{JKR}}{A_{ij}} \tag{1.9}$$

$$P = \Sigma_j \frac{max(0, F_{ij}^{JKR})}{A_{ij}} \tag{1.10}$$

Contact area

The contact area among element model is computed thanks to space discretization. The domain space is discretized in a cubic and regular grid. Each cube that intersects with a cell is labeled by the cell index. Then, each cube face that separates two distinct elements (different cell index) can be counted. Thus, the model can measure the surface contact between healthy cells/ tumor cells, healthy cells / endothelial cell, tumor cells / endothelial cells, etc. To avoid units issues, the contact areas are divided by the total element surface in contact and presented as a dimensionless contact area fraction.

Densities

Biological information is commonly given as density. The model can relate the spatial element to a density by counting the number of elements on a discretized space. In the results sections, endothelial cells density is shown. The model can provide data in 3D or 2D (with projection on a plane) and delivers density of apoptotic cells, quiescent cells, tumor cells, proliferative cells, etc.

Blood vessel data

The nodes that constitute the endothelial cells (cells that form the blood vessels) are modeled as an elastic graph. From the position of each node and its connected nodes, we can establish the mean distance among nodes and also the mean angle (most of the time, the nodes are connected only twice). The mean node distance and mean angles are two measures for the distortion of the graph.

Radius of gyration

For cell populations, the radius of gyration R_g is a value that gives information on the object size and shape. This value is computed by giving a weight to each cell with respect

to the distance to the cell population center of mass. It is given by:

$$R_g = \sqrt{\frac{1}{N}\sum_i ((x_i - x_{cm})^2 + (y_i - y_{cm})^2 + (z_i - z_{cm})^2)} \tag{1.11}$$

where $x_{cm} = \frac{1}{N}\sum_i x_i$, $y_{cm} = \frac{1}{N}\sum_i y_i$ and $z_{cm} = \frac{1}{N}\sum_i z_i$ are the coordinates of center of mass.

Principal component analysis

Let M be the cell population covariance matrix.

$$M = \begin{bmatrix} \sum_i (x_i - x_{cm})^2 & \sum_i (y_i - y_{cm})(x_i - x_{cm}) & \sum_i (z_i - z_{cm})(x_i - x_{cm}) \\ \sum_i (x_i - x_{cm})(y_i - y_{cm}) & \sum_i (y_i - y_{cm})^2 & \sum_i (z_i - z_{cm})(y_i - y_{cm}) \\ \sum_i (x_i - x_{cm})(z_i - z_{cm}) & \sum_i (y_i - y_{cm})(z_i - z_{cm}) & \sum_i (z_i - z_{cm})^2 \end{bmatrix} \tag{1.12}$$

where x_{cm}, y_{cm}, z_{cm} are the coordinates of the cell population's center of mass and x_i, y_i, z_i the coordinates of cell i.

In 3D, the principal component analysis consists in finding eigenvalues of the covariance matrix M. Each value is the size of the axis in a coordinate system, chosen such that the longest axis of the object of cell population is the first eigenvalue; the other ones are orthogonal to this axis. In case of compact cell populations, the principal component analysis is a key value to analyze the results. It gives the symmetry of the cell population. A spherical population pattern has equal eigenvalues whereas elongated population patterns have at least one greater eigenvalue.

Evolving pattern

During the computation, because each cell position is known, it is possible to observe cell population's shape. Regularly, the model outputs all positions in a file. The cell population can then be visualized thanks to the visualization tool implemented and described in the next section.

Conclusion:
The developed model takes place in the realm of systems biology research, a relatively recent domain of science. It approaches problems like experimental science does, but in contrast to which the experiments are conducted in computer software. In many contexts and in biology especially, agent-based models are good candidates for this type of modeling. They provide a direct approach in which all individual information is immediately available. Finally, by approximating the cell as dumb-bell and including biomechanics in the model, the elements follow this equation of motion:

$$(6\pi\eta_0 r_i)\left(\frac{A_i^{cs}}{A_i}\underline{v}_i + \frac{a_i}{2}\hat{\underline{a}}_i \times (\underline{F}_i^{(1)} - \underline{F}_i^{(2)})\right) + \sum_j \underline{\underline{\Gamma}}_{cc}\frac{A_{ij}}{A_i}(\underline{v}_i^{ij} - \underline{v}_j^{ij}) = \sum_j \underline{F}_{jkr}^{ij} + \underline{F}_i^{\text{active}} \tag{1.13}$$

Chapter 2

Implementation of the simulator

In brief:
In this chapter, we describe algorithms and necessary components to simulate the agent-based model presented in the previous chapter. Due to the complexity of the problem, many challenges had to be faced and the implementation occupied a large part of the working time. Technical descriptions are developed here in order to be reproducible: program language, libraries, algorithms, numerical schemes, parallelization and solvers. We show benchmarks that compare program efficiency of the sequential version to the parallel version.

2.1 Introduction

The model is based on the framework of [22], but the complexity turned out to be far beyond the simulation tool to model monolayers and multi-cellular spheroids, and more complex than the model tool used for liver regeneration [43]. Moreover, in a number of simulations the tumor cells were strongly compressed against the blood vessels, which yields very large forces. In order to guarantee numerical stability, the time step had to be significantly reduced, which led to very long simulation times. Significant effort was spent for making the simulator faster, more flexible and more robust. This led to a better modularity of the code and about 5-times shorter simulation times than the first version of the code. A large number of independent tests had to be performed to guarantee a high reliability. The whole code is 50,000 lines large. The development time represents about two third of the total worked time. We present in this chapter the main algorithms and libraries used to simulate the model.

2.2 Description of the components of the code

In brief:
The choice of the programming language was guided by our needs, which are:

- Modularity: the model should be open to extensions without a full re-organization of the code.
- Collaborative: the code should be readable and understandable rapidly by collaborators.
- Fast: the simulations deal with a large number of elements. The program must be fast enough (optimized compilers, optimized algorithms).
- Robustness: A debugging method should be applicable on the code to ensure a minimum of implementation error.

2.2.1 An adapted programming language for agent-based model: C++

C++ is a programming language born at the end of the 70's. Bjarne Stroustrup, its creator, made it up first to enhance with classes the very fast and robust programming language C[74]. The purpose was to make C, an object-oriented language. Later, many other features have been added to C++, which make this programming language still alive and evolving (last release was delivered in september 2011). During the last decades, C++ became a very popular language. Thanks to the Internet development, many communities used and ask to the C++ committee to improve the language. In particular, many libraries of functions where developed for free and tested by an international community (*boost* library for instance). This success is due to the great performance of C++ (much faster than java, a language that offers approximately the same possibilities) and its modularity. Indeed, oriented-object languages are conceptually thought to be modular. It is possible to program independent building blocks and integrate them in the code [26]. This modularity is appreciated in collaborative work and open problems that are constantly evolving – like it is in scientific research. Moreover, application to individual based models is straightforward to translate in object-oriented programming language. The program was developed in order to serve different mathematical models based on the same model framework. For this purpose, the generic programming possibility is useful if one wants to use classes with different objects. We make here a general remark on imperative programming language: the object structure is very good to split and cut and apply reductionism paradigm to the implementation. The implementation of the interactions between agents is not solved anyway. Algorithms have to be well defined and ordered to be properly implemented. Relations among the object are the difficult part (in particular, discretizing and sorting the interactions). Finally, as C++ is very popular, it comes with many graphical

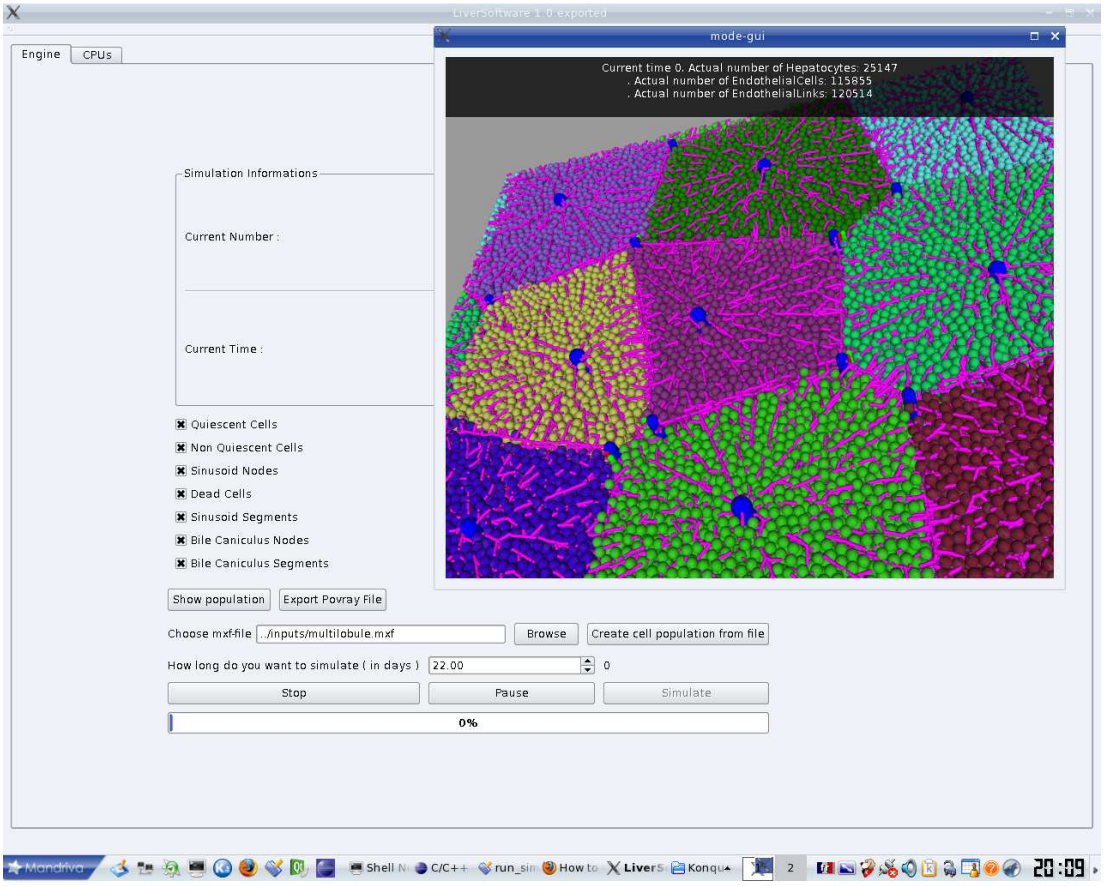

Figure 2.1: Screenshot of the Graphical user interface with OpenGl real time visualization

user interface (GUI) libraries. We chose Qt library for its large number of functions and its complete documentation (figure 2.1). Based on our constraints and C++ capabilities, C++ programming language was the best candidate to code a simulator.

2.2.2 Visualization with OpenGL library and POVRAY

Visualization is one of the most useful measures in simulations for programmers to debug. On the contrary, the modeler must not rely on visualization. Figures and curves only may prove that simulations are correct but their ability to stimulate intuition is not as efficient than visualization. Moreover, images can be directly compared to experimental images and this issue is crucial in biology. This is why it has been necessary to produce images and movies from our simulations. The software includes a 3D real time visualization of the simulations that has been coded with OpenGL library. The simulator outputs are processed and can produce 3D visualization as well. For this post-processing, the ray tracer POVRAY was chosen. The image quality plus the interface close to C language easy to understand for programmers imposed us this choice. The software developed for the model integrates a module that converts model data to POVRAY data format. As an

Core number	Code description	Gain	% of parallelization
1	(1): Model with no cell-cell friction		
12	(1)	2.5	67%
12	(2): (1) + parallelization of contact detection	2.92	73%
1	(2) in Liver		
12	(2)	4.92	88%
1	(3): (2) + cell/cell friction		
12	(3)	2.31	63%
12	(4): (3) + matrix assembly parallel	2.29	62%
12	(5): (4) + sparse matrix multiplication in parallel	2.40	65%
12	(5) + conjugate gradient parallel	3.18	76%

Table 2.1: Benchmarks of parallelized portion of the code

example, all images from the model in this document have been obtained with POVRAY.

2.2.3 OpenMP

New machines offer multiple cores CPU and/or multiple CPUs. We took advantage of it with library OpenMP® included in last GNU C++ compilers. The use of this library is simple. The purpose is to compute at the same time in different cores with a shared memory. The temptation to parallelize the computation is high because the shared memory does not copy data to pass it to other computation units. Shared memory parallelization needs carefulness. The main advantage of the shared memory is also its immediate drawback while it is possible to write and read at the same memory location with different threads leading to memory errors and program failure. OpenMP® library provide an easy method to distribute the computation over the cores during the loops. Most of the computations are made with loops over the elements of the system. In a 10 cores machine, this should allow a 10 times faster computation. Unfortunately, this optimal case is rarely reached because of element dependency. Furthermore, some parts cannot be fully parallelized. For instance, updating a list by swapping, adding or removing elements is not an operation that can be fully separated in different threads without copying data. The best here is to make a list by threads with elements that are to be modified and then scan the resulting lists to apply the modifications. The additional cost could make unfruitful the parallelization.

The computation speed is dependent on the number of objects and their types. In table 2.2.3, we present some benchmarks that show the efficiency of the parallelization. % of parallelization is $\frac{100}{G-1}$, G is the gain in computation time, and represents the fraction of the code that is computed in parallel.

2.2.4 Debugging protocol

The complexity of the program needed to apply a strict debugging protocol. The code can be compiled in *debug mode* or in *release mode*. The two versions coexist. Each parallel algorithm is sequentially coded and during *debug mode* execution, the results of each parallel algorithm is compared to its sequential version. For optimized algorithm we proceed the same way. The greedy version, usually easier to implement and containing less bugs, is coded and compared to the optimized one to ensure that the results are correct. Furthermore, the memory checker Valgrind was used to check any leak of memory after each important modification of the code. When it was not possible to find the origin of the bug,we used a full debugger called GDB. Finally, we tested the simulator in simple cases to check the behavior of the model.

2.2.5 Diffusion of the code

Today, the code is applied to different model variants. Coding variants allow programmers to make evolve the code by adding new functions and to find unsuspected mistakes. In particular, new cases that were not tested are explored. A program with no bugs is a program with no users. Thanks to collaborations, (3 partners are using the present described source) the code evolved and became more robust. The different applications are briefly presented in the Appendix 4.2.

2.2.6 Automatization and Monitoring

The model requires testing many parameters and assumptions. This sensitivity analysis produces a lot of results. The large number of simulations to perform prevents to rely on human control of the whole process that introduces to many mistakes. To minimize the mistake introduction, we automatized the workflow. The process chain is automatized such that the modelers need only to choose the parameters and options of the simulation. This is performed with two *shell scripts*.

Shell script process: Compile/Run/Post-Process

1. Edit a configuration file with macros.
2. Compile the code with proper options and files (only compile the files associated to the chosen model to minimize the compilation time).
3. If the compilation finished: copy sources, configuration and initial file to folder.
4. Run the program with parameters (duration, iteration number, simulation name, initial file path).
5. While the program is running and producing outputs, they are processed and stored (descriptive latex file, curves with Gnuplot, images with Povray and movies).

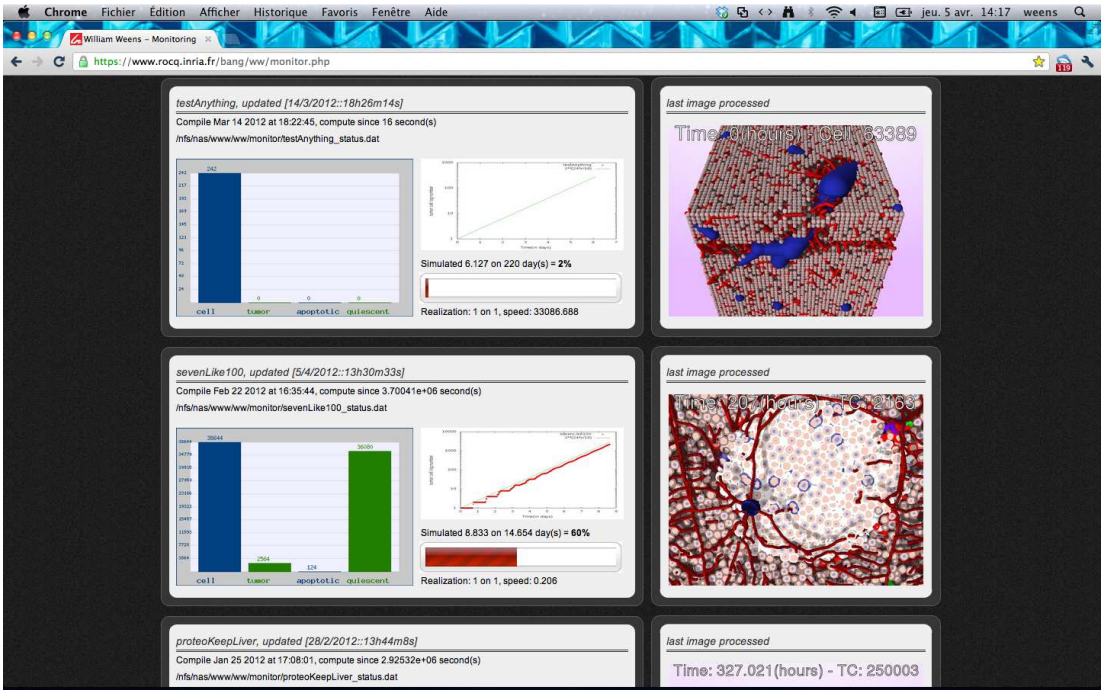

Figure 2.2: Screenshot of the web page where results are automatically sends. A brief summary of information is presented: cell number, tumor cell number, last image processed, running time, etc.

6. The last image and curve processed are sent to the server open to the web with some additional information (cell number, tumor cell number, percentage of the duration accomplished).

The first script allows to choose in a text file the *defined macro* (corresponding model assumptions listed in Appendix 5.3) and parameters that will be used in the simulation. This method saves running time because the model options only are compiled. Other options do not exist in the final executable and so the program does not need to evaluate the different possibilities during the execution. In addition, each user has its own configuration file and can compile the code with its usual options without risking compilation conflicts with other users functions.

The second script is a loop that scans all simulation outputs and processes the result. It compiles the program with backup sources and translates the output files into curves (with GnuPlot), images with POVRAY and movies (FFMPEG concatenate the images). Each image is sent to a web server. A web page has been designed to show progression of the simulation in real time (figure 2.2).

Conclusion:
C++ is an appropriate programming language choice because of :

- Many libraries (especially parallel programming, graphic library and user interface)
- Quite low level language, speed of execution
- Modularity (for different problems and collective work)s
- Popularity (students, collaborators often know this language and it is easy to find documentation)
- For agent-based modeling: object-oriented, inheritance, generic programming
- Parallelization with OpenMP included library in GNU C++ compiler.
- A large choice of debugging tools exist for C++ code.

2.3 Numerical methods and algorithms

In brief:
The aims of the simulator are to compute equation (4.1) with an initial input and to output and analyze the results. In this section, we present selected algorithms and numerical methods we used to compute the Langevin equation: numeral issues, numerical schemes, main algorithm, parallel sparse matrix solver and parallel contact detection. Many functions that simulate or analyze the model are too trivial and can be straightforward programmed even though the time to include them in a code can be long.

The computation of the system of Langevin equations (4.1) is made in two steps. In computers, continuum does not exist so the continuum equations need at first to be discretized in time and space. Then each of equations component has to be computed to actually solve the equation.

Explicit Langevin discretization

Generally, implicit numerical schemes are more stable and allow taking bigger time step than explicit schemes. In our case, the implicit discretization is not possible because of the Johnson-Kendall-Roberts (JKR) force. Indeed, JKR force is not given by the derivative of a potential but directly as a force. This does not help to define the variational problem if one wants to solve the numerical schemes with finite elements for instance. Moreover, it is implicitly defined (equations (1.2) and (1.3)). In spite of these two reasons, it is possible to define numerically a JKR potential. Finally, the real obstacle that prevents the use of

an implicit scheme is that it is impossible to know the elements in contact for future time. Without this information, it is not possible to derive forces acting in the system.

We rewrite equation (4.1) for element i, with velocity v_i, $v_{ij} = v_j - v_i$, α the medium friction, β_{ij} is the cell-cell friction, e vector from cell i-th to cell j-th center, f_i sum of the forces but frictions on cell i (NB. β_{ij} is surface dependent $\beta_{ij} = \beta \frac{A_{ij}}{A_i}$ and $\beta_{ij} \neq \beta_{ji}$). The explicit Langevin discretization for each element is:

$$\alpha v_i^n = \sum_j (\beta_{ij}^n (v_{ij}^n - e_{ij}^n (v_{ij}^n \cdot e_{ij}^n))) + f_i^n \tag{2.1}$$

where upper-script n denotes that the term is computed at time point n where the system state is known, $v_i^n = \frac{x^{n+1} - x^n}{dt}$, x^n is the position of element i at time n and dt the time step. Thus, v_i^n permits to compute x_i^{n+1}, the new position of the element.

Time step issue

We are not able to prove the stability of these explicit schemes due to non-linearties and complications introduced by the cell growth, division, death and hysteresis. However, we define the time step with a hard condition that prevents numerical errors. Indeed, for each iteration we look for the time step value that ensures that:

1. collision between elements well captured.

2. adhesion ruptures cannot be artificially induced.

For case 1, the time step dt is accepted if $dt \leq \frac{1}{3} min_i(\frac{min_j(d_{ij})}{v_i})$. This condition guarantees that no element will be closer than one third of its closest element. For instance, at time t_n, if two elements attract each other, at time $t_{n+1} = t_n + dt$, the force among the elements is evaluated again. If elements are too close from each other (collision), the force becomes repulsive; else elements are still attracted but again cannot move to be closer than one third of their distance. Thus, the algorithm will not miss their collision. For case 2, the principle is the same but applied on the adhesion rupture distance.

The simulations of stiff blood vessels turned out to be very long despite parallelization of the code, particularly if the vessel Young modulus is chosen to be 1000 Pascal or larger, which corresponds to realistic values. Indeed, the vessel nodes are very close to each other and their velocity depends on the elastic force among them. Large forces necessarily decrease the time step and in the case of vessel stiffness this relation is linear.

Adapted time steps can induce oscillations between elements in contact. The time step is chosen to be maximal (under the condition mentioned above) and elements could move around their equilibrium position (when it exists). This effect is smoothed out when the number of element is large. However, to avoid this artificial effect and large time step variations, dt is taken close to the mean value of the time steps. If $(dt \leq < dt >) dt := dt$ else $dt := \frac{\leq dt > + dt}{2}$) where $< dt >= \frac{1}{N} \Sigma_n^N dt_n$ the mean dt value over the iterations.

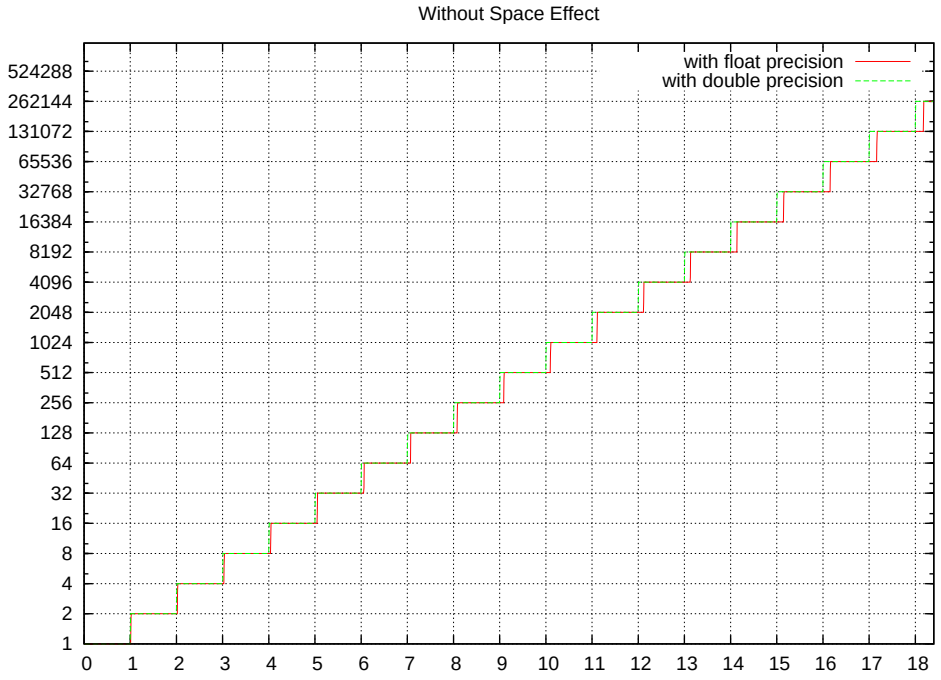

Figure 2.3: Number of cells respect to time in a non spatial model. The two curves are produced by the same code. The red curve used a simple precision for real numbers (float), the green curves used a double precision (double). The cell population doubles every unit of time. The tow curves are progressively desynchronized is due to the **truncation error**.

Truncation error

Discretization of space is not needed to solve the Langevin equation and the model agents can freely move in space. Notwithstanding computers cannot compute with real numbers and a "discretization" is hidden somewhere. Indeed, real numbers are truncated at a certain order of precision (in computers, it correspond to the number of bits used). This truncation can create serious artifact. For instance, for a simple non-spatial model of cell division, if the precision is insufficient, the cell division is delayed (see figure 2.3) and results do not correspond to the model.

2.3.1 Solving cell-cell friction

In 2.1, each v_i^n depends on other velocities. The computation of the element velocity needs to solve a system. For two elements, with omitting the time n and assuming same size object for simplicity $\beta = \beta_{ij} = \beta_{ji}$, the system to solve is:

$$\begin{cases} \alpha v_i = \beta(v_{ij} - e_{ij}(v_{ij} \cdot e_{ij})) + f_i \\ \alpha v_j = \beta(v_{ji} - e_{ji}(v_{ji} \cdot e_{ji})) + f_j \end{cases} \tag{2.2}$$

Let u be the speed of cell i and v speed of cell j, the full developed example with 2 cells becomes:

$$\begin{cases} (\alpha+\beta(1-e_x^2))u_x + \beta(e_x^2-1)v_x + \beta e_x e_y v_y - \beta e_x e_y u_y + \beta e_x e_z v_z - \beta e_x e_z u_z = f_x^i \\ (\alpha+\beta(1-e_y^2))u_y + \beta(e_y^2-1)v_y + \beta e_x e_y v_x - \beta e_x e_y u_x + \beta e_y e_z v_z - \beta e_y e_z u_z = f_y^i \\ (\alpha+\beta(1-e_z^2))u_z + \beta(e_z^2-1)v_z + \beta e_z e_y v_y - \beta e_z e_y u_y + \beta e_x e_z v_x - \beta e_x e_z u_x = f_z^i \\ (\alpha+\beta(1-e_x^2))v_x + \beta(e_x^2-1)u_x + \beta e_x e_y u_y - \beta e_x e_y v_y + \beta e_x e_z u_z - \beta e_x e_z v_z = f_x^j \\ (\alpha+\beta(1-e_y^2))v_y + \beta(e_y^2-1)u_y + \beta e_x e_y u_x - \beta e_x e_y v_x + \beta e_y e_z u_z - \beta e_y e_z v_z = f_y^j \\ (\alpha+\beta(1-e_z^2))v_z + \beta(e_z^2-1)u_z + \beta e_z e_y u_y - \beta e_z e_y v_y + \beta e_x e_z u_x - \beta e_x e_z v_x = f_z^j \end{cases} \tag{2.3}$$

The matrix form of equation 2.3 with $\gamma_x = \beta(1-e_x^2)$, $\gamma_y = \beta(1-e_y^2)$, $\gamma_z = \beta(1-e_z^2)$, $\beta_{x,y} = \beta e_x e_y$, $\beta_{x,z} = \beta e_x e_z$ and $\beta_{y,z} = \beta e_y e_z$ is:

$$\begin{pmatrix} (\alpha+\gamma_x) & -\beta_{x,y} & -\beta_{x,z} & -\gamma_x & \beta_{x,y} & \beta_{x,z} \\ -\beta_{x,y} & (\alpha+\gamma_y) & -\beta_{y,z} & \beta_{x,y} & -\gamma_y & \beta_{y,z} \\ -\beta_{x,z} & -\beta_{y,z} & (\alpha+\gamma_z) & \beta_{x,z} & \beta_{y,z} & -\gamma_z \\ -\gamma_x & \beta_{x,y} & \beta_{x,z} & (\alpha+\gamma_x) & -\beta_{x,y} & -\beta_{x,z} \\ \beta_{x,y} & -\gamma_y & \beta_{y,z} & -\beta_{x,y} & (\alpha+\gamma_y) & -\beta_{y,z} \\ \beta_{x,z} & \beta_{y,z} & -\gamma_z & -\beta_{x,z} & -\beta_{y,z} & (\alpha+\gamma_z) \end{pmatrix} \begin{pmatrix} u_x \\ u_y \\ u_z \\ v_x \\ v_y \\ v_z \end{pmatrix} = \begin{pmatrix} f_x^i \\ f_y^i \\ f_z^i \\ f_x^j \\ f_y^j \\ f_z^j \end{pmatrix}$$

Let matrix A_{ij} be :

$$A_{ij} = \begin{pmatrix} -\gamma_x & \beta_{x,y} & \beta_{x,z} \\ \beta_{x,y} & -\gamma_y & \beta_{y,z} \\ \beta_{x,z} & \beta_{y,z} & -\gamma_z \end{pmatrix}$$

For a system of 4 elements, where element 1 interacts with 2 and 4, element 2 interact with 1 only, element 3 has no interaction and element 4 interacts with 1 only.

$$\begin{pmatrix} \alpha I_3 - A_{1,2} - A_{1,4} & 1_{1,2} & 0 & A_{1,4} \\ A_{1,2} & \alpha I_3 - A_{1,2} & 0 & 0 \\ 0 & 0 & \alpha I_3 & 0 \\ A_{1,4} & 0 & 0 & \alpha I_3 - A_{1,4} \end{pmatrix} \begin{pmatrix} u_1 \\ u_2 \\ u_3 \\ u_4 \end{pmatrix} = \begin{pmatrix} f_1 \\ f_2 \\ f_3 \\ f_4 \end{pmatrix}$$

This example shows that as the number of element increases, the sparsity of the matrix increases too. In 3 dimensions, the average number of neighbors for an element is 12. In our common application the non zero values represent only 0.001% of the total matrix. We used this sparsity to store the matrix. Indeed, the matrix size for N elements is $3NN$ that prevents the full storage of the matrix in computer memory. We build up a special class to store symmetric sparse matrix and to solve in parallel the linear system $Ax = b$ (A is the sparse matrix, b the force known force vector and x the unknown vector of velocities. We used the symmetric Compressed Storage Column (CSC) matrix format [32] (see example with equivalent format Compressed Storage Row (CSR) 2.4). The matrix is assembled on the fly during the contact detection. We solve the system with the conjugate gradient method, an iterative method where the matrix vector multiplication and the sums over elements are parallelized. To debug, we use the Cholesky direct method and we compare the results [70].

2.3.2 Main algorithm

The main algorithm is called to simulate the model evolution. For each time step, it computes the forces in the system and moves the elements with respect to these forces. The time step is computed and adapted to be as large as possible. The time step value is added to the total simulated time. The algorithm stops when the total time t is greater than the prescribed duration T.
While $t \leq T$:

1. ***initialize all sub-element***: Reset the displacements, pressures, contact elements. *→ OpenMp optimized*

2. ***compute hysteresis***: Compute the forces among pairs of elements recorded in the previous iteration. *→ OpenMp optimized*

3. ***apply on each pair(compute cell/cell forces, compute cell/node forces)***: Space is discretized in a regular grid. Look for possible pairs of elements in contact (detail in 2.3.3). If a contact is found, the force among elements of the pair is computed. The pair is recorded for hysteresis effect. *→ OpenMp optimized*

4. ***update cell polarity***: Polarity is updated via the metropolis algorithm (detail in [22]). *→ OpenMp optimized*

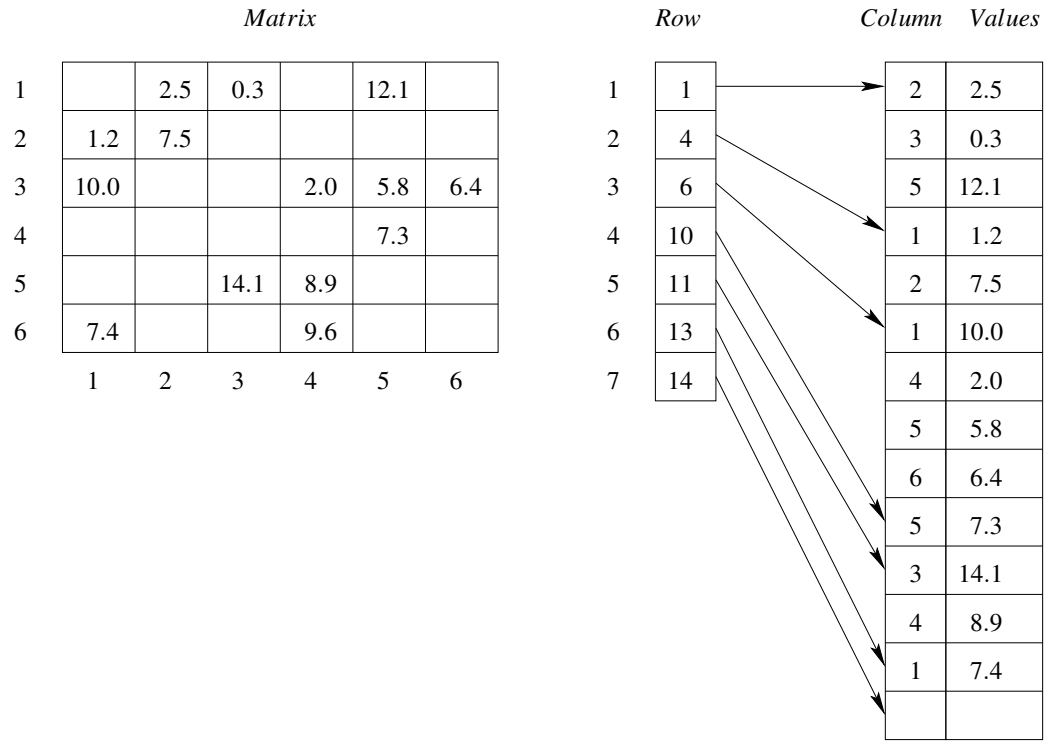

Figure 2.4: CSR format to store a sparse matrix. Let N be the dimension the matrix and m the number of non-zero values of the matrix. The *Row* vector has then a size $N+1$ and the *Column* vectors and *Values* a size $m+1$. For i from 1 to $N+1$, $Row[i]$ stores the position in the *Values* vector at which starts the storage of the non-zero values of the row i of the matrix. $Row[n+1]$ point at the last position of the *Values* vector. Thus, for j of $Row[i]$ to $Row[i+1]-1$, $Values[j]$ corresponds to a non-zero value on the row i and $Column[j]$ indicates the position of the corresponding column. Figure from Maya de Buhan.

5. ***compute spring force***: Compute the elastic force between nodes of the graph that represents the vasculature. → *OpenMp optimized*

6. ***compute pressure gradient***: Compute the pressure on a grid of cell densities to add a bias in the random movement. → *OpenMp half-optimized*

7. ***solve friction***: The friction matrix is assembled with each cell-cell contact detected above in step 3. The inversion of the matrix is done with a parallel conjugate gradient. Details in Section 2.3.1. → *OpenMp optimized*

8. ***compute torque rotation***: Compute the dumb-bell rotation. It sums up the asymmetric forces on the dividing cells and computes the rotation. → *OpenMp optimized*

9. ***compute random***: Compute the cell random force and the adapted time step. The time step is reduced in order not to miss collisions. It must be done after every component of the movement has been actually computed.

10. ***compute diffusion***: Set the source elements (it depends on their location, they could have moved or changed), list every cell surface area.

11. ***Compute the adapted time step***: Choose a mean time step to decrease large time step variations that could create oscillations. Minimum of moves with random adapted time step and diffusion adapted time step. adaptedTimestep(dt) = min(maxTimeStep, 1.2×meanTimeStep) → *OpenMp optimized*

12. ***Apply diffusion***(dt): with respect to the adapted time step dt, update the concentration values in the cells.

13. ***Compute intracellular concentrations***(dt): with respect to the adapted time step dt, compute the values of the intracellular concentrations (ODE system)

14. ***update cell status***(dt): with respect to the adapted dt. Kill, grow or divide cells. This function is difficult to parallelize because the list of elements is modified. Several threads could potentially write at the same memory location.

15. ***apply random move***(dt): with respect to the adapted, actually add $\alpha\underline{\eta}\sqrt{dt}$, the random movement, in each element. $\underline{\eta}$ is a gaussian distributed random vector, α the amplitude of the movement. → *OpenMp optimized*

16. ***Link growth***(dt): Increase the distance among nodes in the graph with respect to the adapted time step. → *OpenMp optimized*

17. ***Node death***: Destroy nodes that undergo too high pressure.

18. ***Move All***(dt): Actually apply the computed move and change the position of all elements. t → *OpenMp optimized*

19. ***Update link length***: Once the nodes have moved, the length of the edges of the graph should be updated. → *OpenMp optimized*

20. ***Stretch growth***: If the length of the links doubled, we add a node. → *OpenMp optimized*

21. ***Update positions in map box***: Update the list of elements in the grid used to detect contact. → *OpenMp optimized*

22. *t* **+=** ***adaptedTimestep***: Increment total simulated time *t*

2.3.3 Parallel contact detection algorithm

In brief:
Contact detection algorithm is an example of an algorithm that cannot be parallelized simply by splitting the loop over the elements in different threads. Because of its high computational cost, the algorithm benefits of parallelization with few elements. We implemented a generic class for contact detection in parallel.

The detection of the interactions depending on distance between objects (mainly contact detection) occupies a large part of the computation. The most basic algorithm can be straightforwardly implemented but has complexity in $O(n^2)$, n being the number of elements, and makes the computation too slow even for few elements (algorithm 2.1)

Algorithm 2.1 Basic algorithm for contact detection. Each element has index (integer), spatial coordinates x,y,z, radius r. Complexity is $O(n^2)$, the worst.

```
for element i = 1 → n − 1 do
    for element j = i + 1 → n do
        if (x_i − x_j)^2 + (y_i − y_j)^2 + (z_i − z_j)^2 ≤ (r_i + r_j)^2 then
            displacements i, j ← f(i, j)
        end if
    end for
end for
```

In the model, objects have approximately the same size. Adapted algorithms for this particular situation have been developed in order to find rapidly the interacting pairs [65, 66]. The principle is to discretize the domain in bounding boxes and to list the objects in it. For spheres, we consider that an element is in a box if its center is actually in the bounding box. The contact detection needs to check the distance among each pair of objects. Elements of a box can be in contact with elements within the same box and/or with elements in neighboring boxes. This routine has a complexity in $O(m^2)$ where m is the number of objects in the box and surrounding boxes. That is why it is very important to reduce as possible the number of objects in boxes. If elements are spherical, the best

box size is the sphere diameter. This algorithm reduces immediately the complexity to $O(n)O(m)$. It seems to be the minimal complexity because the algorithm has to pass by the list of all elements at least once algorithm (2.2).

Algorithm 2.2 Improved algorithm for contact detection with bounding boxes. Each element has index (integer), spatial coordinates x,y,z, radius r. Complexity is $O(n)O(m)$.

```
for element i = 1 → n do
    b ← box index of i
    for element j ∈ b, → m do      ▷ for each elements of box b and neighbors of box b
        if (x_i − x_j)^2 + (y_i − y_j)^2 + (z_i − z_j)^2 ≤ (r_i + r_j)^2 then
            displacements i, j ← f(i, j)
        end if
    end for
end for
```

It is possible to enhance this algorithm (algorithm 2.3). The loop is not made on each element but on each box. The boxes are listed dynamically and so the number of boxes is less or equal than the number of elements. The first advantage is that it allows skipping finding the box index of each element. The most important advantage is that it permits to look only on half of the neighboring boxes without missing any contact (see 2.5). In dimension 3, this algorithm saves 13 loops with respect to the classical contact algorithm.

Algorithm 2.3 Algorithm for contact detection with bounding boxes and enhancement. Each element has index (integer), spatial coordinates x,y,z, radius r. Complexity is $O(b)O(m^2)$. The enhancement consists in looking directly in the boxes. It permits to look only half of the neighbors and skip the step of finding box index of i.

```
for box b = 1 → nb do                                   ▷ loop over the boxes
    for element i ∈ b, → m do                           ▷ for each elements of box b
        for element j ∈ b and in half of neighbors do
            if (x_i − x_j)^2 + (y_i − y_j)^2 + (z_i − z_j)^2 ≤ (r_i + r_j)^2 then
                displacements i, j ← f(i, j)
            end if
        end for
    end for
end for
```

Finally, with this modified form, the parallel computation of algorithm 2.3 is possible and more accurate. OpenMP ® parallelization is more efficient on costly loops. Indeed, the distribution of the computation over the different cores and threads has a certain fix computational cost. In the contact detection algorithm, it is better to parallelize the upper loop on boxes. Nevertheless, the splitting of the box list must ensure that 2 elements would not be written at the same time by different threads. Here, the parallelization requires additional information of the model: a contact cannot occur between objects separated by

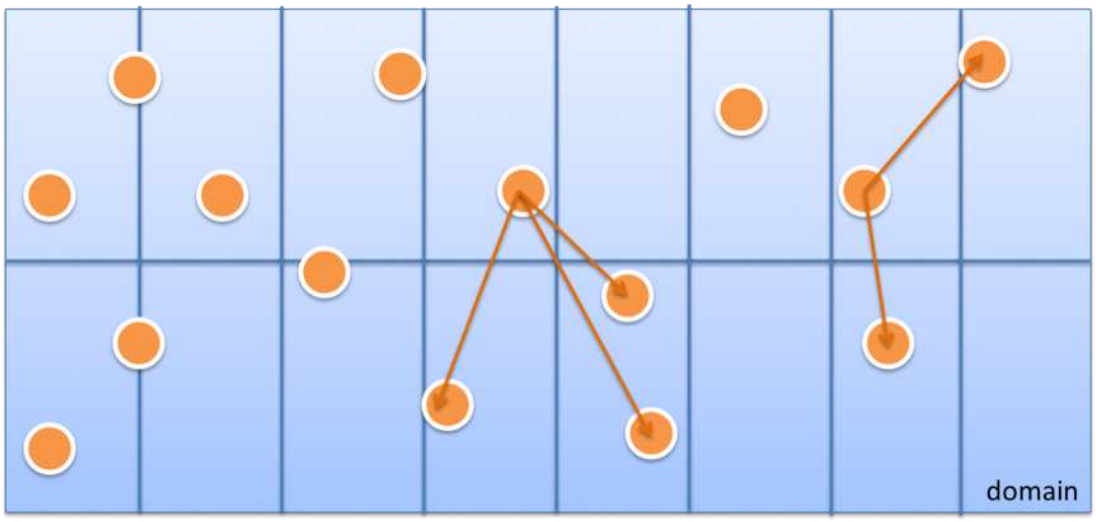

Figure 2.5: Sequential algorithm. For each element in each box, the distance between elements in box and neighboring boxes is check to detect contacts.

more than one box. Thus, if even box indexes are computed in parallel, a thread for an index, different threads cannot read/write on the same elements (see 2.6) and the same for odd box indexes (algorithm 2.4).

Algorithm 2.4 Algorithm is the same than the sequential 2.3 but the loop over boxes is parallelized.

for list of box with x index even, then list of box with x index odd **do** ▷ Parallel loop over boxes list.
  for box $b = 1 \in$ list $\rightarrow nb$ **do** ▷ loop over the boxes of the list
    for element $i \in b, \rightarrow m$ **do** ▷ for each elements of box b
      for element $j \in b$ and in half of neighbors **do**
        if $(x_i - x_j)^2 + (y_i - y_j)^2 + (z_i - z_j)^2 \leq (r_i + r_j)^2$ **then**
          displacements $i, j \leftarrow f(i, j)$
        end if
      end for
    end for
  end for
end for

For our model, we include additional features. Elements of the boxes are generic and code with *template* classes, this is particularly useful to use this class for new models. We create a dedicated and optimized data structure for the boxes for dynamic memory allocation of elements and fast memory access. For the liver applications, we introduce periodic domain. Boxes at the border are connected to the other border. It is especially tricky for the parallel algorithm because the number of columns could be inappropriate. For instance, if the number of threads is 5 and the number of column is 9, the last column

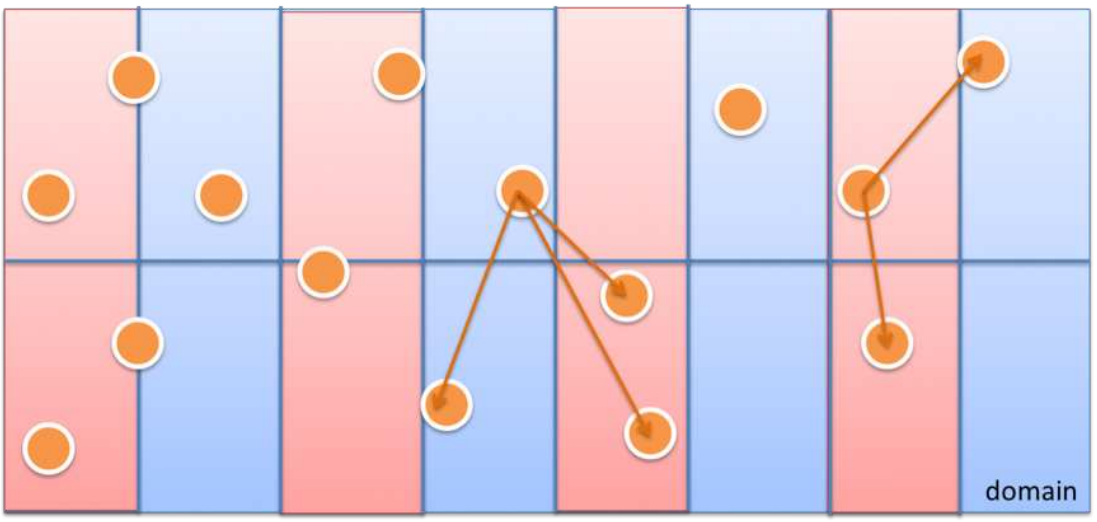

Figure 2.6: Parallel algorithm. Each blue column is computed in a different thread. No memory collision can occur between the different threads because they don't treat the same element. Once the contact detection of the elements of the blue box have been checked, the algorithm computes in parallel the red column.

will be computed by thread 5 and the first by thread 1 at the same time. Threads at the border could then cause memory collisions. To avoid this, the size of the boxes has to be set such that the number of columns is adapted to the number of threads. Finally, we implement a second type of elements. These elements are blind to their own kind but interact to the first type of element.

Conclusion:
Model simulations are very demanding. They imply a large number of elements and ask for numerical accuracy and rigorous conditions. A large part of the work is necessarily invested in implementation and optimization. Efficient algorithms have been created to work with recent techniques of parallelization and provide software able to solve rigorously the model. We manage to create the first liver model able to analyze multiple cancer phenotypes in 3D in a multi-lobule environment. Moreover, thanks to the generic implementation, the code can be applied to other models.

Chapter 3

Application to liver carcinogenesis

3.1 Introduction

In brief:
Despite the large efforts over the last decades, cancer is a leading cause of death. The complexity of the disease has now led to request of support to the mathematical community [28]. Colnot et al. [15] have developed an interesting liver *in vivo* cancer mouse model. The model could explain some aspects of the human liver cancer but also pointed a number of questions. We adapted the model introduced in the previous chapters to address these questions by studying the possible influence of different mechanisms on carcinogenesis by simulations with our *in silico* liver model. We detail in this section the biological information necessary for this application, namely: the liver cancer, the mouse model, its data and questions, and the model specificities that we had to include to mimic possible scenarios of carcinogenesis in liver.

3.1.1 Some key figures about cancer

The most general cancer definition could be: "an abnormal cell proliferation caused by genetic mutations". In most cases, the proliferation of cancer cells has a monoclonal source [36], which means that a single mutated cell initiates the cancer and the invasive clone is composed of only one genotype. This cell is degenerated and, by either its proliferation, its loss of functionality or both, it damages organs until they are not able to accomplish their task anymore, which eventually causes death of the host. Often, the organism does not fight against this aggression since it is not identified as a threat. Symptoms may be often visible only at a very advanced stage of cancer development, which makes therapies less effective and personalized treatments more favorable for cancer therapy [64, 80].

According to World Health Organization, cancer was responsible for 7.6 millions cases of death in 2008, which makes cancer a leading cause of death worldwide (around 13% of all deaths). Among them liver cancer is the third most killing cancer with 695000

deaths and the Hepatocellular carcinoma (HCC), variant of liver cancer, is involved in the 78% of them. Most of the time, HCC develops out of hepatitis or cirrhosis. For instance, in France, the number of cases is constantly increasing [1] and generally, the number of patients tripled between 1975 and 2005 in western countries [2]. Obviously, the human and economic impacts of this disease are important and have driven a large amount of investments in research to cure liver cancer. International agency for research on cancer (IARC) has a budget of about 38 billions of dollars every 2 years. The new plan for the fight against cancer in France amounts to 732 million euros for the 2009-2013, of which 95 million are invested in research. The ARC alone spent 21 millions euros in the last decade. In this context, every success in comprehension on HCC is valuable. However, despite the large progress accomplished, cancer remains a very difficult question. Medicine and biology looked for contributions from every domain of science to tackle this disease.

For this reason, mathematicians and computer scientists have been solicited and models start to emerge. Nowadays, models are more and more directly compared to biological data. As an example, the reader can refer to [75] where the authors make predictions using an *in silico* model. Along this spirit we here aim to contribute to the understanding of the emergence of HCC, its initiation and development, by using numerical simulations based on a mathematical model. A map of the genetic events presented in [38] is not known for HCC but, according to [62, 30], it shall involve at least three pathways: the p53, RB and Wnt/β-Catenin signaling transduction pathways (STPs). Mutations on β-Catenin genes are involved in 12-26% of human HCC[16]. In [15], the authors developed a mouse model to understand the role of the Wnt- and Ras-pathways in HCC. This model is described in 3.1.3 and constitutes the main source of biological material of the presented work. Before a detailed description of the mouse model and its results, we summarize some general aspects on the liver and its components.

3.1.2 The liver: function and organization

In brief:
The liver has a crucial role in the organism as it synthesizes and metabolizes molecules by uptake of certain metabolites and release of metabolic products back to the blood. Moreover it removes toxins from the blood. To succeed in this task, the liver is endowed with a particular architecture and different specialized components. Regeneration of liver architecture after toxic damage has been shown to result from an interplay of physical forces and cell-kinetic interactions of liver components. Hence a model mimicking carcinogenesis must take into account these components and forces. We briefly describe here the elements that we included in the model.

In [46], the subject is introduced as follows:

[1] source Association pour la recherche contre le cancer (ARC)
[2] source cancer.org

> "The liver provides functions required to maintain homeostasis in the organism. To accomplish this, the liver synthesizes numerous essential molecules of diverse sort; extracts and metabolizes a plethora of nutrients and xenobiotics brought into the body through the alimentary tract (and substances entering by other routes), as well as worn-out molecules and cells; stores, exports and/or excretes the metabolic products; and neutralizes numerous foreign antigens and microbes from the gut. These varied functions take place in a structurally complex, multicellular tissue with a unique angioarchitecture that has slowly evolved to its present form.
>
> Major features of liver structure are a functional tissue (parenchyma) composed of at least seven distinct types of cell – hepatocytes, cholangiocytes, sinusoidal endothelial cells (SECs), macrophages, lymphocytes of several different phenotypes, dendritic cells, and stellate cells – that conjointly possess the capacities to synthesize, metabolize and eliminate a wide range of complex molecules and to carry out immune functions, all arranged in a matrix that facilitates their cooperative interaction."

The authors emphasize the capital role of the organization and describes the blood flow in the liver:

> "The most fundamental feature of liver organization is a unique vascular pattern in which afferent (supplying) and efferent (draining) blood vessels of all sizes interdigitate uniformly, always maximally separated by parenchymal tissue and connected almost exclusively by the smallest capillary-size vessels (the sinusoids). Afferent blood vessels branch to form up to 8-10 orders of diminishing size from their entrance at the liver hilum; terminal portal veins, which supply blood to sinusoids, arise from the smallest two or three orders of preterminal portal veins. Sinusoids are interposed between afferent terminal portal veins and small efferent hepatic ('central') veins, which collect sinusoidal blood and merge to form larger hepatic veins. This vascular pattern provides a large volume of blood at a high flow rate through large vessels with high compliance and capacity to supply the sinusoids at a low flow rate and pressure. Total liver blood flow is large only because there are myriad sinusoids."

The smallest functional liver unit capable of performing the tasks described above is called lobule (see figure 3.1). The lobule reflects the disposition of the vasculature that yields a roughly hexagonal pattern composed about 4000 hepatocytes – the main cell type of the liver – in mouse [42]. In this functional unit, the spatial organization is made to maximize the contact surface among of the cells and the blood vessels. At the same time, the hepatocytes must be connected to create the bile network. These three components, the hepatocytes, the blood vessels and bile network are visible in figure 3.2 and 3.3. Hepatocyte is a differentiated cell with certain abilities that make this architecture optimal.

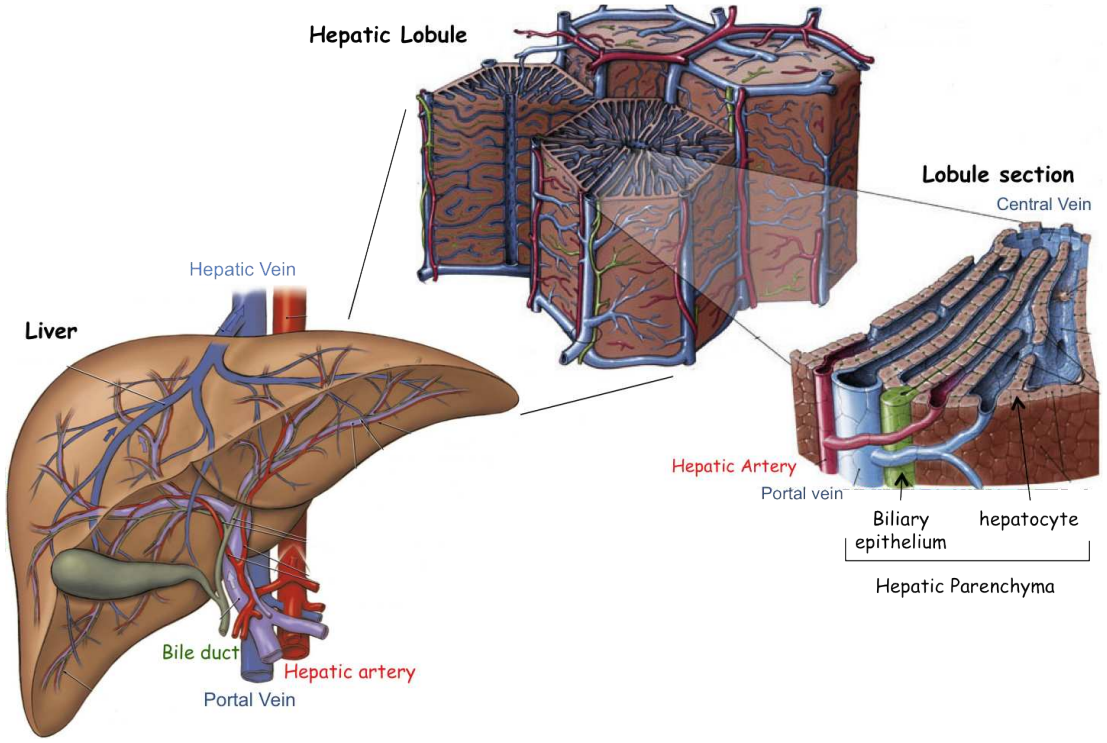

Figure 3.1: Organization in liver: From left to right, the scheme zooms in to illustrate different scales in liver. Left: the whole organ scheme illustrates the main role of the liver: filter the blood. Veins and arteries are split in myriad of capillary-size vessels and reassembled. Middle: the second scale – the lobule – shows how the space is organized to manage this task. Right: lobule section illustration presents the detail of the creation of the bile duct and the detailed architecture of a lobule that makes it functional. Image from embryology.ch

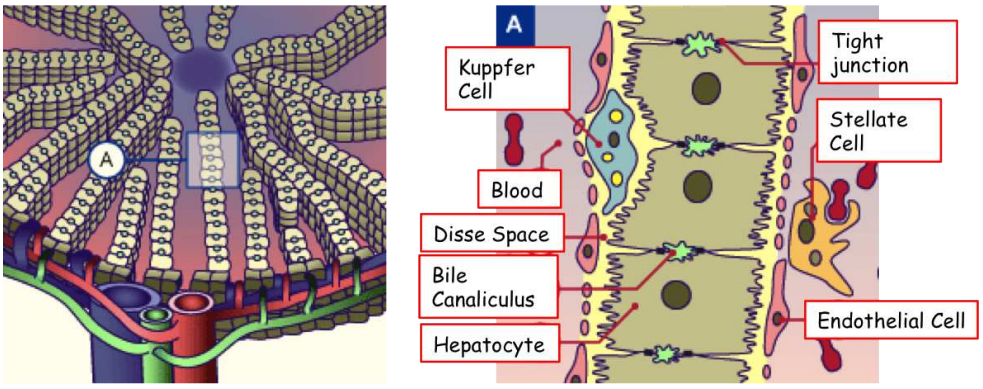

(a) Schematic liver lobule with columnar organization of the hepatocytes

(b) Spatial arrangement of the liver components

Figure 3.2: Organization in liver: (a) Schematic illustration of liver lobule and (b) magnification of internal organization of the components. (Images (a) and (b) from embryology.ch)

> "The hepatocyte, the major epithelial cell of the liver, performs many crucial functions that stem largely from its strategic position between two different environments, the blood plasma and the bile. The functions carried out at the two fronts are distinct, which means that the hepatocyte surface is asymmetric or polarized." [46]

The hepatocyte polarity defines the lobule architecture. Hepatocytes make tight-junctions with their hepatocyte neighbors and form the bile network (in green in figure 3.3(b)) and the rest of their surface is in contact with the blood network. The architecture is crucial because even hepatocytes with internal metabolic function correctly working could not carry out their task if the tissue is disordered. For instance in some cancer, tumor cells have genetic modifications that generally suppress cell specialization. In case of hepatocytes, if such a modification occurs, it can interfere on the cell capability to form bonds (loss of polarity) or it can decrease the contact surface to sinusoids, which would destroy the precise architecture and decreases the metabolic function of the liver. This is why, in the experiment described below, experimentalists stain the tumor obtained to quantify the differentiation of cells. A large part of the present work was devoted to explore this phenomenon (see section 3.4, 3.3.2, 3.3.2, 3.5)

The blood is transported from the portal vein and artery through the sinusoids to the central (hepatic) vein. The vessel network forms the structural support or "skeleton" of the liver and encompasses about 22% of the liver's mass/volume [33]. Sinusoid is a capillary vessel made of SECs with special properties:

> "[They] are penetrated by holes (fenestrae) and lack a basal membrane, features that allow free egress of the fluid components and solutes of the perfusing blood[...]. [SECs] are surrounded by a complex mixture of molecules.

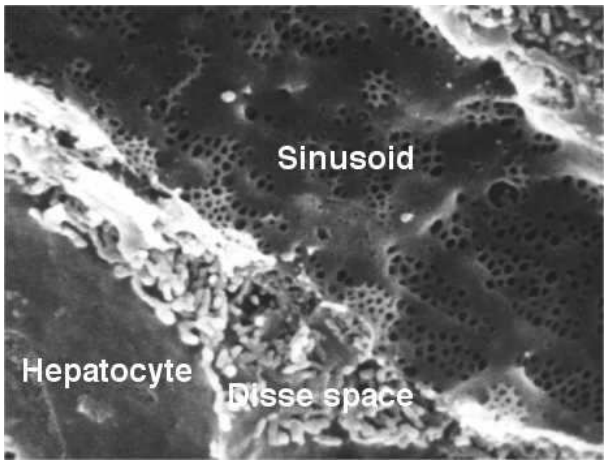

(a) Liver sinusoid. Scanning electron micrograph of a liver sinusoid with fenestrated endothelial cells. Image created by Prof. Robin Fraser, University of Otago, New Zealand and released into the public domain on 2006-05-22 as quoted below.

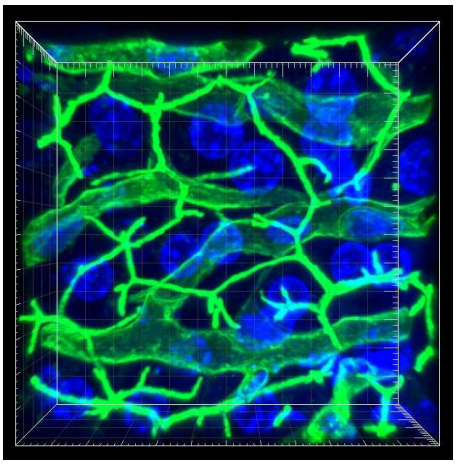

(b) 3D reconstruction of liver from confocal micrographies. Blue spheres are the hepatocyte nuclei, thin and full green lines define the bile network, clear and thick green lines the sinusoids. (Image from our collaborators at Ifado 5.1).

Figure 3.3: Organization in liver: (a) electron micrograph and (b) 3D reconstruction from confocal micrograhs.

> The unique structure of liver endothelium and sinusoids enables the free escape of fluid components of blood [...]"[46]"

Blood vessels play a crucial role as vasculature presents the skeleton of this complex architecture. However, the precise arrangement of cells within this skeleton is orchestrated by the balance of physical forces between the different constituents forming the liver. More details and results on biomechanics of the vasculature can be found in section 3.3.

Conclusion:
Here we presented the principles underlying mammalian liver in general, and mouse liver in particular. The spatial arrangement of liver constituents ensures that the liver functionality is optimized. Modifications in liver architecture decrease the organ performance. Liver function is guaranteed by different cell types and their complex organization. Cancer introduces perturbations leading to disorder in the tissue. To explain this disorder a mathematical model must reflect liver architecture and should describe the emergence of this architecture from the interplay of physical forces between the liver constituents (polarity, tight-junctions, vessel stiffness,...)

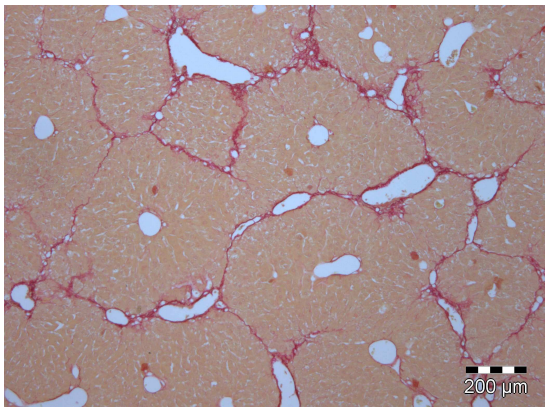

(a) Pig liver lobules. In pig, the connective tissue delimits each lobules (Image from our collaborators at Ifado)

(b) Representation of the lobules in the model for mouse. The lobule mosaic is obtained by coloring each hepatocyte in function of its closest central vein

Figure 3.4: Organization in liver: (a) in pig, the connective tissue enclosing each lobule makes lobules them more distinguishable from each other than in human or mouse liver. In the center of each lobule is a central vein and at the junctions between liver lobules are the portal triads, composed of the portal arterioles, portal venules, and bile ducts. (b) the liver model reproduction of the liver organization.

3.1.3 Mouse model and data

In brief:
Our collaborators at Institut national de la santé et de la recherche médical (INSERM) (see 5.1) established a transgenic mouse model to study HCC. We present here a summary and a description of the biological material. In the mouse model, *APC* downregulates β-Catenin that is involved in cell proliferation, cell-cell adhesion, and more generally in tumorigenesis [39]. Biologists are able to knock down the *APC* gene in mutant mice suppressing *APC* protein production, and thus causing upregulation of β-Catenin, which induces either excessive proliferation leading to the death of the mouse in short time or to tumorigenesis after a few weeks or months, depending on the quantity of a certain drug (*AdCre* / Tamoxifen) injected (see schematic illustration of the experiment in figure 3.5). Readers interested in details and methods can refer directly to [15].

In [15], biologists established a mouse strain to investigate whether (*i*) *APC* is functional in the liver and (*ii*) activating β-Catenin signaling is an oncogenic event in the liver. The mice have mutations on each strand of the DNA on the *APC* gene. The injection of *AdCre* can remove totally *APC* genes in the cell suppressing *APC* protein production. *APC* controls cellular levels of β-Catenin. Experimentalists look for β-Catenin immunoreactivity to detect *APC* inactivated cells. In the same way, β-Catenin can be in-

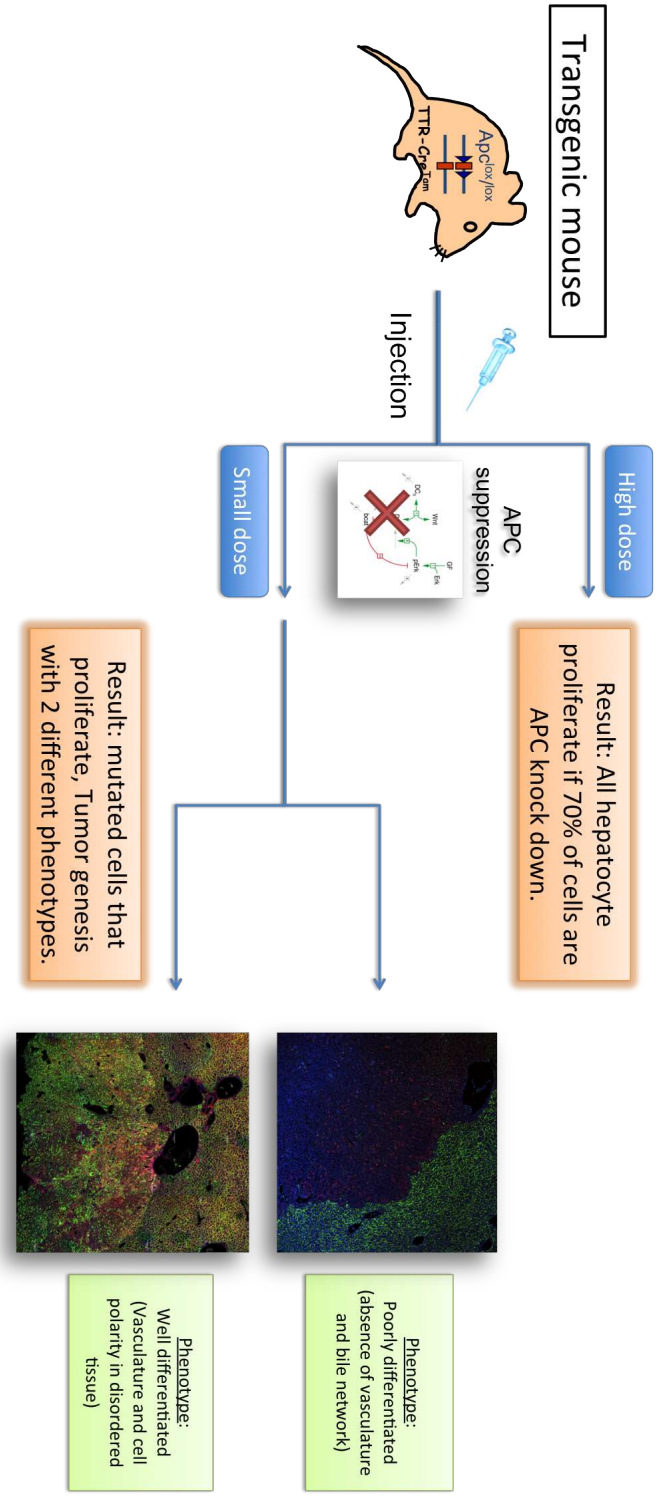

Figure 3.5: Experimental input: scheme of the pilot experiment that provided most of the biological material used in this chapter. High dose of *AdCre* injection induces a high cell proliferation that kills the mouse in a few weeks. A smaller dose is oncogenic and will initiate tumor with different phenotypes. We aim at understanding the intracellular mechanisms that trigger proliferation and the cause of the phenotypical difference among the tumor.

directly detected by immunostaining for GS, the product for one of its target genes in the liver. In this situation, GS staining indicates either normal β-Catenin activity (in this case a small about 2-cells-thick ring around the central vein in control mice), or overexpression of β-Catenin due to a loss of *APC* function leading to massive appearance of GS-positive hepatocytes.

High dose injection

After a single dose of 10^9 pfu of AdCre: the loss of *APC* in liver leads to a substantial mortality of the treated transgenic mice: 50% of the mice died within 2 weeks of the injection, and 95% died within 2 months. On day 7 after administration of 10^9 pfu of AdCre, mice presented a significant hepatomegaly, the livers being 60% bigger than those of the controls with higher number of proliferative hepatocytes. The 70–95% of the hepatocytes showed β-Catenin staining (direct and indirect, in nucleus and cytoplasm).

Diluted injection

After injection with 0.5×10^9 pfu of AdCre: 15% of the mice died within 2 months, whereas no mortality was observed with 0.25×10^9 pfu of AdCre. Ten $Apc^{-/-}$ mice were analyzed; four did not contain any GS^+ hepatocytes and developed no liver tumor. Among the six mice that still possessed GS^+ hepatocytes, four (67%) developed micro nodules for a total of nine tumors (see 3.1). These HCCs were histologically typed as: well differentiated (WD), moderately differentiated (MD) and poorly differentiated (PD). A molecular analysis was performed on the tumors and has shown that level expression of some genes decreased as the differentiation status of the tumor decreased. This has been confirmed by additional staining performed at Leibniz-Institut für Arbeitsforschung an der TU Dortmund (IfADo) (see description in table 3.2). In the well differentiated phenotype the tumor still shows a visible vascularization (ICAM-1 staining) and DPPIV staining indicating the bile canaliculi. The poorly differentiated phenotype is characterized by the absence of blood vessels within the tumor. Moreover, DPPIV – the marker labeling bile canaliculi – is absent in poorly differentiated tumors indicating the absence of bile canaliculi - and thereby the likely absence of tight junctions indicating missing adhesion among tumor cells (see figures 3.6 and 3.7).

Conclusion:
The authors of [15] demonstrated that (*i*) *APC* is functional in the liver and (*ii*) aberrant β-Catenin signalling is a genetic event able to initiate the development of HCC. In the case of a high dose of *AdCre* injection, they showed a threshold effect of *APC* depletion in liver (70%) to trigger hepatocyte proliferation. In the case of diluted dose injection, they produced and analyzed different HCC phenotypes. In the next sections, we present mathematical models that take into account this biological information and suggest explanations to these experimental results.

Mouse Id	No. of GS^+ cells in nontumoral tissue	No. of tumors WD	MD	PD	HCC size, mm
1	6	4	–	–	4.2, 2, 1.5, 2
2	3	–	3	–	20, 6, 8
3	1.8	–	–	1	0.5
4	1.3	–	–	1	3
5,6	0.6, 0.9	–	–	–	–

Mouse 1 was killed 8 months after *AdCre* injection.
GS-expressing cells in nonperivenous areas per 1,000 hepatocytes.

Table 3.1: **Hepatocarcinogenesis in $Apc^{-/-}$ mice** (reproduction of *Table 1* in [15])

Color	Name of the marker	What is labeled
Blue	DAPI	labels the cell nuclei
Green	DPPIV	labels the bile canaliculi (adhesion) on hepatocyte's membrane. Ideally, it should only color the bile-side of the hepatocytes (as it is a polarity marker) but it additionally stains parts of the sinusoidal cell membrane.
Red	ICAM-1	labels SEC
Yellow	ICAM-1 and DPPIV	Indicates a co-staining of ICAM and DPPIV (both are present) and reveals (after some image processing) the location of the sinusoids. In ICAM/DPPIV images what is in green (but not yellow) is bile canaliculi.

Table 3.2: **Staining information** (comments Stefan Höhme)

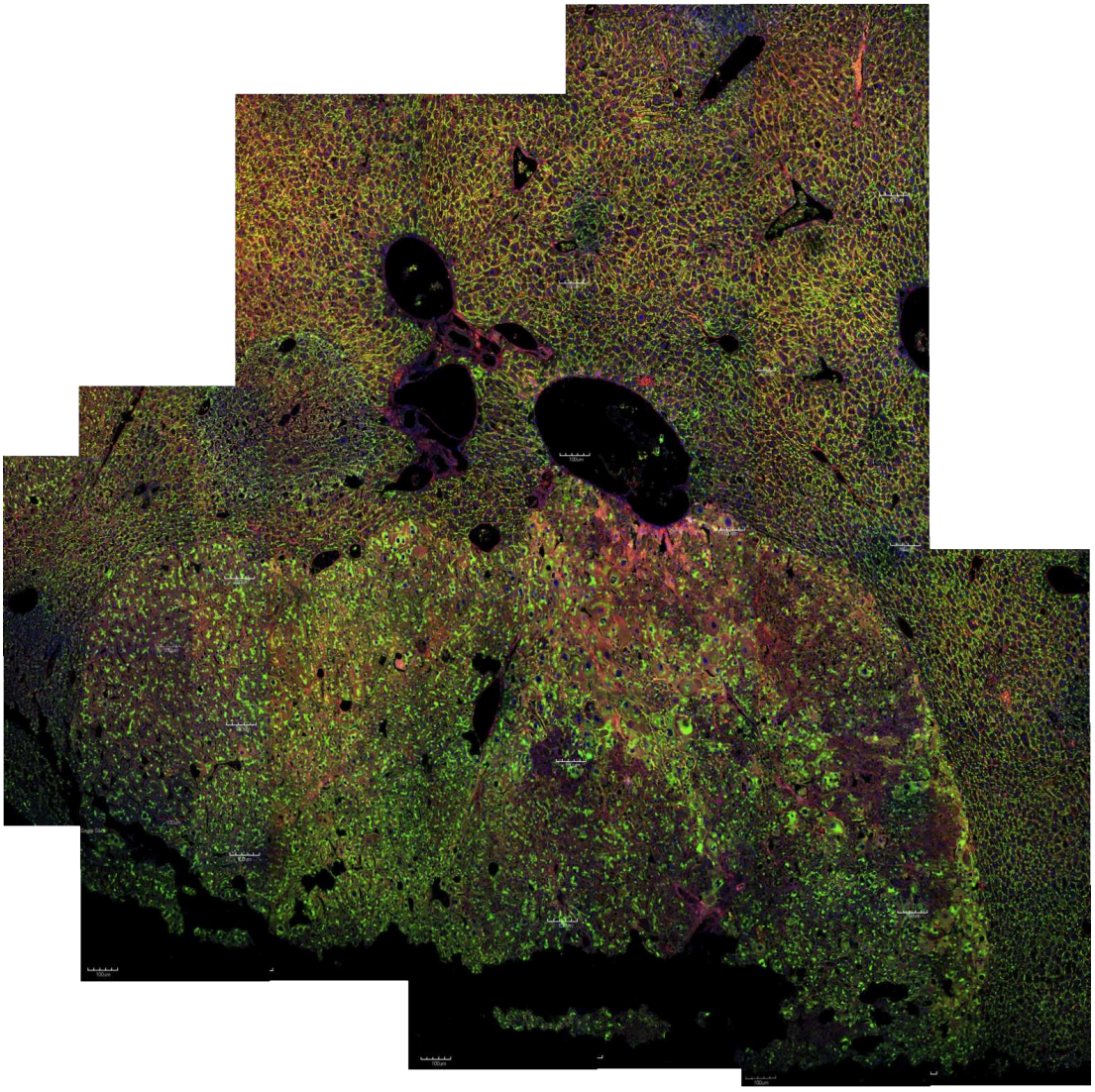

Figure 3.6: Experimental result: well differentiated tumor. The tumor shows visible vascularization (ICAM-1 staining) and DPPIV staining indicating the bile canaliculi. See table 3.2 for staining description. Experimental data from Colnot et al., INSERM, staining from IfADo. Scale bars size is 100 micrometers.

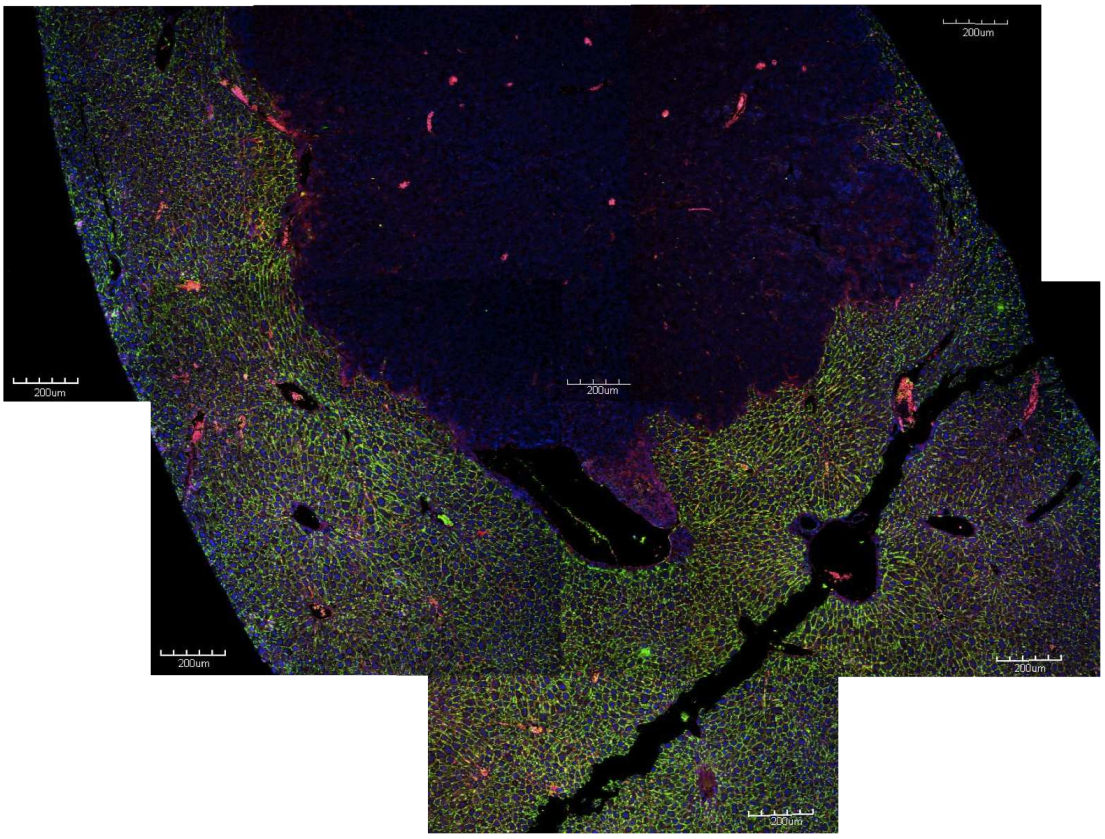

Figure 3.7: Experimental result: poorly differentiated tumor. The absence of ICAM-1 staining suggests that there are no blood vessels within the tumor. DPPIV is not present indicating the absence of adhesion among tumor cells. See table 3.2 for staining description. Experimental data from Colnot et al., INSERM, staining from IfADo. Scale bars size is 100 micrometers.

3.1.4 Specificities of the liver model

In brief:
Starting from the model [44] validated in *in vitro* cases and [43] validated on biological *in vivo* data, we composed an extended model to study the liver tumorigenesis and to reproduce experiments of the mouse model presented above (section 3.1.3) *in silico*. This Section describes additional model specifications and assumptions. The full mathematical model and its implementation are described in Chapters 1 and 2. We used the data extracted in [42] to build a representative sample of lobules. We describe here the novelties introduced.

The questions raised by the experiments explained in 3.1.3 were new and have not yet been addressed by [43] on liver regeneration or by [41] on multi-cellular spheroids. They require a realistic model of tumorigenesis in a realistic organ environment, namely, in a group of liver lobules. The mathematical model of section 1 has been taken as a starting point and was iteratively extended and refined as a result of intense interactions with biologists and experimentalists. As in our simulations uncontrolled production of liver tumor cells led to a high accumulation of tumor cells close to the blood vessels, the forces occurring between cells and vessels could be significantly larger than those observed during liver regeneration. Accordingly, the time step size in the simulations had to be significantly reduced and a large effort had to be devoted on solving numerical implementation issues to face the challenge of a large liver section. We present here the list of new mechanisms, rules and configurations. For several cases, we consider a number of alternative model variants. For the equations, see section 1.1.2.

We explored the mechanisms and parameters of the model to observe the differences in case of liver carcinogenesis. Due to a large number of possible combinations of the mechanisms each combination determining a possible tumor cell phenotypes, many simulations had to be done. We present in the next sections of this chapter a selection of the most interesting and realistic ones and the meaningful results.

1 – Initial State : The model simulates a liver section composed of 9 lobules. The precise model set up was sampled from data obtained from a statistical analysis of confocal laser scanning micrographs hence each individual lobule represents a "representative" liver lobule [42]. The multi-lobule was designed with parameters extracted from the lobule architecture and liver components: central veins, portal veins, sinusoids and hepatocytes (see appendix 5.2). Other parameters were taken from literature. To avoid adding too many parameters and modeling the difficult problem of the Glisson capsule (elastic tissue that encapsulates the liver), the spatial domain is periodic at its boundary in the three directions. The size of this liver section is $75 \times 75 \times 7$ (in hepatocyte diameters i.e $23.3 \mu m$). The schematic liver lobule is often represented hexagonal but the reality suggest a lobule tessellation closer to a Voronoi diagram (see figure 3.4). For this reason, we distributed

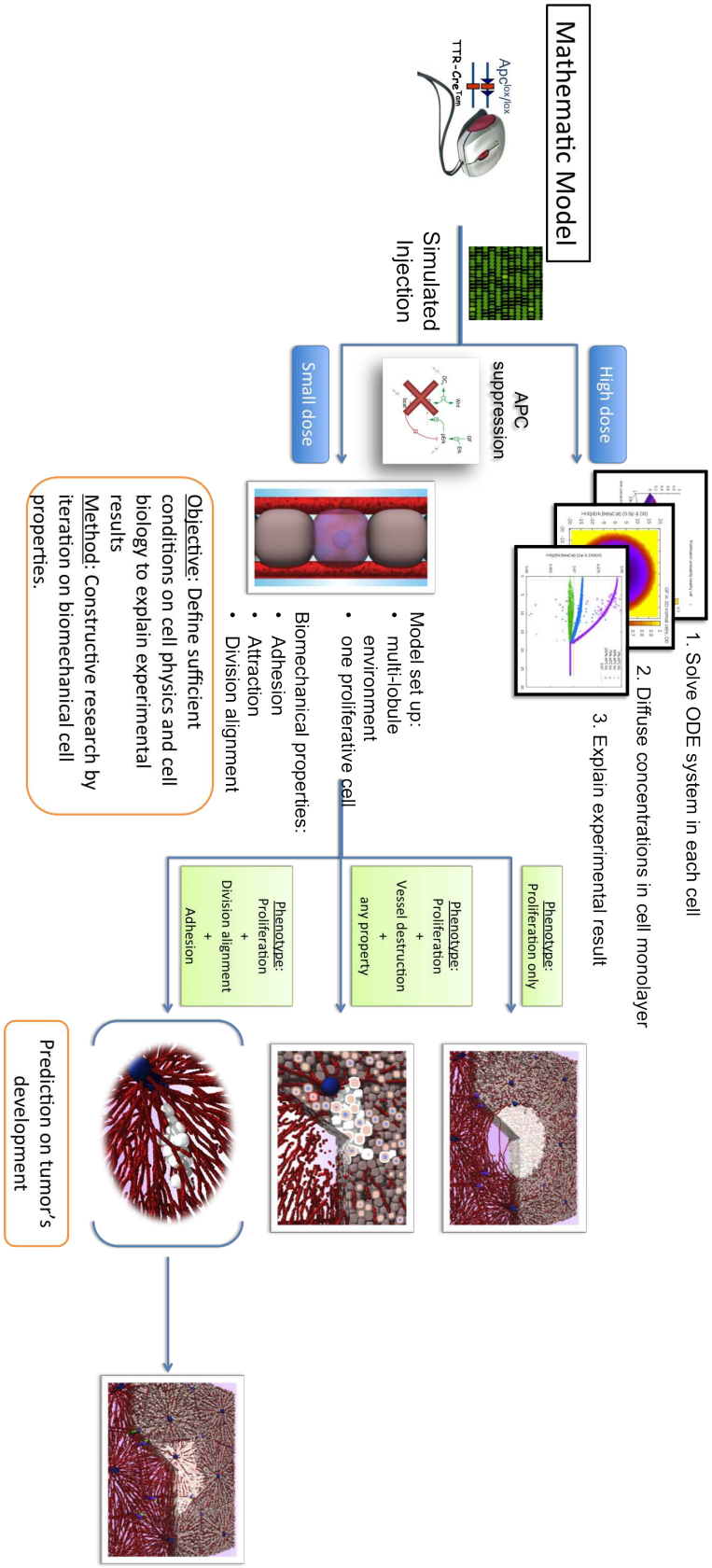

Figure 3.8: Models from experimental input: Model integration of the experimental input (3.5): work aims and methods.

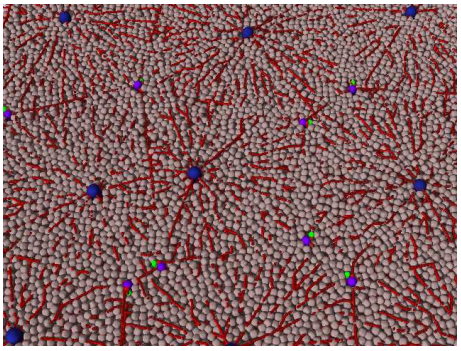

(a) View of liver at simulation start.

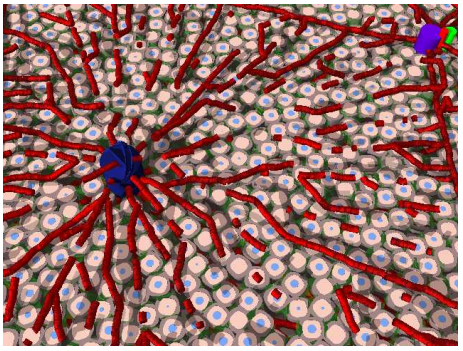

(b) Magnification of the left image cut at the top.

Figure 3.9: Liver model: Initial state of the model. The simulation starts in a periodic multi-lobule environment. (a) In brown, the hepatocytes and red the sinusoids. The central vein is dark blue and portal triad is made of one portal vein in light purple, one hepatic artery in red and bilary duct in green. In the magnification (b), the blue circles represent hepatocyte nuclei. The light brown is the cell cytosol and the dark brown is the cell membrane. The transparent green arrows on cells are the adhesive poles of hepatocytes.

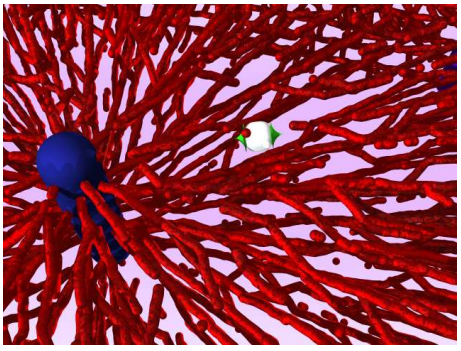

(a) View of the initial states without healthy hepatocytes. Only vasculature and the first initial tumor cells is represented.

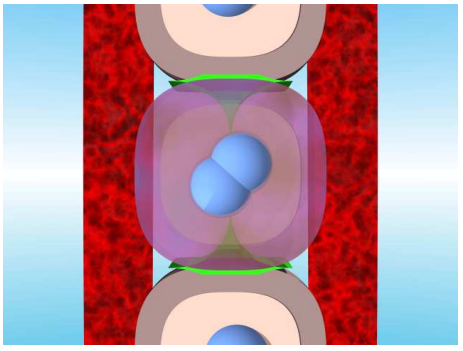

(b) Schematic view of the hepatocytes embedded in is sinusoid environment.

Figure 3.10: Liver model: Model starts with one tumor cell in the center lobule of the multi-lobule environment of 8 lobules enclosing the center lobule. The tumor cells may be either polar or not (here the green arrows shows a polar tumor cell). In real and virtual liver, hepatocytes, the main parenchyme cell type of liver are aligned in columns along the sinusoids.

randomly on an hexagonal tessellation the central veins and used a Voronoi-Delaunay library from Nick Jagiella (see 5.1) to determine the portal triads. Once an arrangement of 9 lobules is obtained, it is mirrored to connect the vessels at the periodic boundaries. Before each tumor growth simulation, a relaxation simulation is performed with the configuration in order to avoid artifacts.

2 – Proliferation : We assume that cells are able to re-enter the cell cycle only if the local pressure does not exceed a critical value p_q (we used the principle of Biomechanical force for inhibition (BFI) explained in Section 1.1.2, the pressure is sum of the forces divided by the contact area). This value is assumed to be larger for tumor cells than for normal cells as tumor cells are known to be insensitive to contact-inhibition of proliferation. Above a second pressure threshold computed again with the forces and the contact area (we refer to these forces as Biomechanical force for apoptosis (BFA)) $p_d > p_q$, cells die. This assumption has been shown and is able to explain homeostasis inside monolayers [23]. Note that this assumption fits into the concept of "homeostatic pressure", recently suggested by Basan et. al. in [7] to explain tumor expansion. However, we assume that the pressure is only sensed in G_1 and G_0. Once a cell has passed S-phase it is committed to proceed until division. In the simulations of this work we have chosen the tumor death threshold p_d^t high enough so that death of tumor cells did not occur. This setting of the death threshold was motivated by the finding that neither necrosis nor apoptosis was observed in the experiments. We explored different parameters for the tumor's proliferation threshold. For normal hepatocytes $p_q^n = 0$ so that cells only proliferate if neighbor cells die. $p_d^n = 3$ kPa (kilo Pascal) is enough to avoid any healthy cell death.

3 – Dumb-bell system : Additionally to the Monte-Carlo simulation that evaluates orientation changes based of the change of the potential energy, we consider equations for the torques. The equation for the torques of each cell can be calculated using the same external forces as in the equations for the cell migration. This leads to a larger consistency as in both, the equations for the torques and for the cell mass shifts, the same forces can be used, and complex interactions be represented. During the mitosis cells may rotate because of an asymmetric shape (a dumb-bell) and modify polar interaction with other hepatocyte to form tight-junctions and the resulting bile canaliculi network.

4 – Division axis : In simulations that take place in a multi-lobule environment the division axis of cells can be set randomly and uniformly distributed, in the direction of cell polarity, or parallel to the closest sinusoid. We call the latest assumption Hepatocyte sinusoid alignment (HSA).

5 – Micromotility : The random component in the cell motion (a) can be biased in the direction of locally lowest pressure or (b) can be uniformly distributed.

6 – Cell type adhesion :

1. Tumor cells do not adhere to hepatocytes or to sinusoids.

2. For hepatocytes, we tested two variants. (a) No adhesion to tumor cells and sinusoids, but adhesion to other hepatocytes. (b) When a tumor cell comes in contact with a healthy cell, then the cell-cell contacts of the healthy cell with its neighbor cells are destroyed. This mimics the effect of short-range proteolytic enzymes secreted by tumors cells on cell-cell contacts.

3. Hepatocyte/SEC adhesion, Tumor/SEC adhesion.

7 – Polar adhesion : The cell-cell adhesion contacts of both, normal hepatocytes and tumor cells can be either polar or non polar. The polar angle can be set differently for healthy and tumor cells.

8 – Environment : Simulations take place either in a nine lobules environment or in a full box of hepatocytes with no vessel network. Both configurations have the same size and periodic conditions. The aim of studying tumor growth without any vasculature is to establish a reference situation where the growth of the tumor (especially its shape) is not driven by the vessel architecture.

9 – Pressure measurement : The pressure on a cell is the sum of all forces divided by the contact area where the force is exerted. Hence, in absence of cell-cell adhesion, all contributions are positive while in presence of cell-cell adhesion, the total pressure can be negative (tension) or positive. In simulations it can make sense to study negative and positive pressures, or to consider only the positive compressive contribution of the cell-cell interaction even in case adhesive interactions are present. For this reason we consider both measures in our simulations.

10 – Pressure gradient preferred move : The random component in the cell motion can be biased in the direction of locally lowest pressure.

11 – Morphogen attraction : Sinusoids release a morphogen that attracts hepatocytes. We model this SEC morphogen chemoattraction either on all cells or on tumor cells only.

12 – Cell/Cell adhesion desctruction : When a tumor cell comes in contact with a healthy cell, then the cell-cell contacts of the healthy cell with its neighbor cells are destroyed. This mimics the effect of short-range proteolytic enzymes secreted by tumors cells on cell-cell contacts.

13 – SEC proliferation and death : SECs growth may either be induced by vessel stretch or by a signal [19]. SEC death is induced by pressure. If a SEC in contact with tumor cells experience a pressure above a certain threshold, it dies. Technically, a SEC divides, a node is added and connected to the local nodes of the graph. When a SEC dies, the links with other nodes in the graph are removed.

14 – Individual parameter variations : Most of the parameters are not global but individual for each cell. However, in most of the simulation, we distinguish 3 distinct sets of parameters for 3 distinct populations: healthy, tumor and endothelial cells (the endothelial cells make up the sinusoids). For each of the three sub-populations, we can vary the parameters for mechanical softness (Young modulus, Poisson ratio), medium friction, cell-cell friction (every combination of cell: tumor, healthy, endothelial), polar angle, cycle-time, pressure threshold, etc.

Conclusion:
Due to the cancer nature, agent-based models might be naturally well suited to help in the understanding of early carcinogenesis. The most general cancer definition could be: “an abnormal cell proliferation caused by genetic mutations”, expressing the monoclonal character of cancer formation. In agent-based models, where each cell is modeled individually, it is practical and immediate to add or remove cell properties. The difficulty is to identify the relevant properties, if they are changed by a certain mutation and - in case they are changed - when they are changed. Cells are very complicated and complex objects and it is today impossible to pretend to model them in complete detail. The modeler must choose plausible assumptions and infer what is missing by comparison to the biological information available. From the point of view of systems theory, cancer causes a perturbation in the system. The impact on the system in the individual case depends on what, where and how the perturbation takes place. We used the biological information on liver carcinogenesis and adapted our model for liver to answer certain questions that experiments only can hardly resolve.

3.2 Mathematical modeling of β-catenin and Ras signaling in hepatocyte and its impact on proliferation, tissue organization and formation of hepatocellular carcinoma

In brief:
As a proof of concept we first integrated a simplified model of the Wnt and β-catenin – signal transduction pathway into the multi-cellular model. We perform here integration into a monolayer and choose the boundary condition in analogy to those in a liver lobule. We have chosen this intermediate step – the test of the intracellular model in a monolayer resembling a liver lobule cross-section – as it is much less simulation time intense than the full multi-lobule model. Moreover, it isolates important phenomena on intracellular pathways that could be hardly distinguished from other phenomena in a more complex system.
In a fundamental first step we study if Wnt and Ras signaling pathways can explain the observation of [15], that instantaneous proliferation in $Apc^{lox/lox}$ mice can only be observed if around 70% of the hepatocytes become $Apc^{-/-}$. In the experimental model this is performed by administration of 0.5×10^9 pfu AdCre. For consistency we initially used an intracellular model provided by our collaborators in the CancerSys project at Charité at Humboldt university of Berlin (see 5.1). It turned out that this model is insufficient to explain the aforementioned proliferation – threshold – like behavior at 70%. We integrated a further function of APC-knockout, namely the assumption that β-Catenin acts as a transcription factor of TGF-alpha, which then is secreted into the extracellular space and able to activate the Ras pathway by binding to the EGF-receptor. TGF-alpha is furthermore assumed to diffuse and hence can serve as a messenger molecule informing other hepatocytes of the existing APC knockout cells. We find that if both the production of TGF-alpha as well as its diffusion are fast enough, it is possible to define a growth factor threshold concentration at which cell cycle entrance occur such that the experimentally observed proliferation threshold behavior in $Apc^{lox/lox}$ mice at about 70% knockout can be mimicked. TGF-alpha production had to be strong enough such that the local growth factor concentration exceeded that in the extracellular medium.

3.2.1 Introduction

In order to predict the effect of molecular manipulations on multi-cellular organization, mathematical models of multi-cellular tissues must present the link between the molecular alphabet and the cell phenotype [72] [71]. In the transgenic mouse stem considered in this project, Wnt and Ras STPs are believed to play an important role in the development of HCC [11, 79, 78]. For this reason, many investigations were done in the CancerSys project

and Wnt and Ras STPs were included into a multi-cellular model [1, 52, 69].

As shown in [15] Tamoxifen triggers GS positive hepatocytes in $Apc^{lox/lox}$ mice. The fraction of GS positive hepatocytes depends on the dose of Tamoxifen administered. GS is a target of β-catenin hence GS positive hepatocytes reflect nuclear presence of β-catenin. If the fraction of GS positive hepatocytes exceeds about 70% then hepatomegaly linked to hepatocyte proliferation was observed. Tumor formation was observed 8 or 9 months after administration of 0.5^9 pfu of Tamoxifen in six of 10 mice. From these observations it is clear that the individual hepatocyte must be able to detect how many other hepatocytes are GS positive. Findings by [78] suggest that TGF-alpha expression is triggered by β-catenin as the TGF-alpha gene is also a target of β-catenin. TGF-alpha is then secreted outside the cell, and binds to the EGF receptor activating the Ras pathway. As it can diffuse, it can bind to the EGF-receptor of the same cell that secreted TGF-alpha as well as to the EGF-receptor of neighbor cells. As the model simulations in liver are very complex and time-consuming – already without including the intracellular model, we consider as a very simplified multi-cellular arrangement a monolayer representing a liver slice as we did previously in [42] to study liver regeneration after CCl4-induced damage. So far, the intracellular model considered a generic growth factor (named "GF") as well as Wnt. The findings described above propose that TGF-alpha has to be considered in addition. Accordingly, we first explain the intracellular model, extended by the production of TGF-alpha. In a second step we will explain how the growth factor and Wnt diffuse in our model. Then we will show simulations in the monolayer situation where the number of cells has been calibrated to those in a liver slice. The transition from liver slice to the full multi-lobule model is straightforward as the same software tool is used for both.

3.2.2 Normal hepatocytes: the intracellular model

We extend the intracellular model finally set up in the EU - project CancerSys for normal hepatocytes by our collaborating group lead by Nils Blüthgen (with no mutations or APC depletion). For reasons of consistency we use the same parameter values for those model parts taken from our collaborators work. The simulations in the full liver multi-lobule model are currently on the way.

Schematic model representation

Here we describe the scheme shown in figure 3.11. "Step n" denotes the considered process, denoted by the rate constant k_n.

1. Transformation of the free destruction complex DCF into the receptor destruction complex DCR through Wnt stimulation. In fact, Wnt signaling requires the inhibition of Glycogen Synthase Kinase 3 (GSK3) activity through the recruitment of the free destruction complex DCF to the plasma membrane which then binds to a receptor complex.

2. Degradation of DCR through endosomes, multivesicular bodies, and possibly exosomal secretion.

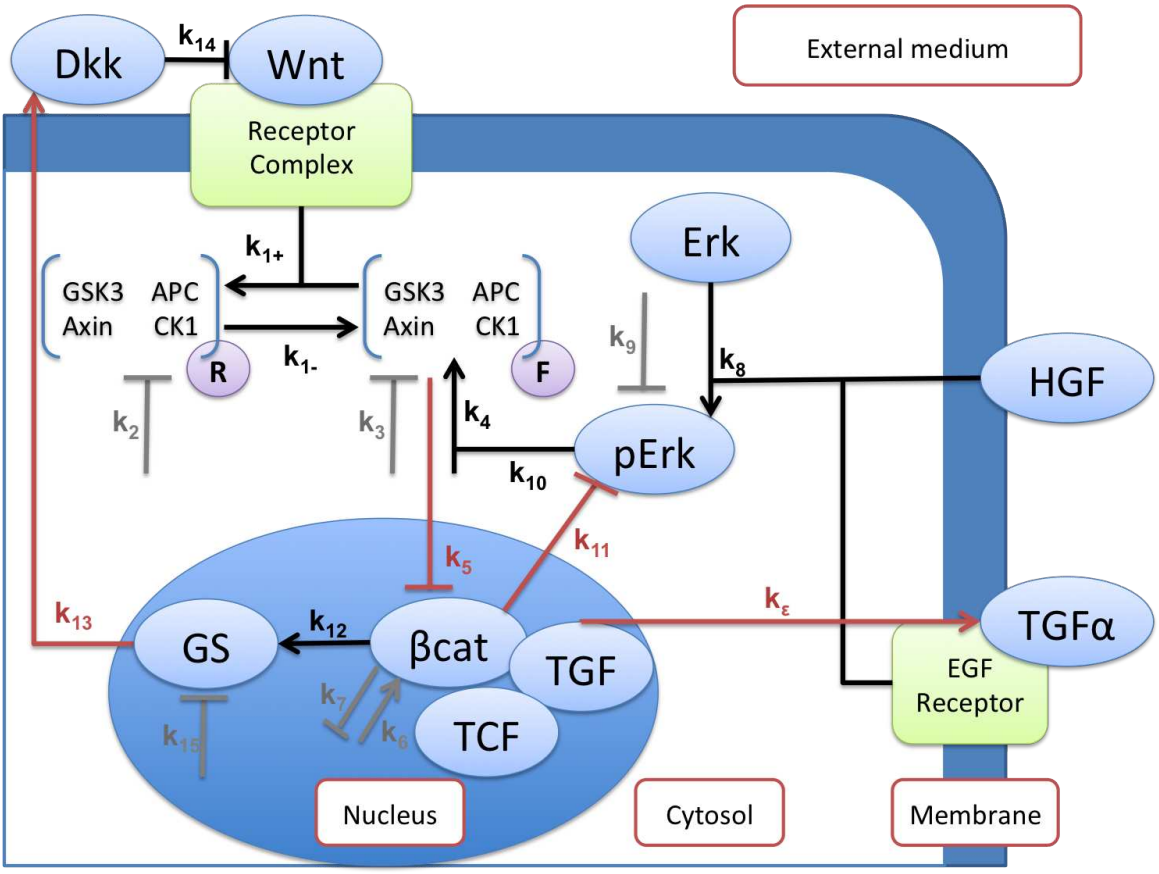

Figure 3.11: Scheme of Wnt and Ras pathway signaling used in our model. Ras is not explicitly shown here. GF (represented here exemplarily by HGF) and TGF-alpha activates Ras, leading to downstream activation of Erk. The different reactions are explained in the text in 3.2.2. For a better readability of the scheme we place β-catenin production in the nucleus. Actually, β-catenin is formed in the cytosol but triggered by expression of genes in the nucleus. It can then enter in the nucleus and binds to transcription factor.

3. Degradation of the unbound form of the destruction complex (DCF).

4. Natural production of DCF.

5. Inhibition of β-Catenin by DCF by phosphorylating β-Catenin thus marking it for protosomal degradation.

6. Another form of β-Catenin synthesis.

7. Another form of β-Catenin degradation.

8. Transformation of Erk into phosphorylated Erk, pErk, through HGF stimulation.

9. Degradation of pErk.

10. DCF production activation (more precisely of the APC complex component) by pErk.

11. Inhibition of pErK by β-Catenin.

12. Production of GS if β-Catenin concentration in a hepatocyte exceeds a certain β-Catenin threshold in the cytosol.

13. Production of Dkk if β-Catenin concentration in a hepatocyte exceeds a certain β-Catenin threshold.

14. Negative feedback produced by Dkk into this network. Dkk inhibits Wnt signaling through competing for the same receptors as Wnt.

15. Degradation of GS by the proteasome.

16. ε describes the production of TGF-α which is secreted in the medium once β-Catenin accumulates and translocates in the nucleus through APC knock-out (when β-catenin translocates into the nucleus then it binds to Tcf/Lef transcription factor leading to expression of the Tcf-related target genes such as TGF-α [78]). TGF-α is secreted into the extracellular space where it binds to the EGF receptor. As TGF-α can diffuse, it can bind to the EGF receptor of the secreting and of adjacent cells.

Dkk (steps 13 and 14) is believed to play an important role in zonation but is not considered below. The reader can report to [55] for more details.

Mathematical model representation

$$\frac{d[DC_R]}{dt} = k_{1^+}[Wnt][DC_F] - k_{1^-}[DC_R] - k_2[DC_R] \tag{3.1}$$

The term $-k_{1^-}[DC_R]$ represents the dissociation of DCR from the membrane.

$$\frac{d[DC_F]}{dt} = -k_{1^+}[Wnt][DC_F] + k_{1^-}[DC_R] - k_3[DC_F] + k_4(1 + (k_{10}[pErk])^n) \tag{3.2}$$

$$\frac{d[pErk]}{dt} = k_8[HGF][Erk] - k_9[pErk] - k_{11}[pErk][\beta cat] \tag{3.3}$$

$$\frac{d[\beta cat]}{dt} = -k_5[DC_F][\beta cat] + k_6 - k_7[\beta cat] \tag{3.4}$$

$$\frac{d[Wnt]}{dt} = D_{Wnt}\Delta[Wnt] - \mu_{Wnt}[Wnt] \tag{3.5}$$

where D_{Wnt} is the Wnt Diffusion constant and μ_{Wnt} is the Wnt degradation constant and n a natural number ¿ 1. We furthermore assume that Wnt adopts a maximum value at the central vein which, we here identify with the center of the (mono-)layer.

$$\frac{d[Dkk]}{dt} = D_{Dkk}\Delta[Dkk] + \rho_{Dkk}F([Dkk]) - \mu_{Dkk}[Dkk] \tag{3.6}$$

where D_{Dkk} is the Dkk Diffusion constant, ρ_{Dkk} is the Dkk production constant and μ_{Dkk} is the Dkk degradation constant. F is mimics Dkk production. In the current model, we do not consider Dkk.

if β-Catenin exceeds a certain threshold of β-cat (β-cat > β-cat threshold)

$$\frac{d[GS]}{dt} = k_{12}[\beta cat] - k_{15}[GS] \tag{3.7}$$

If β-cat does not exceed the threshold:

$$[GS] = 0 \tag{3.8}$$

We further make a number of assumptions:

The total destruction complex is given by the mass conservation:

$$[DC] = [DC_F] + [DC_R] \tag{3.9}$$

We assume that the degradation of the two forms of the destruction complex DC_F and DC_R occur at the same rates:

$$k_2 = k_3 = k_{DC} \tag{3.10}$$

Receptor internalization normally happens within 15min, see [37]. And since there's evidence that the destruction complex needs to be bound to the receptor complex before it

can be internalized [37], receptor complex binding needs to be faster than internalization (<15min). For this reason, we assume that the variation of the DC_R in time is very small and consider the steady state for DC_R:

$$\frac{d[DC_R]}{dt} = 0 \tag{3.11}$$

It is assumed that the dissociation of the receptor complex from the receptor is much faster than the degradation of the receptor bound destruction complex. In fact, the degradation of the receptor bound destruction complex happens mainly via internalization and exosomal degradation. We suppose: $k_{1^-} >> k_2$

The total amount of Erk (denoted by superscript "T") is conserved and the sum of activated (phosphorylated) and non-phosphorylated Erk is constant:

$$[Erk^T] = [Erk] + [pErk] \tag{3.12}$$

We also set the derivative of pErk with respect to time to zero as pErk reaches the steady state instantaneously because of the rapid phosphorylation of Erk [54].

$$\frac{d[pErk]}{dt} = 0 \tag{3.13}$$

and for simplicty we set $[Erk^T] = 1$

Because of the slow diffusion of Wnt molecule caused by palmitoylation, Dkk diffusion is much faster than Wnt diffusion [81]: $D_{Dkk} >> D_{Wnt}$

With these assumptions we find:

$$\frac{d[DC]}{dt} = -k_{DC}[DC] + k_4(1 + (k_{10}[pErk])^n) \tag{3.14}$$

$$[DC_F] = \frac{[DC]}{1 + k_{16}[Wnt]} \tag{3.15}$$

$$k_{16} = \frac{k_{1^+}}{k_{1^-}} \tag{3.16}$$

$$[pErk] = \frac{[HGF][Erk^T]}{[HGF] + k_{17} + k_{18}[\beta cat]} = \frac{[HGF]}{[HGF] + k_{17} + k_{18}[\beta cat]} \tag{3.17}$$

$$k_{17} = \frac{k_9}{k_8} \tag{3.18}$$

$$k_{18} = \frac{k_{11}}{k_8} \tag{3.19}$$

The equation for the free destruction complex becomes:

$$\frac{d[DC]}{dt} = -k_{DC}[DC] + k_4 + \left(\frac{k_{10}[HGF]}{[HGF] + k_{17} + k_{18}[\beta cat]}\right)^n \tag{3.20}$$

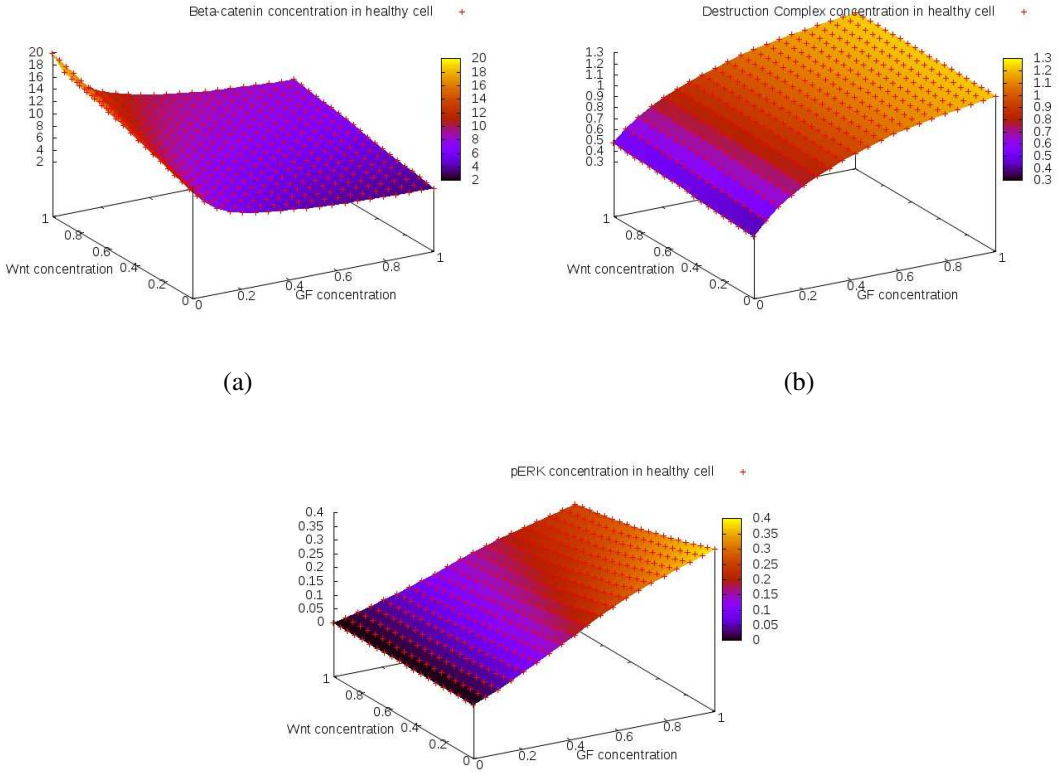

Figure 3.12: Steady state in normal (healthy) hepatocytes. (a) β-Catenin, (b) free destruction complex $[DC_F]$ and (c) $[pErk]$ as a function of the Wnt and GF concentration in the range $[0:1]$ following the normalization of our collaborators on the EU-project CancerSys.

Hence, if HGF (representing growth factors) is zero, then $[DC] = \frac{k_4}{k_{DC}}$

$$\frac{d[\beta cat]}{dt} = -k_8 \frac{[DC]}{1+k_{16}[Wnt]}[\beta cat] + k_6 - k_7[\beta cat] \tag{3.21}$$

We further assume the following initial conditions: $[DC](0) = 0$ and $[\beta cat](0) = 0$

Figure 3.12 shows the concentrations of β-Catenin, free destruction complex, and pErk as a function of the Wnt and GF concentration for healthy hepatocytes. In the steady state, β-Catenin and pErk both become a function of the GF and Wnt concentration. For normal cells, $k_4 \neq 0$. Hence free destruction complex is always produced.

In case of a *Apc Knock-out*, $[DC]$ = 0 leading to $[\beta cat] = \frac{k_6}{k_7}$. On the other hand, zero Wnt-concentration increases the decay of $[\beta cat]$ but due to the constant production rate $k_6, [\beta cat] > 0$. Moreover, for $Apc^{-/-}$ cells, $k_4 = 0$. Hence, free destruction complex is not produced and consequently β-Catenin not degraded. The resulting functions for

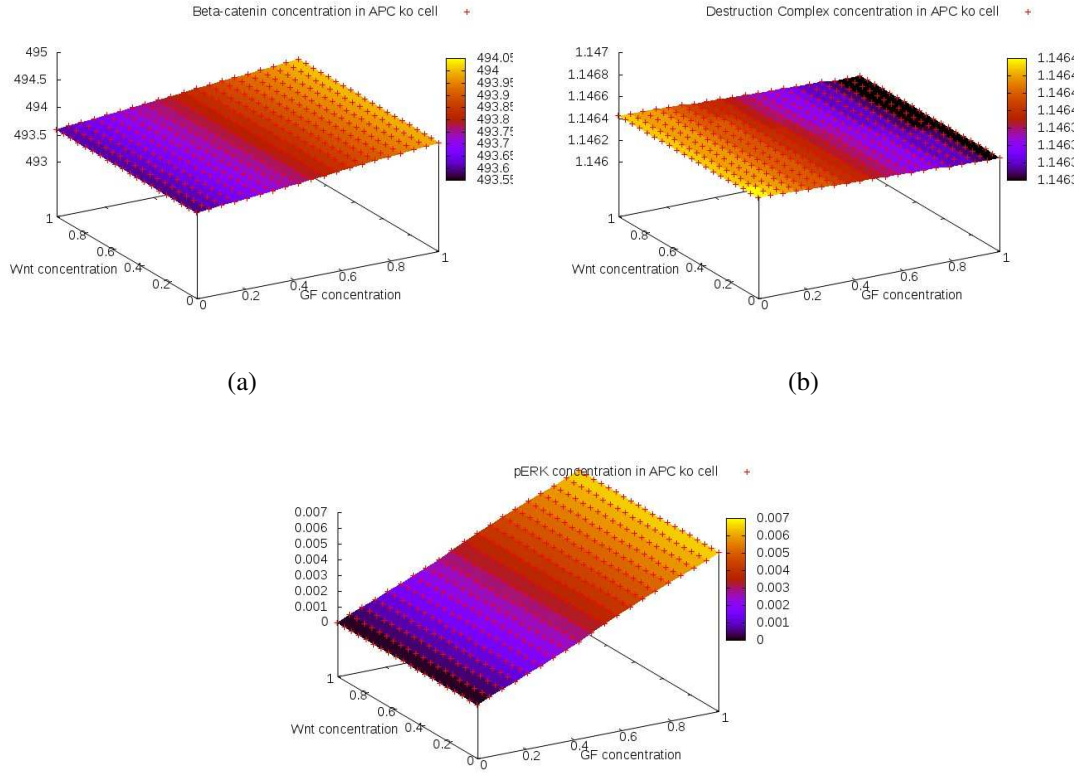

(a) (b)

(c)

Figure 3.13: Steady state in Apc$^{-/-}$ hepatocytes. (a) β-catenin, (b) destruction complex and (c) pErk as a function of the *Wnt* and *GF* concentration in the range $[0:1]$ following the normalization of our collaborators on the EU-project CancerSys. Note that the β-catenin concentration is a constant.

β-Catenin, destruction complex and pErk are shown in figure 3.13.

3.2.3 Simple models of coupling of proliferation and apoptosis to β-catenin and pErk

Different possible hypotheses may be supported by references and the findings in our consortium of how β-catenin and pErk concentration on one hand as well as proliferation and apoptosis on the other hand may be coupled.

Probability – triggered cell entrance or apoptosis

1. In a first approach we assumed that pErk and β-catenin determine the probability of proliferation and survival by a Hill function. This corresponds to assuming a threshold-

behavior. We assume that at a certain point in time a cell either enters the cell cycle, becomes apoptotic or stays quiescent depending on its concentration of β-catenin and pErk. One way of defining the probability to enter the cell cycle is:

$$p = \frac{1}{C}\frac{([\beta cat][pErk])^n}{\theta_p^n + ([\beta cat][pErk])^n} \tag{3.22}$$

n is the Hill exponent, $\theta_p > 0$ denotes the value where the 2nd derivative of p with respect to $[\beta cat][pErk]$ is zero. $C > 0$ is a normalization parameter. $0 \leq p \leq \frac{1}{C}$. The apoptosis probability can be defined as:

$$a = \frac{1}{C}\left[1 - \frac{[pErk]^n}{\theta_a^n + [pErk]^n}\right] = \frac{1}{C}\frac{\theta_a^n}{\theta_a^n + [pErk]^n} \tag{3.23}$$

Where $\theta_a^n > 0$ and $0 \leq a \leq \frac{1}{C}$. One can show that for any $n > 0$ and $\theta_p = \theta_a = \theta > 0$, we have $0 \leq p + a \leq \frac{2}{C}$. As the sum of the probabilities must be 1, $C \geq 2$.

The probability of a cell to stay quiescent is then:

$$q = 1 - p - a \tag{3.24}$$

Figure 3.14 shows p, q and a for C=3 for healthy and APC-ko cells for the values of figures 3.12 and 3.13. Note that if [GF]=0, then Erk is not activated and proliferation does not occur while apoptosis is maximal.

2. A second model would be that only activation of Erk alone controls proliferation and apoptosis. The effect of β-catenin on proliferation in this model is indirect: β-catenin enters the nucleus and triggers expression of TGF-alpha, which is secreted into the extracellular space. Here, it binds to the EGF-receptor and activates the Ras pathway activating Erk and triggering proliferation. For the cell cycle entrance probability one can assume:

$$p = \frac{1}{C}\frac{[pErk]^n}{\theta_p^n + [pErk]^n} \tag{3.25}$$

For the apoptosis probability:

$$a = \frac{1}{C}\left[1 - \frac{[pErk]^n}{\theta_a^n + [pErk]^n}\right] = \frac{1}{C}\frac{\theta_a^n}{\theta_a^n + [pErk]^n} \tag{3.26}$$

For the quiescence probability:

$$q = 1 - p - a \tag{3.27}$$

Figure 3.15 shows p and a for C = 2

State transition rates

One might expect that cells regularly sense the signals from their environment and readapt their state and activity to the incoming signals. In such a case one would have to

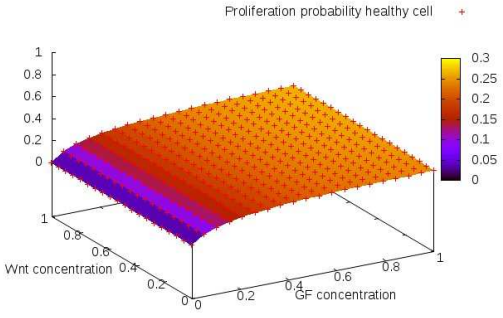

(a)

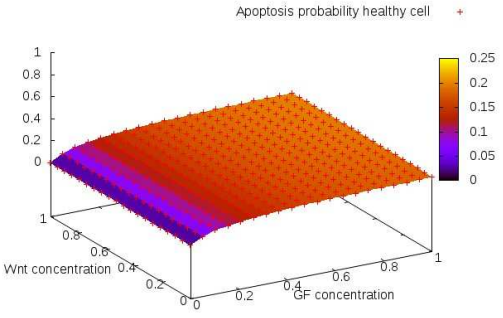

(b)

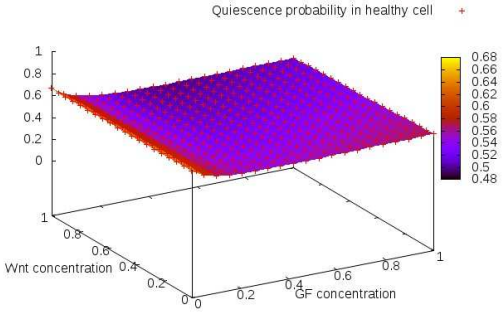

(c)

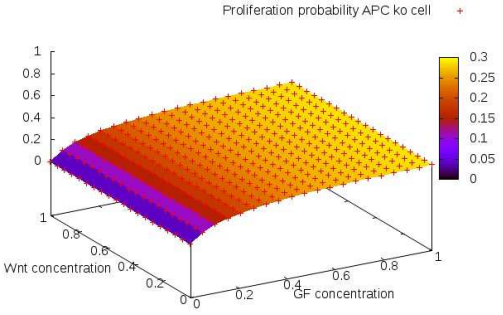

(d)

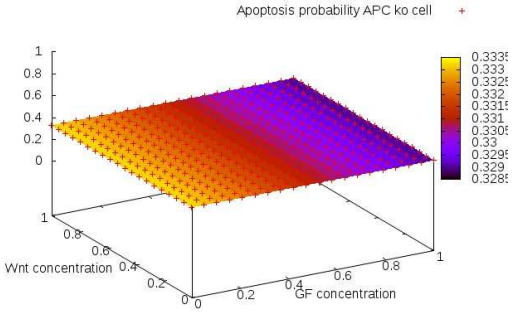

(e)

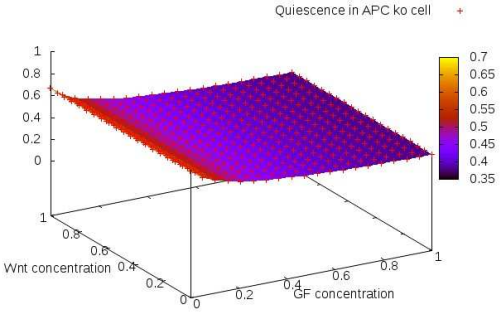

(f)

Figure 3.14: Probability model assumption 1 for equations (3.22) and (3.23): (a) Proliferation, (b) quiescence, (c) apoptosis probability for healthy cells, and (d) proliferation, (e) quiescence and (f) apoptosis probability for APC-knockout cells for the values used in figures 3.12 and 3.13.

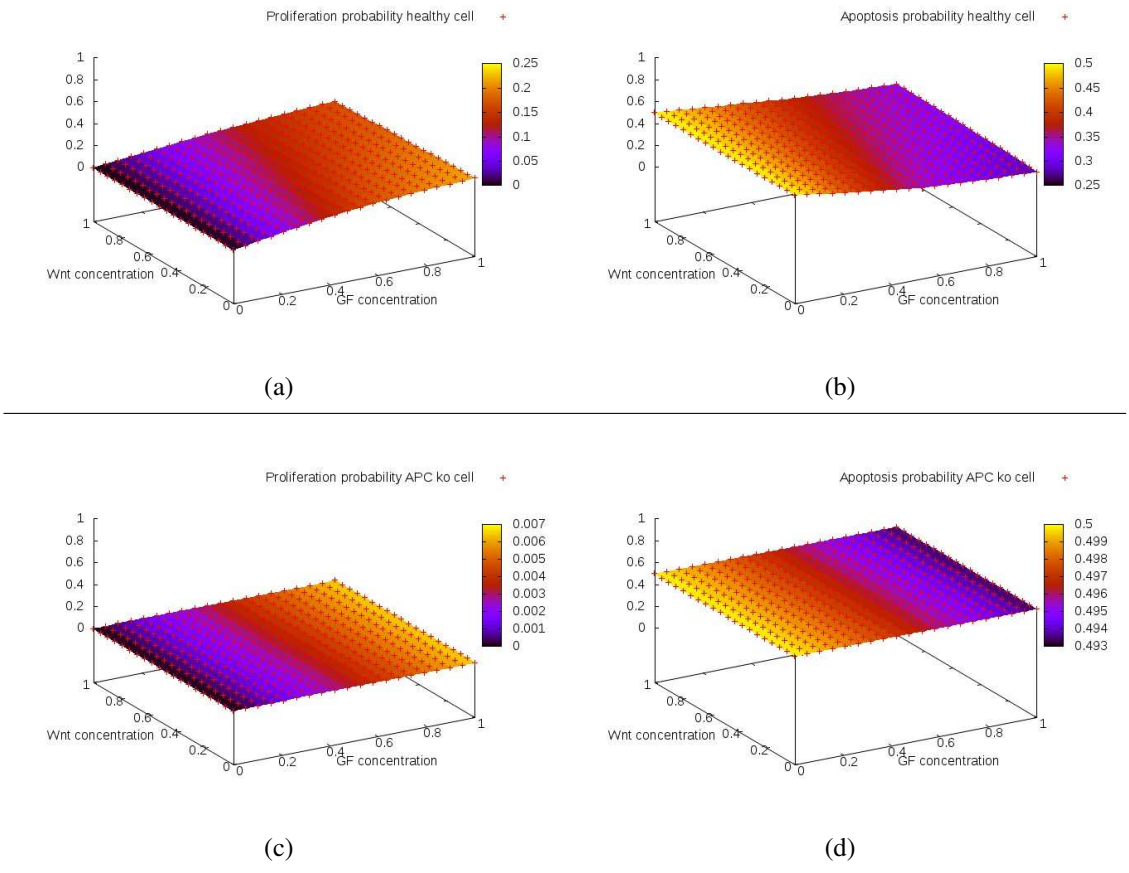

Figure 3.15: Probability model assumption 2 for equations (3.25) and (3.26): (a) Proliferation and (b) apoptosis probability for healthy cells, and (c) proliferation and (d) apoptosis probability for APC-knockout cells. In both cases, the quiescent probability is $q = 0.5$. The parameter values are those used in figures 3.12 and 3.13.

replace the probabilities by rates, one for certain rate of cell cycle entrance, another rate for cell death, and a third rate for quiescence (neither cell cycle entrance nor cell death). Cell death could only act on non-proliferating cells.

In order to mimic the experimentally observed bell-shaped curve of a cell cycle duration (see [23] and refs. therein) the cell cycle is divided into m sub-phases and Poisson processes are assumed to mimic the transition from one intermediate state to the next one. The cell cycle progression rate from one state $i > i+1$ can be defined by λ/m where relates $\lambda = 1/\tau$ to the cell cycle duration τ of an isolated cell. A cell at state m divides into two quiescent cells. A quiescent cell does not enter the cell cycle with rate α. Be further the death rate for a quiescent cell γ assuming that a proliferating cell does not die i.e., a cell, once it entered the cell cycle, finishes the cell cycle. In most cases and in absence of anti-mitotic drugs this gives a suitable description.

In the computer simulation the dependency of the rates on the local concentrations of Wnt and GF (including TGF-alpha) favors algorithms with fixed time step Δt. At time t, one would firstly test if the cell is proliferating or quiescent. Δt it has to be chosen small enough such that within the time interval only a single event is likely to occur in the whole population. Alternatively, one could chose cells in random order and make sure that each individual cell $i(i = 1,\ldots,N)$ can change its state only with $W_i\Delta t << 1$ where W_i denotes the total rate with which the state of the respective cell i can be left. However, this has the risk that one cell state change affects another one in the same time interval so usually it is favorable to choose Δt so small that $W_{total}\Delta t << 1$ where W_{total} is the total rate at which a given global state can be left. If for a random number η uniformly chosen in $[0,1)$, $\eta < W_{total}\Delta t$, then the configuration changes its state, otherwise no change of the global change is performed. To choose a state change, all states accessible from the current configuration are calculated together with its weight. Then one of them is chosen at random taking the weight into account. As the time interval has to be chosen very small, $\Delta t << 1/W_{total}^{max}$. Typically, $\Delta t << \eta/W_{total}^{max}$ with $\eta = 0.001 - 0.01$. Accordingly, the simulations can take very long.

For the simulations in this thesis we use the first approach (approach 1.) to show proof of concept as the last algorithm has very long simulation times.

3.2.4 Normal hepatocytes

For the simulations in this and the following sections the intracellular Wnt- and Ras-pathways were integrated into each individual cell. Wnt and GF are assumed to be transported outside the cell. The transport considered here is by diffusion from cell-to-cell. However, as long as no significant apoptosis occurs leading to large necrotic lesions no significant difference of cell-to-cell diffusion from inter-cellular diffusion in the ECM is expected. In order to be consistent with the normalization of our collaborators on the EU-project CancerSys, the GF-concentration is set to 1 in the outer field of the monolayer mimicking the peri-portal field, and Wnt is set to 1 at the center of the monolayer, reflecting the central vein. Advection is not considered. In this way the monolayer simulation represents a potential experimental setting. However, we also do not expect largely dif-

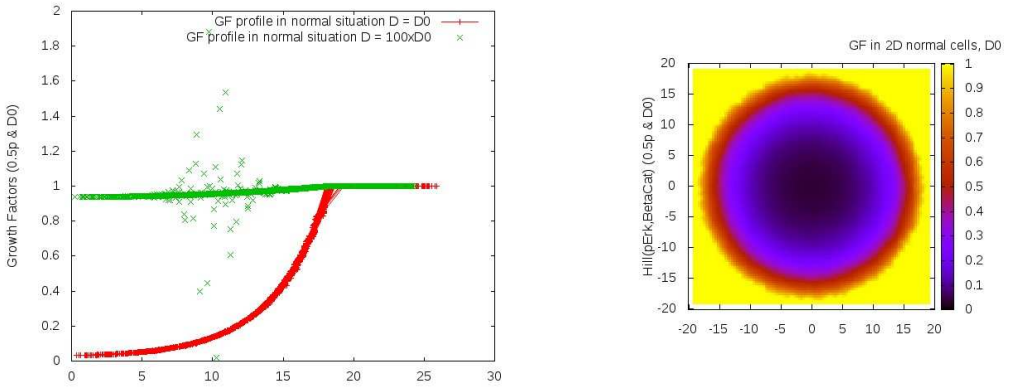

(a) (b)

Figure 3.16: (a) GF concentration profiles for 2 different diffusion constants as a function of the distance between the monolayer center (0) and the monolayer border (at 20 cell diameters). The noisy points emerge from the random position of cells as diffusion in the simulations was assumed to occur from cell-to-cell. (b) the GF profile in the monolayer in 2D for the smallest diffusion constant D_0. The value 1 represents the source at the border.

ferent results with or without advection as the size of the diffusion constant can largely account for the effect of advection.

Numerical solution of partial differential equations

We assumed that diffusion of Wnt and GF occurs from cell to cell. The numerical solution of the reaction diffusion equations for Wnt and GF for a given cell i during the time step Δt having a concentration equal to C_x with $x \in$ (GF,Wnt) follows the numerical scheme presented in 1.1.2.

Results

Figure 3.16 shows simulations results for the spatial steady state profile of GF in healthy cells for two different GF-diffusion constants. The noise reflects neighbor irregularities, as diffusion is from cell-to-cell. Intercellular diffusion in the ECM would damp noise effects if the local concentrations of GF are sufficiently large.

As expected, a smaller diffusion constant results in a steeper concentration profile. Figure 3.17 and 3.18 shows the corresponding spatial profiles of β-catenin, pErk, the product $[\beta cat][pErk]$ as well as the Hill function determining the proliferation probability.

Note that due to the product of β-catenin and pErk concentration, the slope for a small diffusion constant has another sign as that for a large diffusion constant. Hence, the spatial coupling by diffusion has a significant impact on the proliferation.

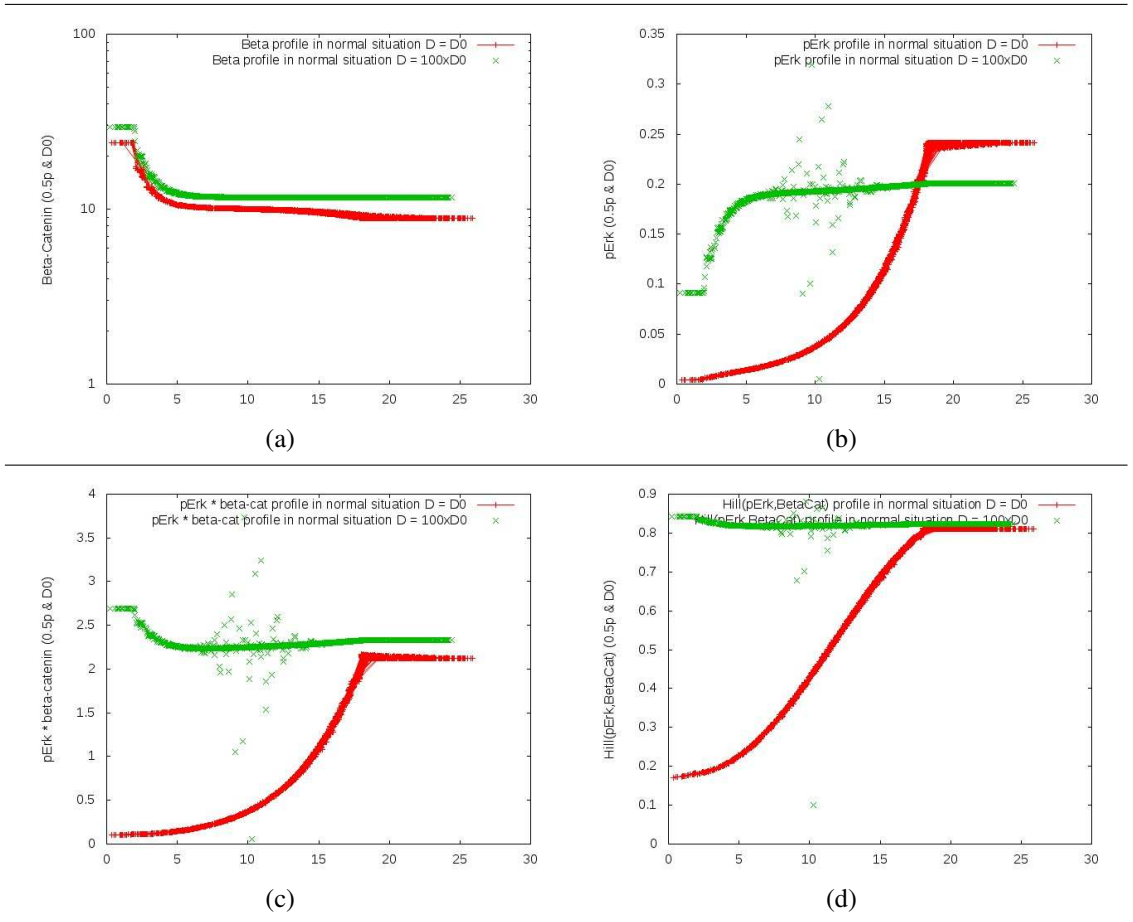

Figure 3.17: (a) β-Catenin concentration (in log-plot) vs. distance between monolayer border and monolayer center for two different diffusion constants. (b) corresponding plot for pERK concentration. (c) product of β-Catenin and pERK concentration, (d) Hill-function. Note that the gradient of the Hill-function changes sign in going from small to large diffusion constants.

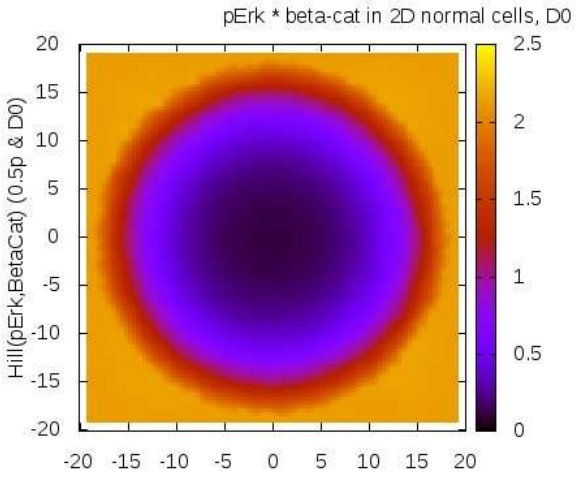

Figure 3.18: For small diffusion constant the Hill function has its smallest value in the center (lower), for large diffusion constant at the border (compare curves in middle line). Note that the local value of the Hill-function evaluated at the position of a cell determines the probability of cell cycle entrance of that cell.

3.2.5 APC depleted hepatocytes

We assumed that the depletion of APC does not modify the diffusion constant of GF or Wnt. For example, a high β-catenin concentration emerging from APC knockout could modify adhesion among cells and thus create disruption in the normal diffusion process. We assume that the diffusion of growth factors necessities to be faster enough to avoid this situation (order of few seconds which is much faster than cell properties modifications).

If β-catenin exceeds certain threshold of β-catenin ($\beta cat > \beta cat_{threshold}$) then $k_4 = 0$ and we find for the GF:

$$\frac{d[GS]}{dt} = -k_{12}[\beta cat] - k_{15}[GS] \tag{3.28}$$

If β-catenin does not exceed the threshold, then:

$$[GS] = 0 \tag{3.29}$$

TGF-α

Once β-catenin is over expressed and translocated into the nucleus it activates it serves as a transcription factor for genes of several factors, for example, GS, TGF-α and Dkk. TGF-α is secreted into the extracellular space where it can diffuse and bind to the EGF –

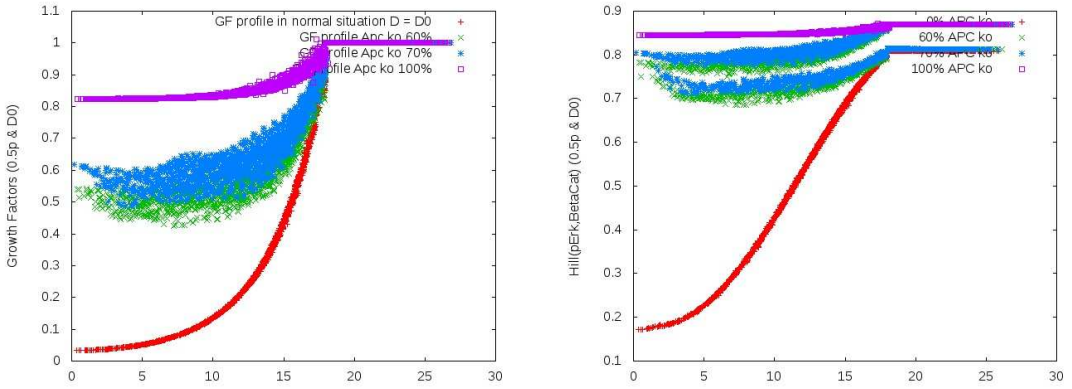

(a) (b)

Figure 3.19: (a) GF profile for 4 cases: no APC ko cells, 60% APC ko cells, 70% APC ko cells and 100%. (b) Corresponding Hill-function. For 0% APC-ko cells no TGF-α is produced (red curve) while for 100% APC-ko cells, each cell produces growth factor (magenta curve). For 60% and 70%, 2 different curves emerge, one that corresponds to APC ko cells, the other one for those cells where APC is not knocked out. (0.5p is the production term of TGF from APC ko cells, $p = 10^6$ in (seconds $\times$ cell volume)$^{-1}$)

receptor of the secreting cell and of neighboring cells and activate the Ras – pathway. For the secretion we assume: $TGF_\alpha = \varepsilon[\beta cat]$ with ε being a certain fraction in steady state.

If the cell is APC-KO, then $k_4 = 0$. The steady states for the destruction complex and β-catenin in case of APC-KO are respectively:

$$[DC] = 0 \tag{3.30}$$

$$[\beta cat] = \frac{k_6}{k_7} \tag{3.31}$$

In our simulations, we subsume TGF_α into the total GF-concentration by the replacement $[GF] \to [GF] + [TGF_\alpha]$. Hence, we assume that TGF-α has the same diffusion constant and decay rate at other GFs.

Results

The corresponding profiles found in the monolayer for *Apc Knock-out* are shown in figure 3.19. For 0% as well as for 100% knockout-cells the Hill-function generates a unique curve. For 60% and 70% APC-knock-out the cells with APC-knockout produce TGF-α and locally trigger β-catenin increase and, after secretion into extracellular space, an increase of GF in extracellular space, and by binding to EGF-receptor, an activation of RAS. For APC-knockout cells the Hill-function is larger than for those without APC-knockout for the parameters considered. In this case it is impossible to find a threshold such that proliferation occurs if 70% of the cells are APC knocked out but no or almost no

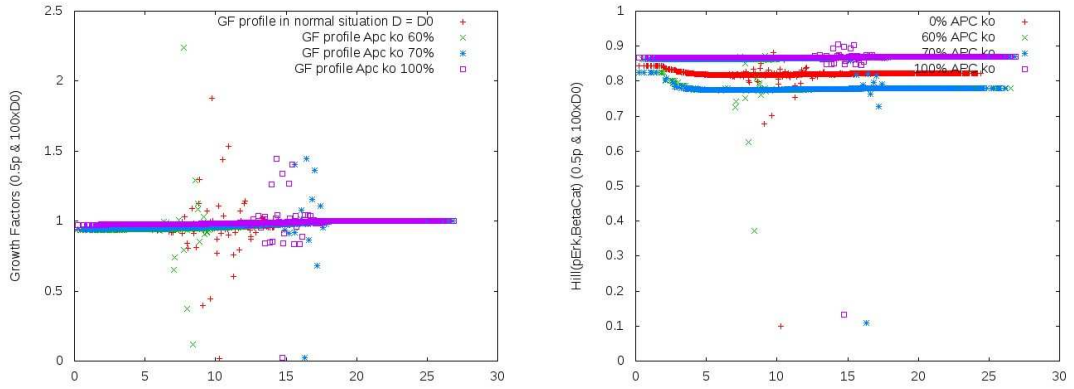

(a) (b)

Figure 3.20: Same simulation as for figure 3.19 but with 100 times larger diffusion constant. (a) GF concentration and (b) Hill-function for *Apc Knock-out* cells have approximately the same value of β-catenin and pErk. To distinguish them we had to increase the production of TGF (see figure 3.21).

proliferation occurs in case 60% of the cells are APC knocked out. Moreover the diffusion of GF is slow such that cells in APC-knockout – rich cell patches accumulate GF so the 60% and 70% APC-ko - curves show a large overlap.

Only increasing the diffusion constant of the growth factor did not help (figure 3.20). Still 60% and 70% could not be distinguished.

Only after in addition to the increase of the GF-diffusion constant also the production rate of growth factor was increased it was possible to define a threshold capable of distinguishing between 60% and 70% APC-knockout cells.

Figure 3.23 shows simulations where in the monolayer the cell cycle entrance after administration of tamoxifen is mimicked for a cell layer without *Apc Knock-out* , Figure 3.24 the corresponding pictures with *Apc Knock-out* . The parameters are the same as for figure 3.21.

Coupling to cellular phenotype

In figure 3.25, we investigate which cells enter the cell cycle at 50% and 70% APC-knockout hepatocytes, respectively. At 50% almost no cell cycle entrance is observed in the model. The remaining very small number of cell cycle entrance may disappear once we also include free diffusion in intercellular space while so far we have only considered cell-to-cell diffusion. For 70% APC-knock out a significant fraction of cells enters the cell cycle.

It turned out that the dynamics is very important. We first calculated the proliferation profile starting from the steady state of the β-catenin concentration which led to results incompatible with the experimental findings. In this case, all cells entered the cell cycle. Moreover, if the GF were not removed fast enough from the environment it may

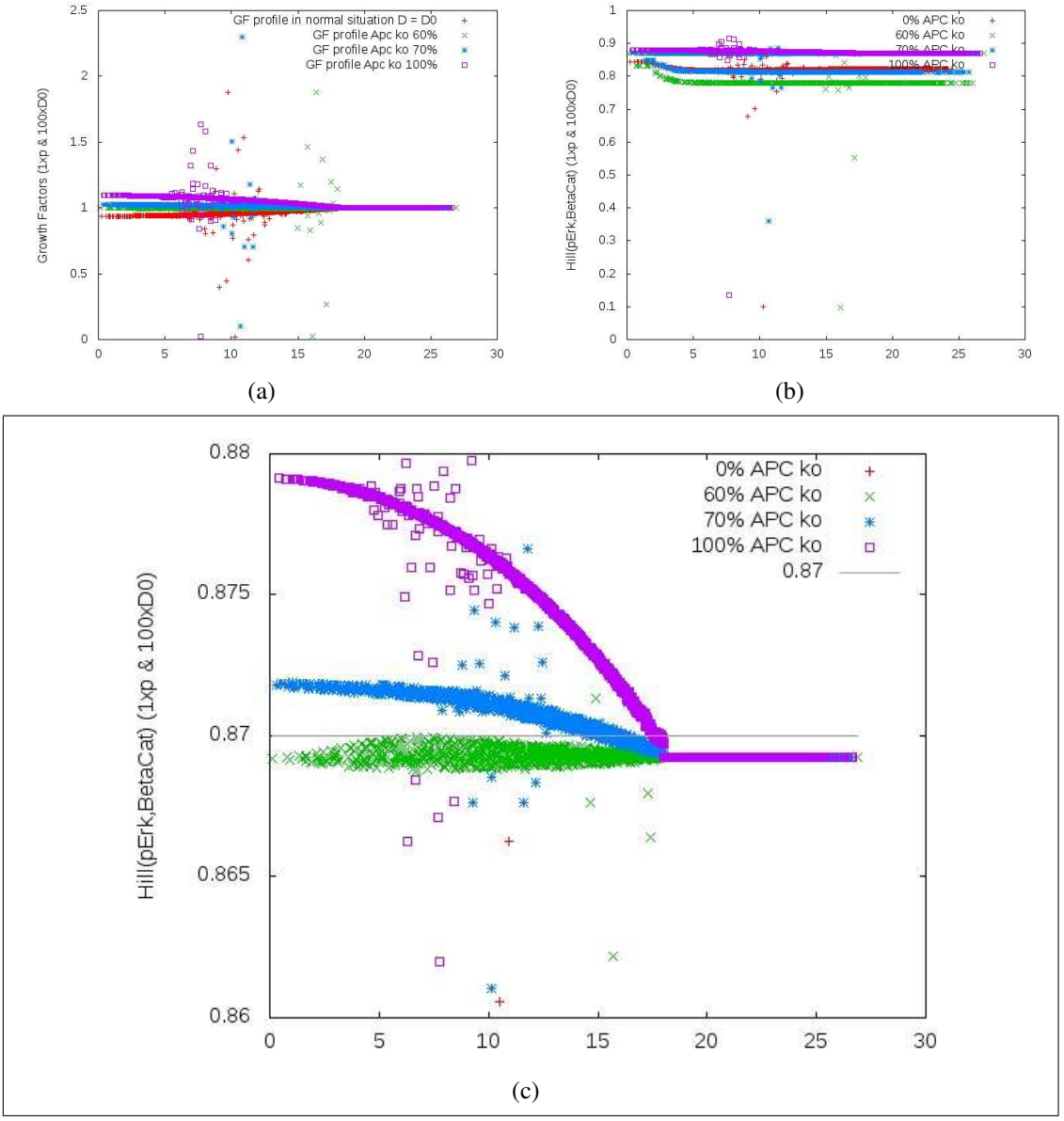

Figure 3.21: (a) Growth factor and (b) Hill-function if in addition to the increase of the diffusion constant (see figure 3.20) also the production rate of TGF-alpha was increased. (c) Magnification of the upper right picture. Due to the fast diffusion, GF is homogeneously distributed and due to the large production rate of TGF-alpha, a distinction between 60% case and 70% case by a threshold becomes feasible.

Figure 3.22: Legend color for probabilities: from 0 (black) to 1 (white).

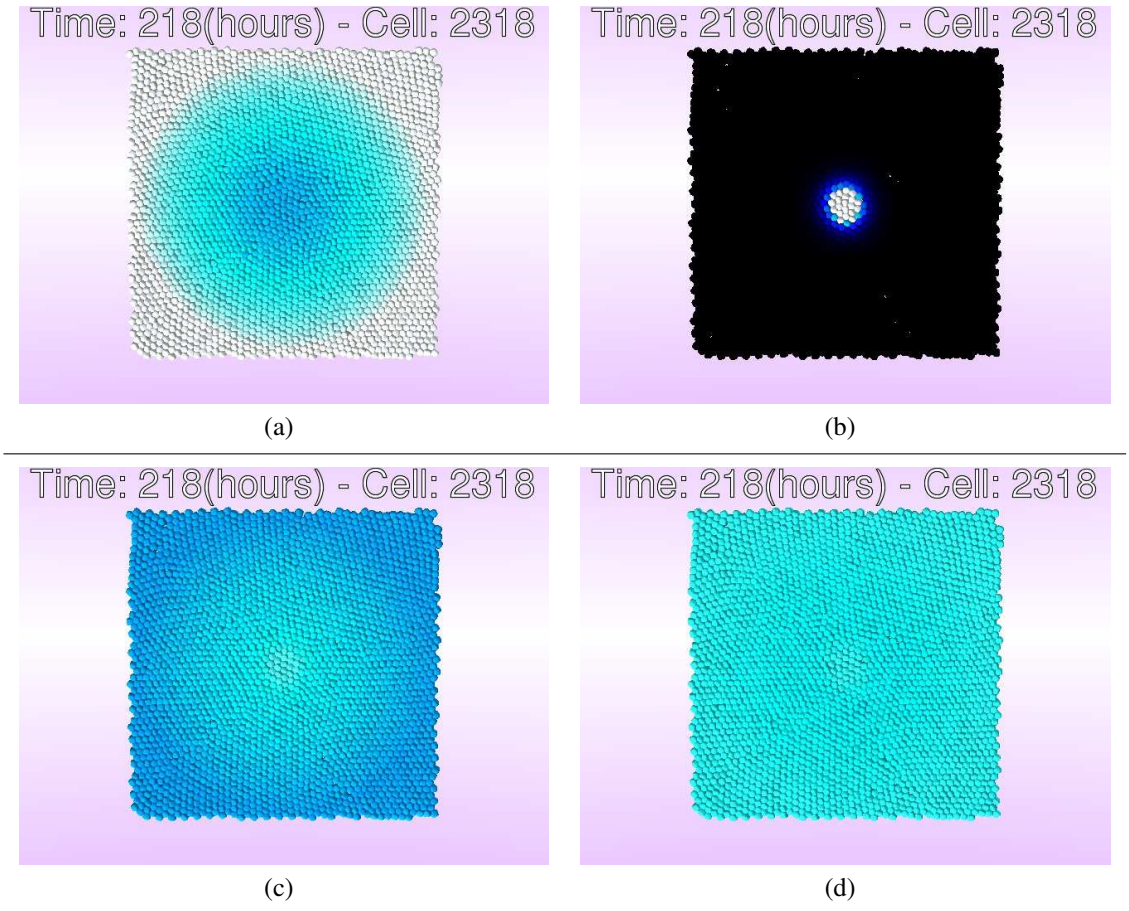

Figure 3.23: Simulations: for cells without APC knockout. Computation of concentrations and pathways for normal cells in a monolayer with a ring of sources of GF at the border and Wnt in the center. (a) GF diffusion is fast enough to generate a moderately increasing gradient of GF concentration from the border. (b) Wnt sources trigger β-catenin only for the cells close to the center. (c) The probability of apoptosis is higher in the center while (b) the probability of proliferation is very homogeneous.

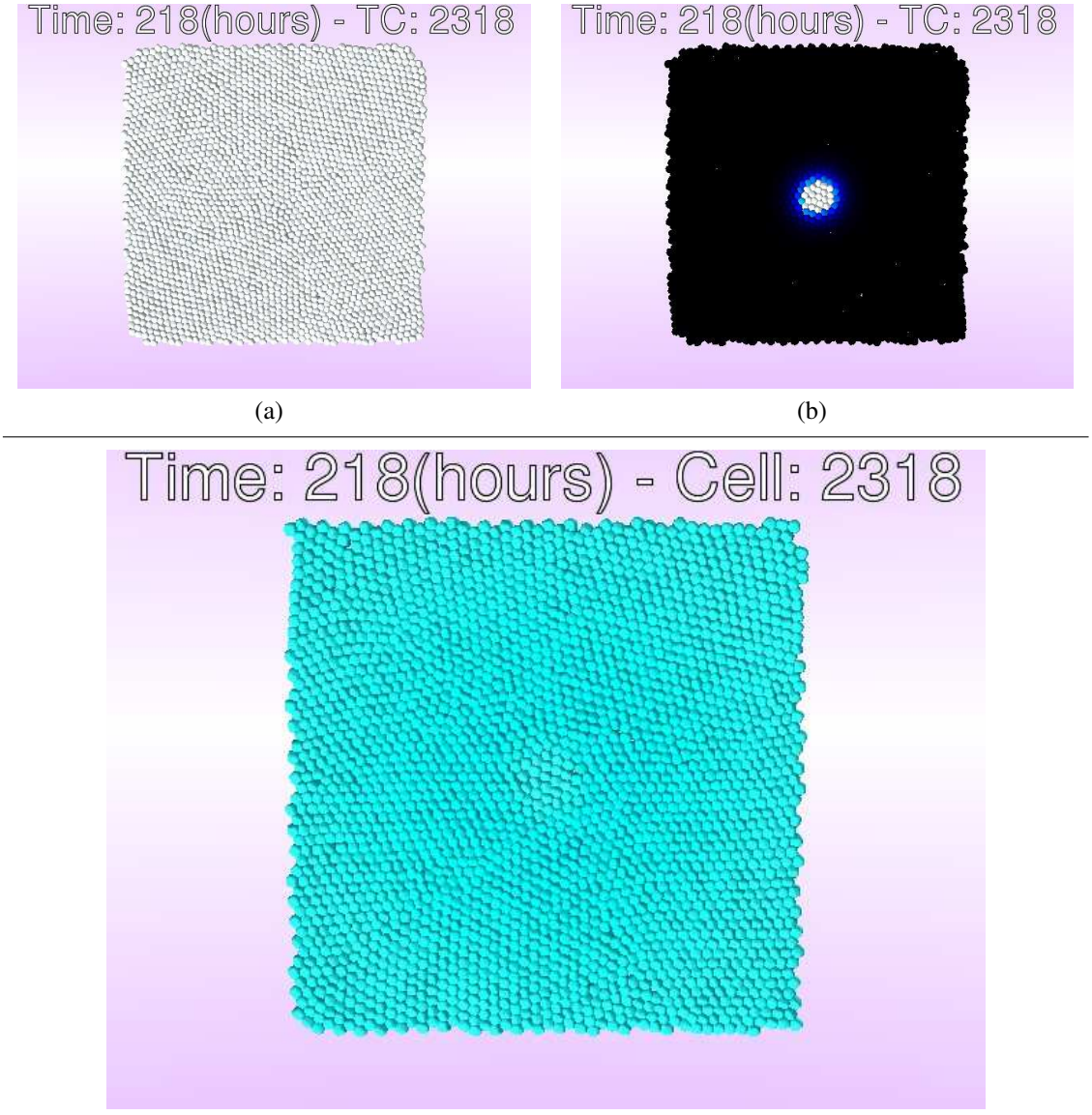

Figure 3.24: Same simulations as for cells without APC knockout (see figure 3.23) here for APC knockout cells. (a) GF diffusion is fast and the high number of sources fills the domain. (b) Wnt sources provide only the cells close to the center with Wnt. (c) The probability of proliferation is 1 in the tumor center (light blue are cell sources not taken into account for the computation of the pathways). APC ko cells do not show dependence on the Wnt concentration. Every APC-knockout cell has a high probability to enter the cell cycle as the GF concentration is high enough.

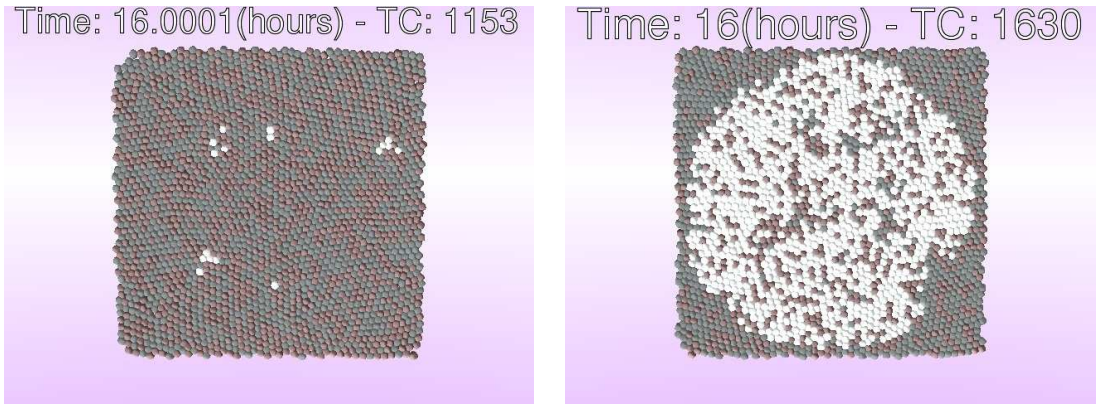

(a) (b)

Figure 3.25: Simulation of cell cycle entrance with (a) 50% APC ko cells and (b) 70% APC ko cells. Brown cells are without APC-knockout, gray cells are quiescent APC ko cells, white cells are proliferating APC ko cells. The threshold is reached for almost all APC ko cells in the 70% case in only 16 hours.

accumulate and induce proliferation.

In figure 3.25, we mimicked the full dynamics from the moment on the cells became $Apc^{-/-}$.

3.2.6 Outlook

The procedure outlined above opens the option to study molecular effects in multi-cellular organ environments. We have demonstrated this here for monolayers choosing the boundary conditions such that they reflect a liver lobule. However, as we used the same software as for tumor genesis in multi-lobules, we are currently running the simulation in full organ environment.

The results show that considering the spatial arrangement of cells instead of only individual cells can make a big difference. Moreover, information from higher scales can help to identify missing control units or links on the intracellular molecular scale.

Both steps studying the impact of cell-level parameters on the tumor phenotype and integrating the intracellular molecular model into each individual cell need to be performed separately. The reason is that not all influences of the intracellular activation patterns on the cell-level parameters are known, so an integrated multi-scale model representing the Wnt/Ras-modules within each cell and coupling them to the known cell parameters proliferation and apoptosis may be insufficient to explain the experimentally observed growth pattern. Indeed, proliferation and apoptosis alone seem insufficient to explain the occurrence and the pattern of the well differentiated and poorly differentiated tumor phenotypes. As suggested in later section, interactions between sinusoidal endothelial cells and tumor cells are likely to be crucial to understand emergence of well-and poorly differentiated tumor phenotypes. This could only be found from studying the effect of cell-level

parameters on the tumor phenotype independently of the intracellular molecular alphabet. On the other hand knowing the possible cell level parameters capable to explain the experimentally observed phenotypes gives valuable hints to additional functions of Wnt- or Ras- pathway activation effects, or to alternative pathways that may be activated during carcinogenesis.

3.3 Model prediction on vasculature in case of disordered division

In brief:
The liver functions are dependent on the liver tissue organization. In this tissue, the vasculature plays a crucial role. In this section, we show a sensitivity analysis of the model on the vessel stiffness and relate it to the well-differentiated phenotype.

3.3.1 Introduction

As emphasized in section 3.1.2, the liver functionality is totally dependent on its architecture. It has been observed in section 3.1.3 that poorly and well-differentiated tumors create disorder in the tissue organization. For poorly differentiated tumors, the sinusoids are simply removed from the tumor center (see explanation in section 3.4) whereas in well-differentiated tumor, vasculature remains in the tumor but is slightly disordered. In figure 3.26, we can see a magnification of a well-differentiated tumor. The co-staining of sinusoid in red and the hepatocyte membrane in green produces a yellow-like color in the healthy tissue whereas they are clearly separated in the tumor nodule.

In case of rapid cell proliferation, additionally to the force already present (cell/cell adhesion, cell/cell repulsion, cell/SEC adhesion, cell/SEC repulsion), the cell growth exerts a force that distorts the surrounding vasculature. The response of the vasculature is proportional to the Young modulus of the endothelial cells it is composed of. This feedback effect determines the pattern of the vasculature. We make a sensitivity analysis of this parameter and demonstrate its importance in resulting tumor phenotype. We compare different scenarios using a value found in the literature for *in vivo* liver sinusoids [9].

3.3.2 Vessel stiffness

In tumor, mechanical properties changes could be either the result of cell phenotype modification or, inversely, a factor that induces cancer [51]. In both cases, a better understanding of the interplay between the tumor phenotype and the biomechanical properties of the tissue constituents cells and vessels may on the long run permit a better diagnosis. Hepatocytes are differentiated cells. Their main function is linked to blood exchange (metabolic functions, detoxification, etc.) and their spatial arrangement. Within the model

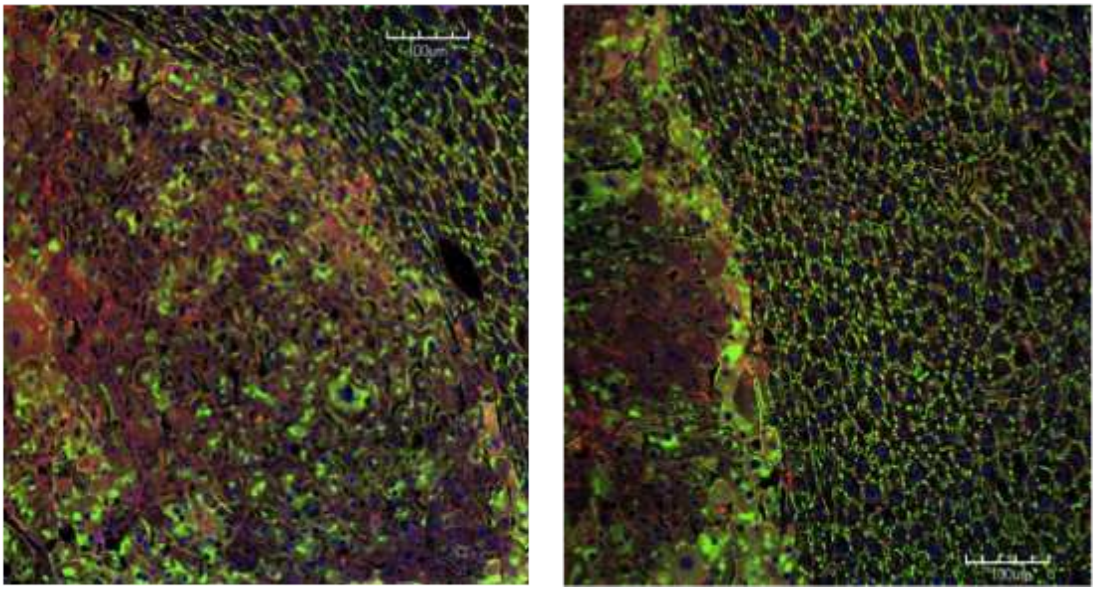

(a) Magnification of figure 3.6 (b) Magnification of figure 3.6

Figure 3.26: Well-differentiated tumor magnifications of figure 3.6. Magnification of a well-differentiated tumor at the tumor border. All markers appear in healthy and tumor tissue but the tumor tissue is clearly disordered.

we represented hepatocyte properties that we believe influence the spatial arrangement of hepatocytes and tumor cells in the lobule and consequently their contact with the blood. Cells (hepatocyte or tumor cell) have mechanical capabilities in relation with blood cells that we consider: polarity (an asymmetric shape that is orientated for communication and exchange), morphogen attraction by SEC, HSA, cell/SEC adhesion as properties which inherently require a sinusoid in the spatial neighborhood of a cell; without the presence of the sinusoid, such cell properties cannot persist. We study the case of vasculature destruction in section 3.4 that provides a possible explanation for the emergence of a poorly differentiated tumor. For well-differentiated tumors, the vasculature remains in the tumors but is disordered (see figure 3.26). To better understand this phenomenon, we tested the influence of the vessel stiffness on the tumor phenotype.

We considered a wide range vessel stiffness: Young moduli of 20 Pa, 1000 Pa, and infinitely stiff vessels (see formula that relates the Young modulus and stiffness in section 1.1.2). At Young moduli above 100 Pa, the forces between blood vessels and cells can become very large so that the time step in the simulation has to be chosen extremely small to avoid numerical artifacts. It leads to very long simulation time longing (up to a month in certain cases). We find, that the growth velocity of the tumor does not change significantly with the vessel stiffness (data not shown), while the phenotype shows significant changes. With increasing vessel stiffness more vessels remain within the tumor as this is observed in the well-differentiated tumor phenotype. On the other hand if the vessel stiffness is small, the expanding tumor is able to push the vessels aside so that inside the tumor almost no

vessel is found (see figure 3.27).

Tumor cells may secrete proteolytic enzymes that could weaken the vessels, which within the mathematical model corresponds to the case of soft vessels. In case of too soft vessels, the model predicts a vessel depletion within the tumor and high vessel density at the tumor border which is not observed (see schematic representation in figure 3.29). With very high stiffness (for numerical reason we approximated it as infinite and in these simulations vessels cannot move), the vasculature remains inside the tumor like in well-differentiated tumors. On the other hand, vessels seem not that stiff if we refer to experiments conducted on liver sinusoids in [9] that estimates the stiffness at 1000 Pascal. Moreover, if healthy hepatocytes would offer no resistance to tumor cells and die easily upon compression by tumor cells, then tumor cells would replace one by one the healthy hepatocytes. Like in case of liver regeneration, the order would be maintain at least as it is shown in [43], the surface contact fraction between cells and endothelial cells would recover a normal value and the total number of cells in the liver would approximately remain unchanged.

3.3.3 Results:

Soft vessels are pushed aside by tumor cells (figure 3.27(a)). For infinitely stiff vessels, the proliferation is not stopped by the rigidity of the vasculature. The compression of the tumor cells does not prevent proliferation (figure 3.27(b)). With 1000 Pa stiffness for the vessel, the result is an intermediate case which shows the continuity between very soft and very hard vasculature (figure 3.27(c)).

3.3.4 Discussion

Simulations demonstrate that the order in well-differentiated tumor is mainly controlled by the vasculature organization. Indeed, major hepatocyte mechanisms that organize the tissue like HSA, morphogen attraction, cell/SEC adhesion are dependent on the local vessel density. Thus, a large distortion of the vasculature that induces a vessel depleted tumor core would lead to a tumor phenotype very similar to poorly differentiated ones (except that the staining would be different and a high vessel density would remain at the border). With the value of 1000 Pa, we found in literature for sinusoids Young moduli, the vasculature is soft enough to be disorganized but depletion of tumor vessels does not occur. We could exclude that a slower tumor growth and/or a lower BFI threshold would produce well-differentiated tumor phenotype (results in Sections 3.6.2 and 3.6.8). With the biological information available – parameter values from literature, staining that suggests the presence of specific hepatocyte mechanisms – the model reproduces qualitatively well-differentiated tumor phenotypes. A quantification of the proliferation rates and the local vessel density would be sufficient to calibrate the model parameters to permit fitting of experimental data for well-differentiated tumors.

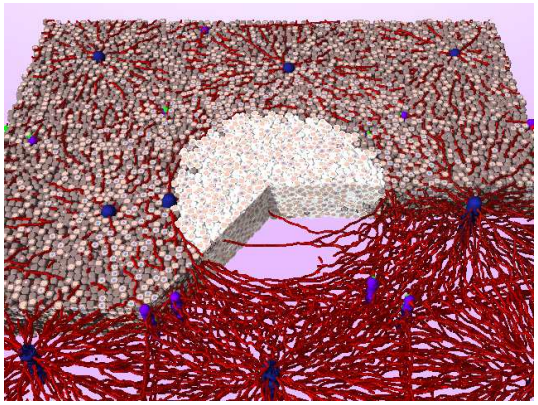

(a) Soft vessels

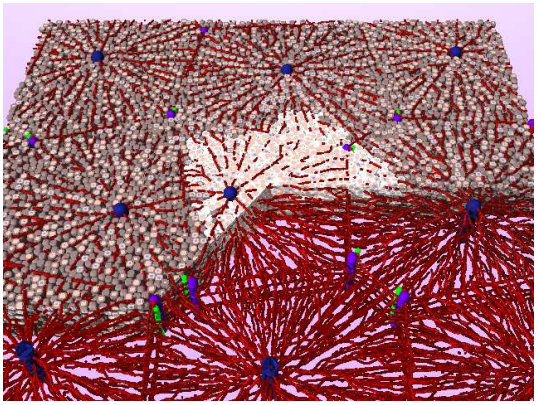

(b) Stiff vessels

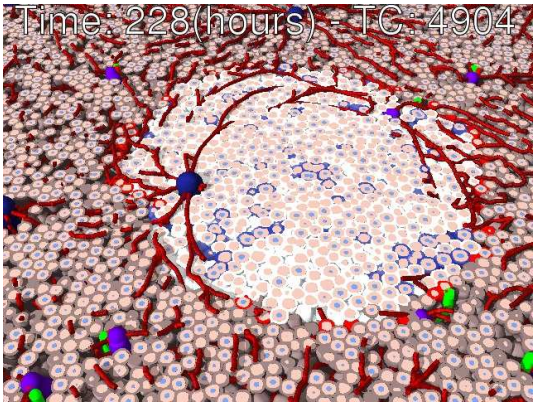

(c) Moderately stiff vessels

Figure 3.27: Vessel distortion: Results from tumor growth simulations: (a) the tumor weakens blood vessels which permits the tumor to push them aside. On the contrary, (b) the vessels are fixed and cannot be pushed by the tumor. (c) is an intermediate case (1000 Pascal).

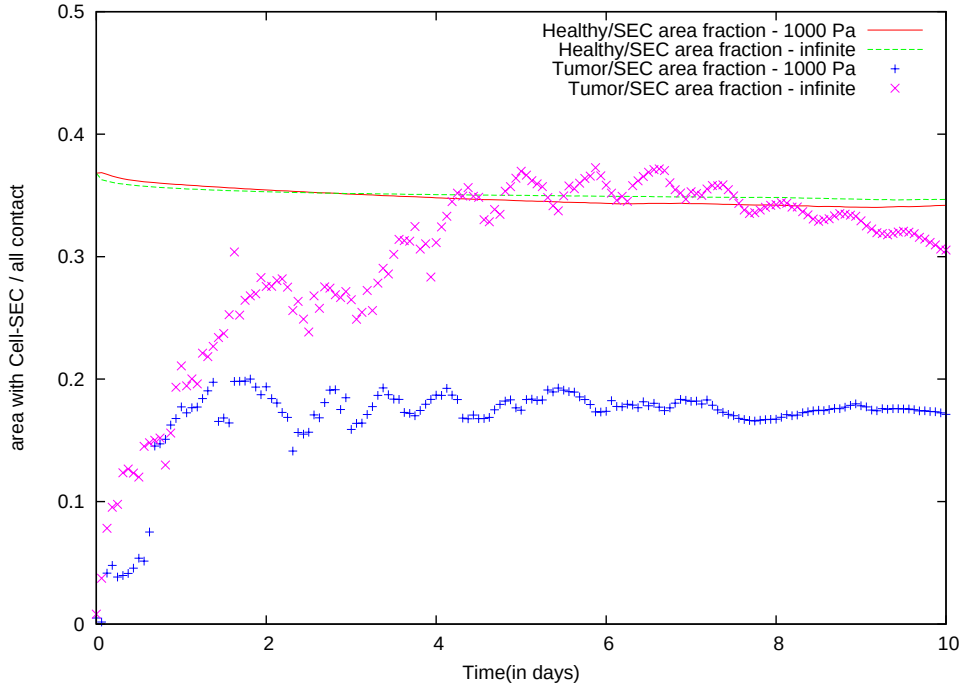

Figure 3.28: The disorder in the tumor can be seen from the contact-area fraction (see section 1.1.3). In simulation with infinitely stiff vessels, the tumor replaces the healthy hepatocyte without disturbing the vasculature. After passing an initial transient phase the contact area fractions Healthy/SEC and Tumor/SEC are in agreement. In the 1000 Pascal simulation, a significant fraction of vessels are pushed towards the border and the Tumor/SEC contact area fraction remains below the Healthy/SEC curve.

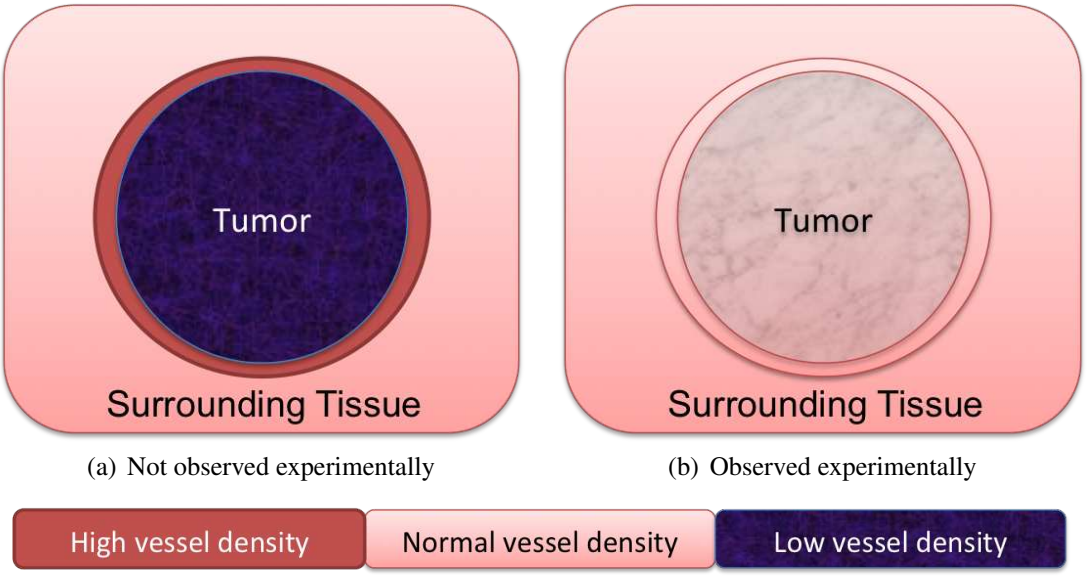

(a) Not observed experimentally (b) Observed experimentally

Figure 3.29: Schematic representation of the vessel density in simulations. The left scheme shows the simulated phenotype obtained with very soft vessels. On the other hand, the right scheme represents a well-differentiated tumor. Because the vasculature depends on the vessel stiffness, if the vessels are very stiff, the tumor remains vascularized but contrary to liver regeneration: the tissue is disordered.

Conclusion:
The homogeneity of the vessel network depends on the ratio among the vessel stiffness and the velocity and strength of the growth. With the experimental value of 1000 Pascal for the vessel stiffness, a totally uncontrolled proliferation creates vessel depletion within the tumor. To calibrate the model, one needs quantitative data on vessel architecture in well-differentiated tumors and data on the tumor development. The next section shows another sensitivity analysis that also emphasizes the determinant role of the vasculature.

3.4 Poorly differentiated tumor: a sufficient condition on cell phenotype

In brief:
In the mouse model, biologists observed poorly differentiated tumor after *APC* cell depletion. This tumor phenotype is characterized by the absence of blood vessels. We integrated this information by including destruction of vasculature by tumor cells and performed a sensitivity analysis.

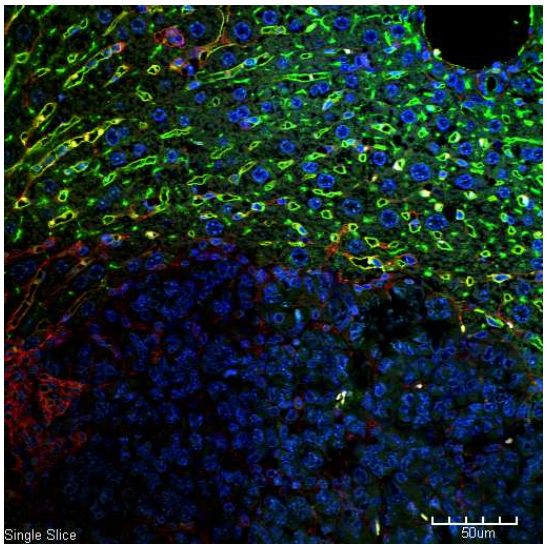

(a) Magnification of figure 3.7

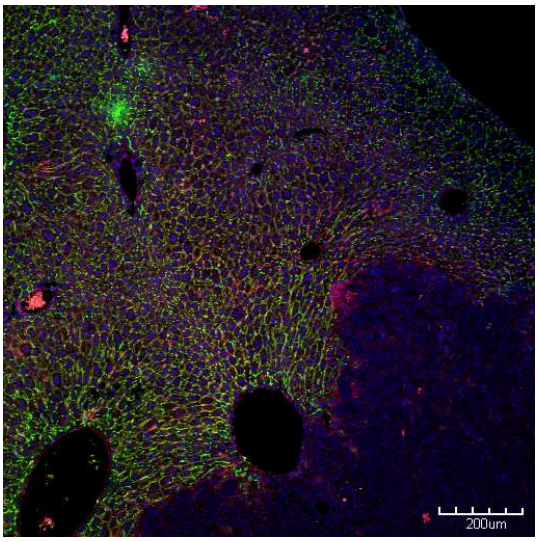

(b) Magnification of figure 3.7

Figure 3.30: Poorly differentiated tumor: this tumor phenotype lost specific hepatocyte functions like tight junction formation. It results in a disordered tissue that clearly identifies the tumor. At the tumor border, the red staining shows traces of SEC that gradually disappear in the tumor center.

3.4.1 Introduction

In section 3.2, we explain the plausible mechanisms that could trigger proliferation in *Apc Knock-out* cells. However, these mechanisms do not explain the cause of the different phenotypes. As outlined in previous section, Wnt and HGF (or other GF) stimulated activation of the down-stream pathways affect proliferation and apoptosis. Indeed, as explained in section 3.1.3, in the first experiments, once the proliferation is triggered, the mouse has very low chances to survive its hepatomegaly, which prevents observation of tumor formation. One way to investigate if activating β-Catenin signaling is an oncogenic event in the liver is to injecte lower dose of *AdCre*. Surprisingly the results show two distinct tumor phenotypes with the same experimental protocol. The poorly differentiated phenotype presents a major distinction: the absence of vascularization in the tumor (see figures 3.30(a) and 3.30(b)).

3.4.2 Vasculature destruction

As described in the section 3.1.3, experimentalists found two significantly different tumor phenotypes. The poorly differentiated phenotype (less frequent) is characterized by 2 aspects: there is almost no vascularization inside the tumor and tumor cell/normal cell adhesion is absent. The latter can is suggested by the lack of DPPIV staining: DPPIV stains bile canaliculi that are enclosed by tight junctions. Hence the absence of DPPIV directly demonstrates the lack of bile canaliculi. Thus, DPPIV is a signature of adhesion

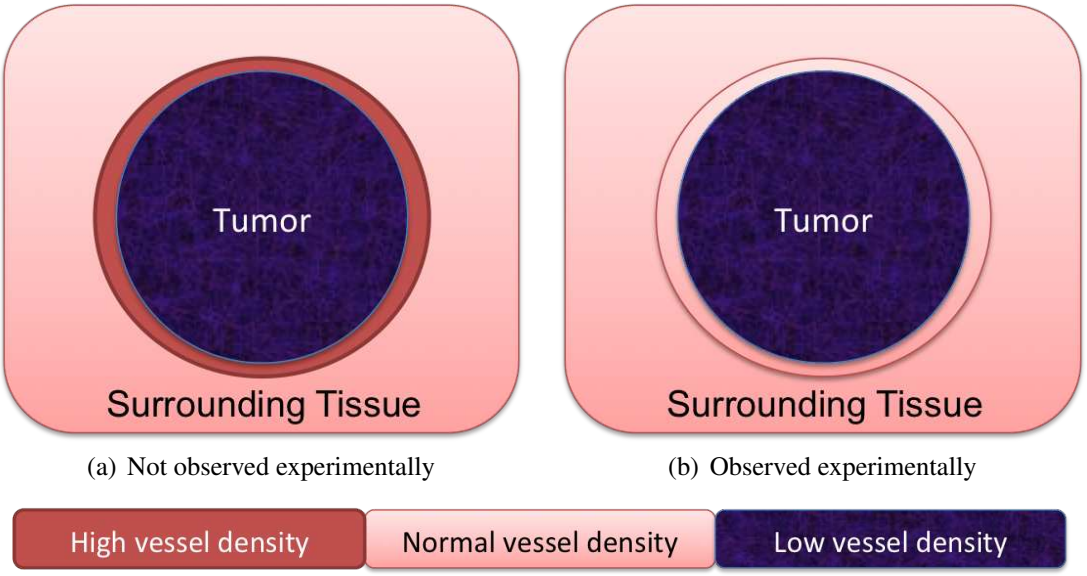

(a) Not observed experimentally (b) Observed experimentally

Figure 3.31: Vessel density in simulations. The left scheme illustrates the phenotype obtained when the vessels are very soft (compare also 3.3.2). The scheme on the right side can exclusively be obtained only if vessel destruction occurs.

among hepatocytes. For that reason, missing DPPIV in a tumor can be interpreted as a missing cohesion between tumor cells. However, a separate study on the effect of cohesion between tumor cells led us to the conclusion that the lack of adhesion between tumor cells alone is insufficient to explain the occurrence of a poorly differentiated tumor phenotype (section 3.6.3).

Our next hypothesis was induced by results in section 3.3.2: a softening of the vessels explain their depletion in the center of the tumor. Moreover, the tumor cell mass exerts a physical stress on the vessels and stretches them. This leads at least transiently to a significant increase of vessels at the tumor margin (scheme 3.31(a)). However, this hypothesis could not be confirmed by observations. In a next step we studied the case tumor cells could destroy blood vessels. Such destruction may result from the secretion of proteolytic enzymes or by compression of sinusoids such that blood cannot pass through anymore in which case the vessels eventually dissolve [31]. In this case we find the situation represented by the scheme Figure 3.32(b).

As an alternative mechanism to destruction by a short-range proteolytic enzyme, we considered the mechanism of blood vessel destruction by a mechanical pressure. This mechanism was able to qualitatively reproduce the observed experiments where the tumor is not vascularized and the vessel density at the border is normal. If the destruction mechanism is efficient enough – in figure 3.32, upper right image we assumed a pressure of 100 Pa to be sufficient for vessel destruction – then a poorly differentiated phenotype occurs. If it is not efficient enough – in the 2^{nd} line of Figure 3.32 we assumed the pressure necessary to destruct a vessel is 500 Pa – then some vessels still remain within the tumor and higher vessel density is observed at the border of the tumor. Thus, additional

information and tumor growth speed (permitting to infer the pressure exerted by the tumor), vessel destruction rate and vessel density (giving information on the death pressure threshold) would permit to calibrate the model to fit the biological data.

We added the possibility of the vasculature destruction for different tumor cell phenotype: TC/TC adhesion, HSA division, Cell/TC adhesion, etc. (results not shown). The results do not show significant differences and suggest that any aggressive tumor phenotype that could destroy its surrounding vasculature would produce the same outcome.

3.4.3 Discussion

The results of the simulation suggest that SEC death induced by pressure exerted from tumor cells on the blood vessels or a short range proteolytic enzyme secreted by tumor cells and acting on the blood vessels is a sufficient condition to explain the emergence of a poorly differentiated tumor phenotype. However, the molecular origin of such vasculature destruction is not known and may be diverse. The experimental data suggest that the vessel removal is necessary and the results of the simulation show that the vessel removal is a sufficient condition.

Conclusion:
APC depletion in cell has a strong oncogenic effect that affects many aspect of the cells. In particular APC depletion could be a possible cause for the emergence of aggressive tumors able to destroy the lobular vasculature. In this case, SEC death is sufficient to reproduce poorly differentiated tumor phenotypes, whatever are the other mechanisms and parameters of tumor phenotype as well as the molecular origin of the SEC death. In order to find the proper parameters tumor growth rate and destruction pressure threshold calibration of the model parameters with biological data that are not yet present would be necessary.

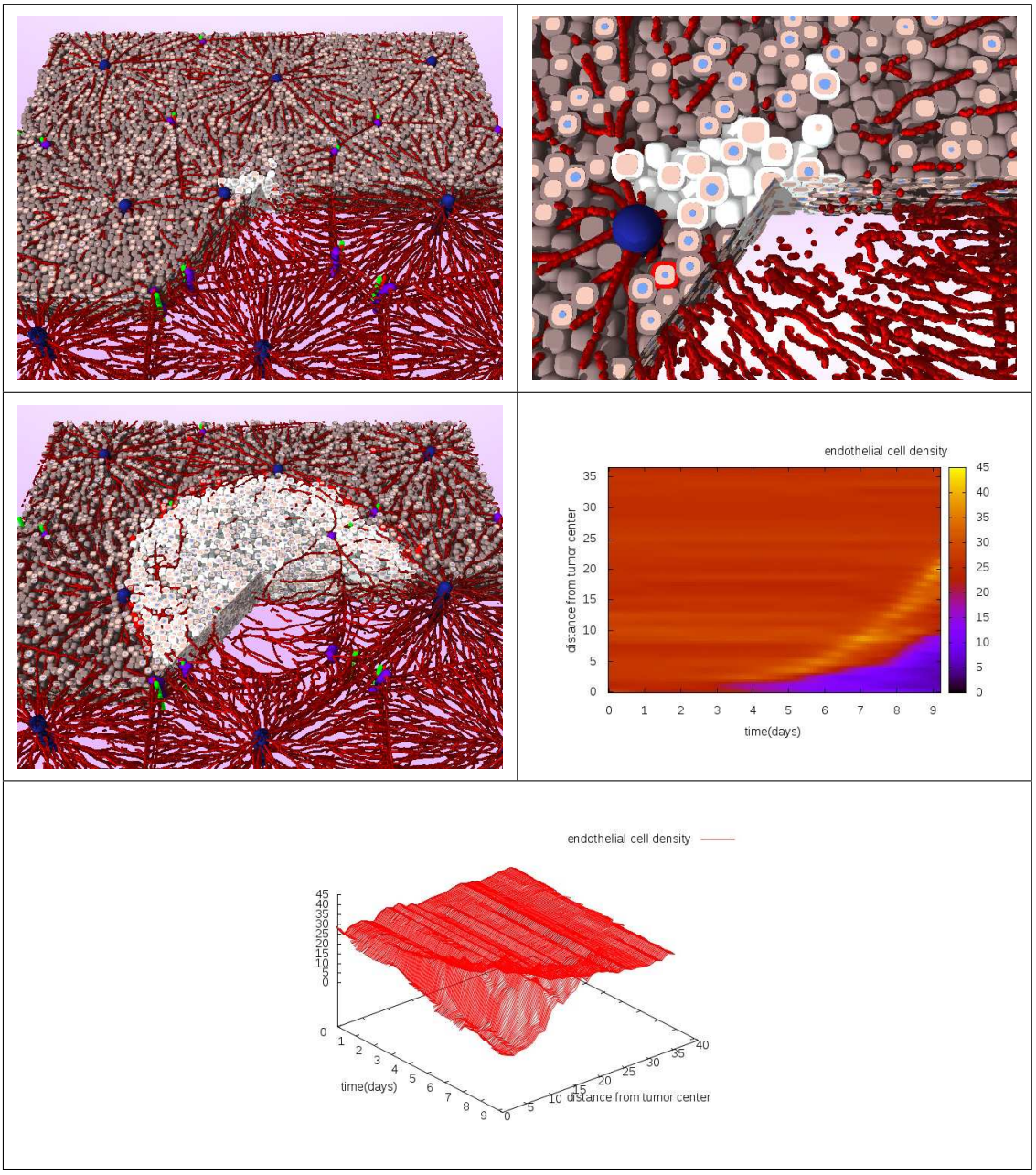

Figure 3.32: Snapshots from simulation where SEC are destructed and dissolved if proliferating tumor cells exert a pressure on them that exerts a certain threshold. For the simulations in this figure, the vessel stiffness is 3000 Pa. First line, on the left side, a simulation that reproduces the poorly differentiated phenotype. First line, right hand side: a magnification of the simulation image on the left hand side (the pressure threshold is 100 Pa). Second line: a simulation where the threshold for SEC removal is 500 Pa. The destruction is not fast enough compared to the tumor's growth so some vessels remain inside the tumor.

3.5 How symmetry reflects the tumor cell phenotype in early carcinogenesis

In brief:
In sections 3.4 and 3.3, we studied the emergence of different tumor phenotypes. We did not, however, study any mechanism affecting tumor symmetry, and how the tumor phenotype is expected to vary with tumor size beyond a nodule size. In the rat experimental model where tumors can be initiated in a controlled way, small tumors can be observed while in human patients at the time point of clinical manifestation, tumors are usually of centimeter size. The tumor shape at tumor initiation may reflect important information on the underlying mechanism. Hence it is important to know if effects that are detectible for small tumor nodules and reflect properties of the tumor cells, may still be reflected in the tumor shape or phenotype at tumor sizes exceeding the distance between the central and periportal vein.

3.5.1 Introduction

In the sections 3.4 and 3.3, all described tumors had a largely spherical symmetry that is in agreement with experimental data from 3.1.3. The mice were killed after 8 or 9 months and so the tumors obtained from this HCC model are large – they cover a volume larger than one lobule which involve at least several dozen of thousands cells. At this size, individual cell properties may be smoothed out. For instance, the HSA mechanism described in [43] would be negligible if the vasculature has disappeared. The same holds true for the tumor/healthy cell adhesion. More subtle underlying mechanisms could become invisible in large tumors where the disorder becomes dominant. In particular, we show in this section that it is the case for asymmetric growth in HCC. We study early patterns and memory effects and give an example for the transition from early to later stages of tumor growth. We qualitatively compare the results with experimental data from literature.

3.5.2 Biological data

We recall that the understanding of tumor cell properties is crucial to define good targets for therapy as it is expressed in [35]:

> "Qualitative and quantitative characterization of initiation [of tumor] would be of great value to understand chemical carcinogenesis and to design cancer prevention strategies."

In this paper, the authors investigate the tumor initiation in rat. The experiments and the HCC model are different from what is presented in Section 3.1.3 and focus on the role of cell replication and cell death but provide interesting information on the early stages

of tumor development. Indeed, it is difficult to follow the development of a single tumor over time because rats have to be killed to take a liver sample and produce the images (see figure 3.33). Moreover, in most experiments, the animals are killed after a long period of time to increase the probability to find a tumor which skips early carcinogenesis events observation (in Section 3.1.3 mice are killed after 8 or 9 months). The authors confirm the problem:

> "Because initiation is a rare event affecting only a few cells within a tissue and because in most models no specific markers for initiated cells are available, direct investigation is difficult."

Brief description of the experimental protocol and results:

In this experiment, the initiation of tumor is induced by injection of the genotoxic carcinogen N-nitrosomorpholine (NNM) and cells are marked with placental glutathione S-transferase (GST-P).

1. injection of NNM
2. apoptosis wave at 12h : 45% of damage at 36h
3. regeneration of liver starts at 48h
4. day 4: liver mass decreased to 48%
5. day 13: placental glutathione S-transferase-positive (G+) single cells reaching a maximum of 150 cm^2 section area.
6. day 24: absolute liver weight back to original

The authors split the results in 3 phases:

1. Phase I, from day 0 to day 14: continuous appearance of G+ single cells and their development to multicellular foci.
2. Phase II, from day 14 to day 28: regression of G+ cell clones. Due to the increase in liver mass after the first 2 weeks the decrease in G+ single cells and G+ lesions per liver was less pronounced than it appeared on histological sections.
3. Phase III, from day 28 to end: the numbers of G+ single cells and of multicellular foci appeared to stabilize and an increase in larger foci was observed.

Interesting information:
First division of initiated cells are aligned with sinusoids (see figure 3.33). The growth is columnar like in liver regeneration experiments. According to results of [43], this means that initiated cells may have an aligned division.

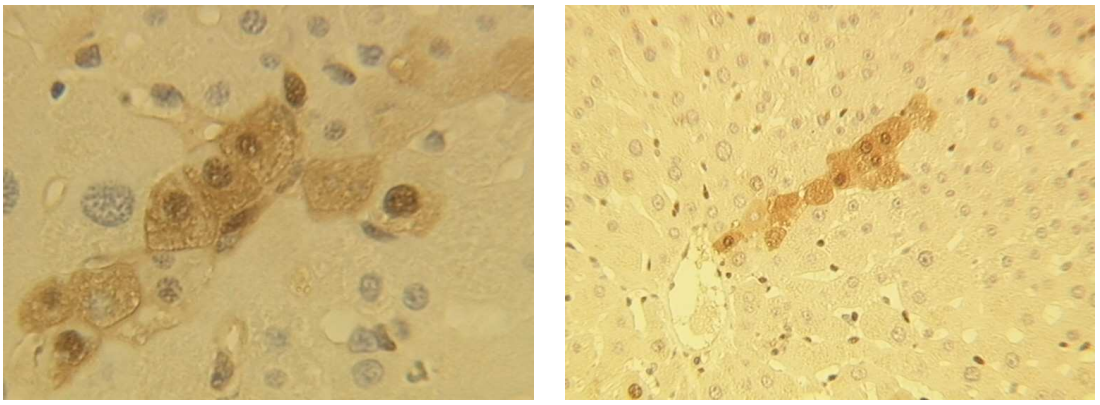

(a) day 23 (b) day 28

Figure 3.33: Columnar growth in rat HCC from two different rats: (a)rat killed 23 days after injection, (b) rat killed 28 days after injection. Stained cells (darker) have a monoclonal origin. The division is spatially ordered in column, which reflects cell phenotype. Images from [35] generously provided by the authors.

3.5.3 From elongated to spherical phenotype

In [43], the authors found that hepatocytes divide along their closest sinusoids during regeneration of liver, thus maintaining liver architecture. We referred to this order mechanism as hepatocyte sinusoid alignment (HSA). Simulations were performed assuming that vessels are soft and easily extendable by the expanding tumor. Here we perform equivalent simulations with modified tumor phenotype and a vessel stiffness of 1000 Pa, observed experimentally [9]. We observe that an aligned division (cells respect HSA) leads immediately to a more elongated shape (see figure 3.34, 3.35 and 3.36). However, this effect lasts until tumor population sizes of several hundreds of cells. For tumor sizes exceeding the distance between central and periportal vein, the elongation is expected to be lost as the sinusoids are oriented from the periportal area towards the central vein, and thus appear disordered on spatial scales large compared to individual size of a liver lobule. Hence, such an orientation effect can only be transient and our simulations suggest that by going from small to large tumors, asymmetries decrease, and besides, tumor cores becomes vessel depleted preventing HSA.

Results

We have performed different realizations of the tumor growth process. The different assumptions in these realizations do not affect tumor proliferation speed (data not shown). These show that despite the many random sources (growth, micro-motility) the tendency that tumor cells aligning along the vessels during division favor the formation of elongated tumors compared to tumor cells that divide uniformly into a random direction is observed in each of the realizations – meaning that the tendency is not due to particular initial conditions. Figure 3.36, upper line, shows that the longest axis is about 16 times longer than

HSA	TC / SEC adhesion	Elongation	Duration
No	No	–	–
No	Yes	+	–
Yes	No	+	+
Yes	Yes	++	++

Table 3.3: Cell phenotype and result on tumor shape.

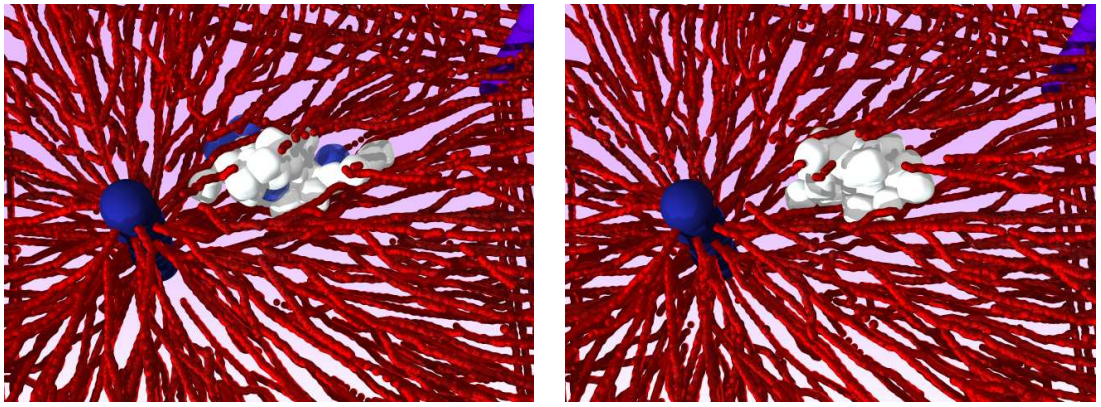

(a) Tumor cells divide preferentially along sinusoids as found for normal hepatocytes during liver regeneration (HSA)

(b) tumor cells divide into uniformly distributed into random direction.

Figure 3.34: Snapshots of a tumor in liver without tumor cell / SEC adhesion (healthy cells not represented, simulated time 99 hours, 32 tumor cells). Simulations with division along sinusoids (a) produce tumor with a more elongated shape than (b) without aligned division (see quantification in figure 3.36). The observed asymmetries are reproducible for different realizations (computer experiments) of the tumor growth process.

the axis perpendicular to the longest axis. This means that the 16 first cells are aligned in row. Moreover, the tumor cell surface area fraction accessible for the blood is slightly larger for tumor cells aligning during division along the vessels than for tumor cells that divide into random direction uniformly distributed. However, for tumor cell populations of $N > 600$ cells, the area slightly drops.

For 4 distinct scenarios with same parameters but different cell phenotype, the first divisions produce different shapes. The simulations with HSA clearly produce elongated shape for a certain time. This effect is enhanced by TC / SEC adhesion whereas this mechanism alone is negligible. In each case, the tumor growth speed is equal.

Discussion:

The simulations show that the aligned division mechanism is not sufficient with a 1000 pa vessel stiffness to obtain long column like in rat experiment (about 11 cells, see sample figure 3.33). Adding the tumor cell adhesion to the sinusoid endothelial cells (SEC)

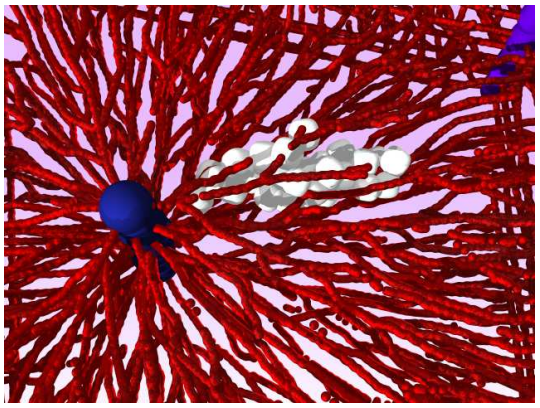

(a) Tumor cells divide preferentially along sinusoids as found for normal hepatocytes during liver regeneration (HSA)

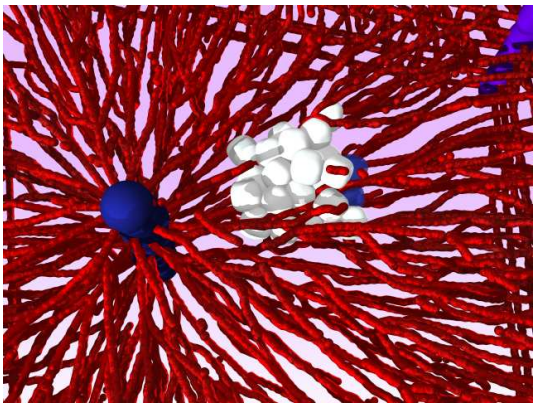

(b) tumor cells divide into uniformly distributed into random direction.

Figure 3.35: Snapshots of a tumor in liver with tumor cell / SEC adhesion (healthy cells not represented, simulated time 99 hours, 32 tumor cells). Again, the division along sinusoid produce tumor with a more elongated shape in (a) than in (b). This effect is more important with tumor cell / SEC adhesion as it is shown in figure 3.36.

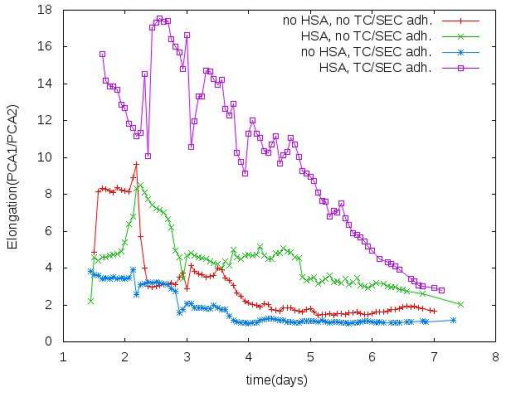

(a)

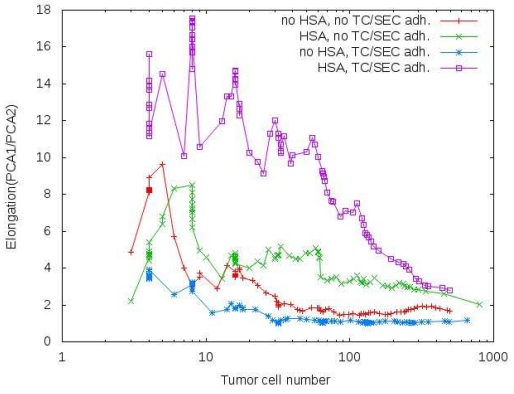

(b)

Figure 3.36: Quantification of the elongation in different simulations."Elongation" denotes the ratio of the longest axis of the tumor divided by the shortest axis perpendicular to it. A value of "1" denotes a perfectly spherical tumor shape. The aligned division along the sinusoid leads to more elongated tumor shapes (purple and green curve). The initial peak reflects the initial growth where tumor grows in a columnar order.

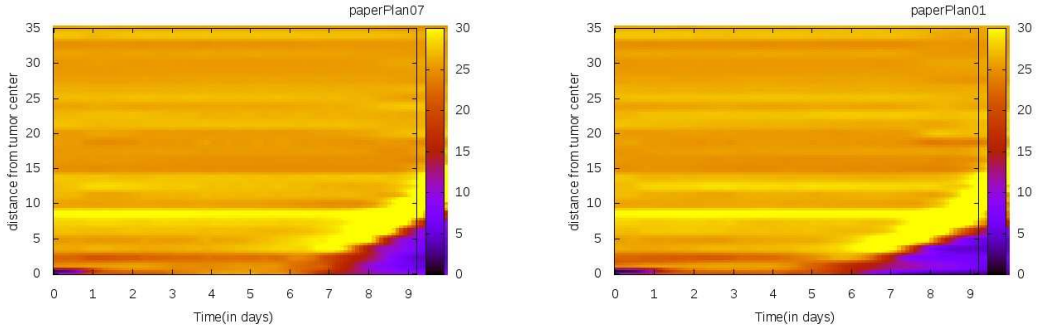

(a) HSA + TC/SEC adhesion.

(b) Random division alignment, no TC/SEC adhesion.

Figure 3.37: Density of endothelial cell in the tumor respect to the tumor cell number. Looking at first depleted values (above 5), the random division shows small SEC density at day 7 as for the same number of cells, the aligned division starts at day 8.

drastically increases the elongation whereas the adhesion alone produces a spherical tumor growth. Thus, in the same environment and with the same parameters, elongation tendency clearly reflects the tumor cell phenotype. The elongation vanishes as the tumor size increases which is amplified by the vessel depletion. The ratio of pressure exerted by tumor growth and the vessel stiffness determines the time point at which the depletion starts. The coupling of HSA and TC/SEC adhesion induces a columnar order that respects original lobule order and delays the vessel depletion (see figure 3.37).

Conclusion:
Tumor cell phenotypes that could be quantified may disappear at later stage of tumorous development. It is important not to look only at the final stage of the tumor (as experimentalists as well as clinicians usually do) but on the whole development phase. The whole analysis over time of the model permits to distinguish differences in cell phenotypes that end with the same tumor pattern. Before converging to a spherical symmetry, the tumor asymmetry reflects the tumor cell phenotype. Our simulations suggest that HSA is not enough to explain the pattern of initiated cells in [35]. These cells must not be to dedifferentiated and possess at least two hepatocyte mechanisms: HSA and SEC adhesion.

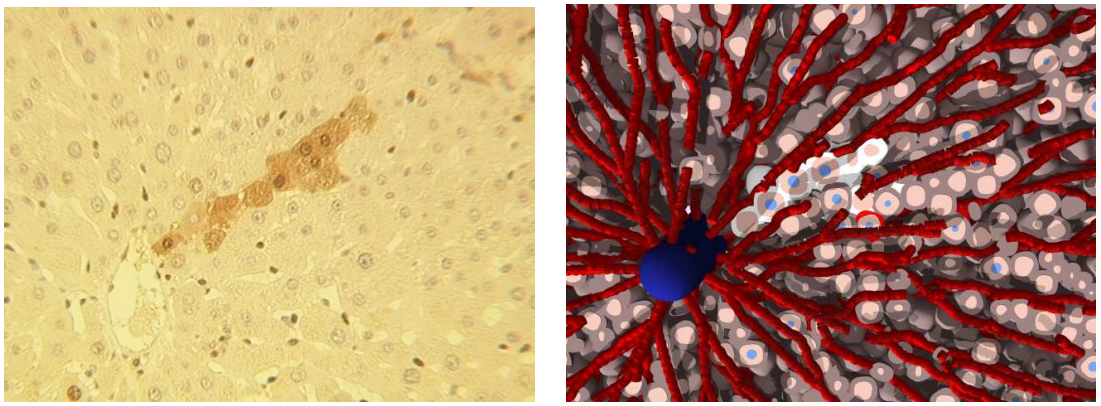

(a) Experimental input. (b) Simulation result.

Figure 3.38: Elongated growth by coupling division alignment and tumor cell/sinusoid adhesion: the model provides quantitative data to measure tumor elongation. Compared to biological data, the model suggests two necessary mechanisms to explain the pattern.

3.6 Simulation results after various stimulation patterns

In brief:
The possible number of combinations of assumptions is too large to be completely tested. However, we performed many simulations to explore the most realistic configurations. We presented in previous sections the most concluding ones. To obtain them, many simulations had to be performed. The results presented in this section are a selection of those, which guided the thinking and allowed us to present a straight forward reasoning and also to justify some affirmations in the argumentation line. Despite their modest influence on tumor growth, the stimulation patterns presented below permitted to understand the relevant mechanisms and discard the ones with small impact. Moreover, they obliged us to find new measurements and new strategies to reach the goals of the previous sections. We present the results here to show that our exploration was not restrained to only few mechanisms but covered a large span of possibilities.

3.6.1 The role of proteolytic enzymes destructing hepatocyte-hepatocyte contacts

As a reference we considered growing tumors in a hepatocyte environment without blood vessels. In this way the effect of blood vessels can be studied. We first compared the difference between two models of adhesion (model option 12.) in an environment of hepatocytes with and without vessel network (model option 1.). In these simulations, tumor cells do not adhere to other hepatocytes as established in the reference model. There is no bias for the random movement (model option 10.) and only the repulsive

forces are used to compute the pressure, i.e. we only use the positive contribution of the forces (model option 9.).

In both simulations, with and without proteolytic activity of the tumor cells on the environmental tissue, the tumor cell population sizes are almost equal over time (figure 3.39(f)). The total number of cells including normal and cancer cells is slightly larger in absence than in presence of proteolytic activity. Tumors grow exponentially fast but the tumor diameters differ between the two cases. Because the numbers are close, the difference in the radii results from different densities of the tumor cells. Both, the normal hepatocytes as the tumor cells are more compressed in absence of a proteolytic activity. This observation is supported by the observed difference in the spatial pressure profile (see figures 3.39(c), 3.39(d)). If tumor cells are able to destroy contacts between hepatocytes cells (figures 3.40(a), 3.40(b)) tumors can more easily expand into the tissue. In the following simulations we used relatively high pressure quiescence threshold to observe the tumor penetration in the tissue (BFI tumor 15 times higher than BFA healthy hepatocytes).

The results differ for same simulations (with/without proteolytic activity) but within a liver lobule i.e., in the presence of blood vessels. Due the pre-existent architecture, both, the tumor growth curves and the tumor radii are equal with and without proteolytic activity of tumor cells on neighboring normal hepatocytes. The blood vessels stabilize the organization of cells locally and largely compensates for the proteolytic effect of the tumor on its environment. Indeed the destructive effect of our model has a range of one cell layer at the border of the tumor.

3.6.2 Influence of the different pressure threshold to control tumor growth

Using the same model but different quiescent threshold for tumors, we observe that with smaller p_{Q_t} the tumors are smaller (figure 3.41). Interestingly, even if the threshold for quiescence of tumor p_{Q_t} cells is slightly below the threshold at which the normal hepatocytes undergo apoptosis, some normal cells die at a second pressure threshold p_{D_n}. The reason is that the evaluation of the pressure only takes place in the G1 phase while once tumor cells have passed S-phase they progress in cell cycle until they divide. They would increase in size even if the local pressure in the meantime exceeds the pressure p_{D_n} for example, because the cell volume increases. If not stated otherwise, we have chosen $p_{Q_n} = 0Pa$, $p_{D_n} = 3kPa$, and $p_{D_t} = 300k$ Pa (the subscript "n" denotes normal hepatocytes, "t" tumor cells).

3.6.3 The role of tumor cell adhesion

β-catenin is known to be able to affect adhesion between tumor cells ([72] and refs. therein). For this reason a key mechanism to be studied was the effect of adhesion between tumor cells, or between tumor cells and endothelial cells on the tumor phenotype. We consider the following mechanisms (snapshots of the simulations in figure 3.42):

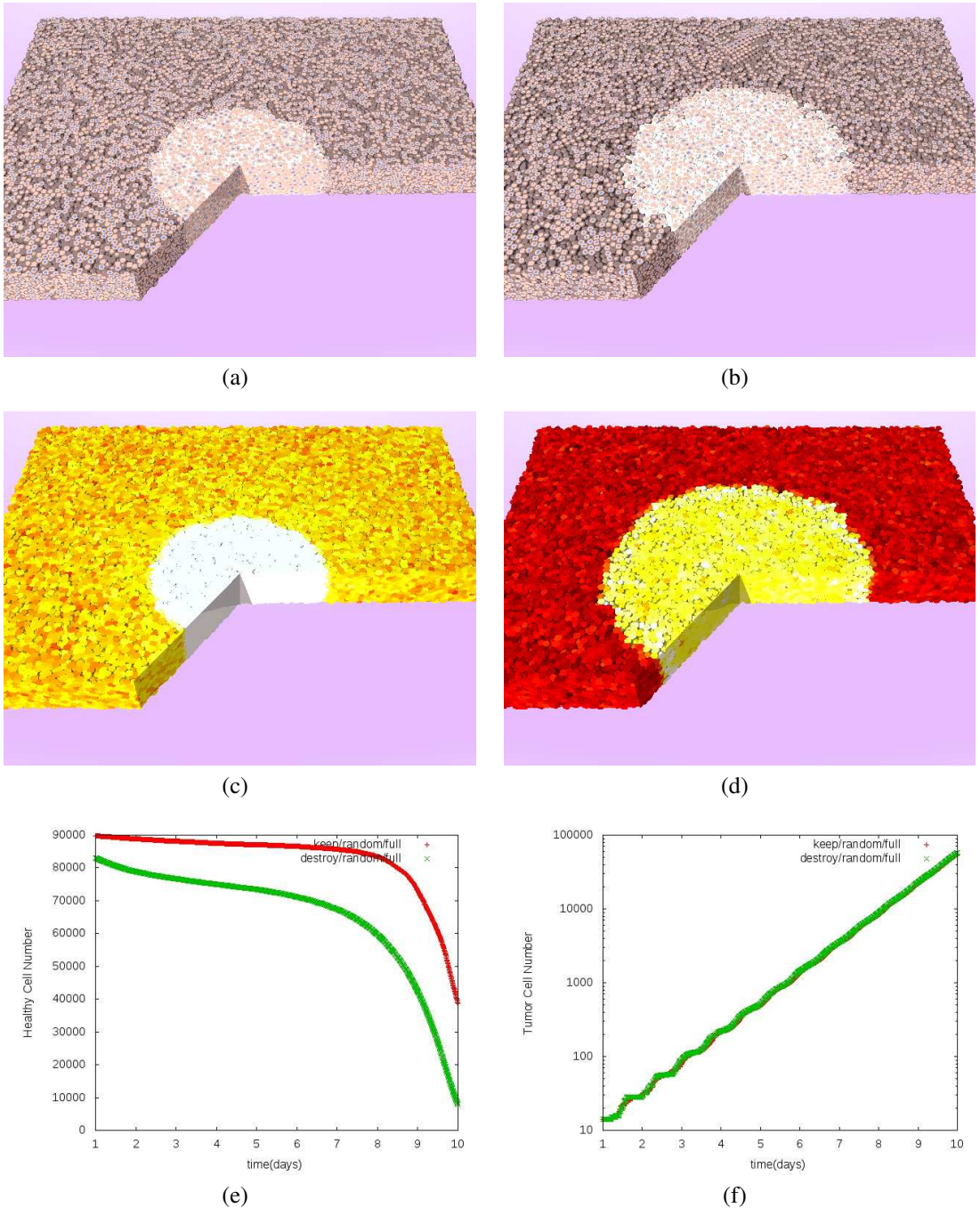

Figure 3.39: (a) A simulation of a growing tumor in multi-lobule environment after 8 days and (c) its corresponding pressure. The tumor cells do not destroy contact between normal hepatocytes. (b) The same simulation but the tumor is able to digest bonds between surrounding hepatocytes. (d) is the corresponding pressure of the system. (e) denotes the number of healthy cells, (f) the tumor population size (in these simulations, blood vessels were not considered).

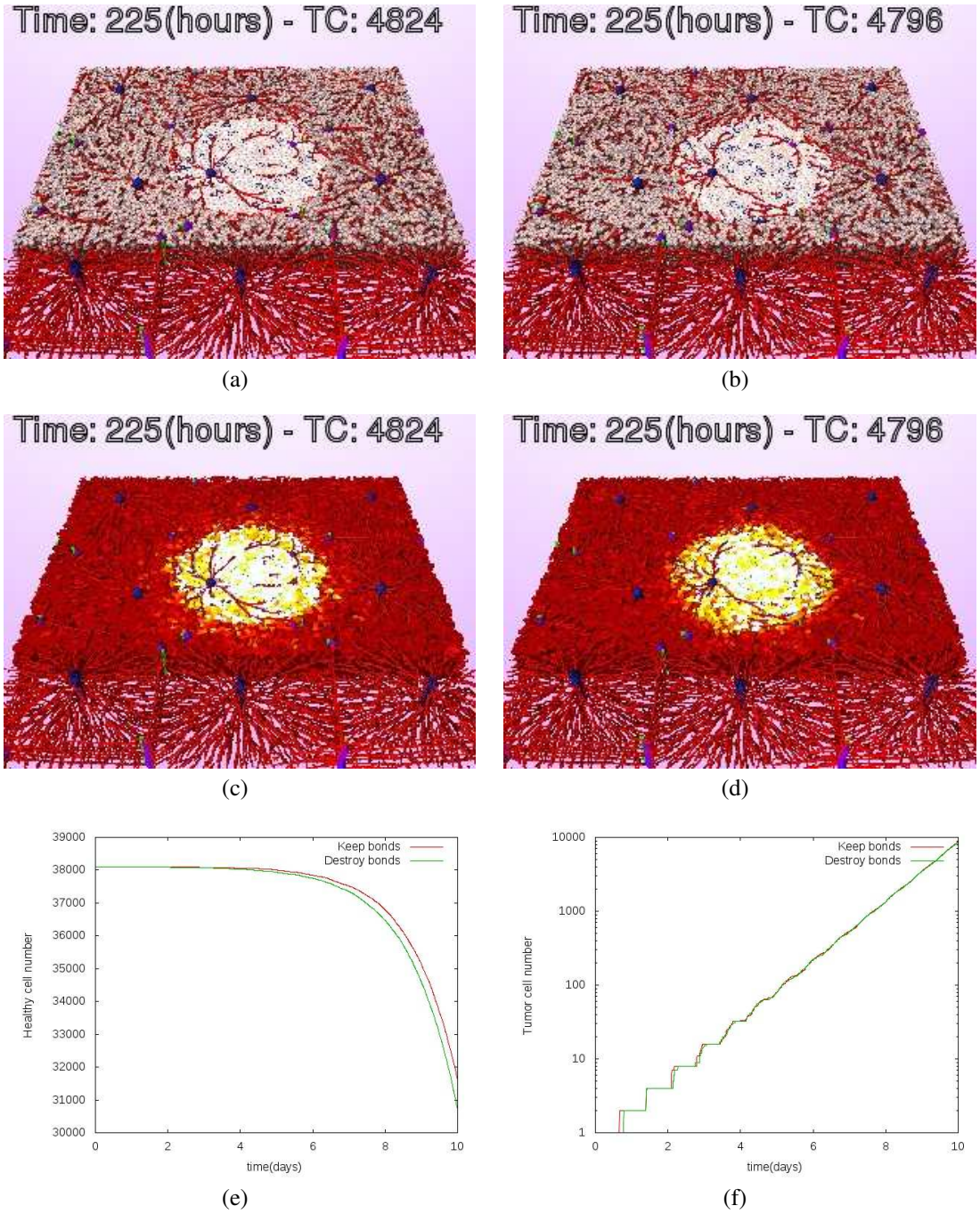

Figure 3.40: (a) a simulation of a growing tumor in multi-lobule environment after 8 days and (c) its corresponding pressure if the tumor cells do not destroy cell-cell contacts between normal hepatocytes. The pressure in the center (in the tumor) is higher. (b) The same simulation if the tumor cells are able to destruct the contact between neighboring hepatocytes. (d) is the corresponding pressure profile. The pressure is higher in the tumor. (e) denotes the total population size, (f) the tumor cell population size (in these simulations blood vessel were present).

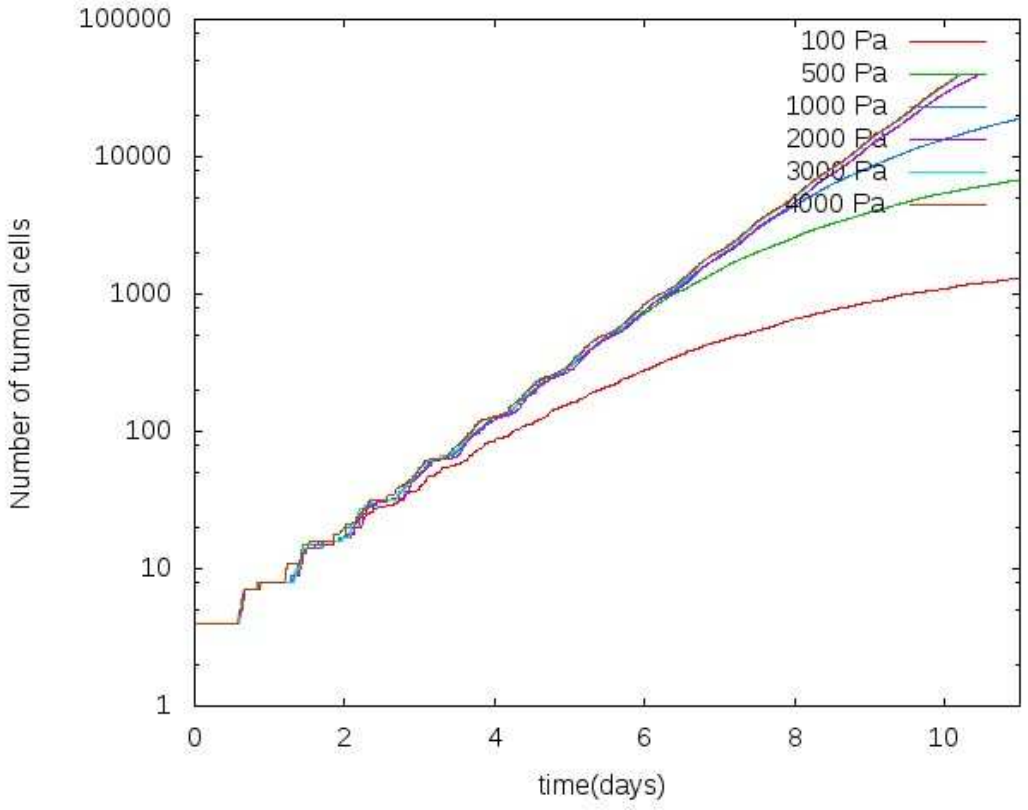

Figure 3.41: Populations of tumor cells. The lower the threshold of quiescence is earlier the growth of the tumor cell population crosses over to sub-exponential growth.

1. No adhesion, neither between tumor cells and endothelial cells, nor between tumor cells and either tumor cells or hepatocytes.
2. Adhesion between tumor cells and either tumor cells or hepatocytes.
3. Adhesion between tumor cells and endothelial cells as well as between tumor cells and hepatocytes.

While visually, it is difficult to detect differences between the different situations, a plot of the radius of gyration versus the tumor cell numbers shows that in case of no adhesion the tumors are least compact while in case of adhesion between tumor cells and endothelial cells as well as tumor cells and hepatocytes, the tumors are most compact (figure 3.43).

As shown in figure 3.44, the contact area hepatocytes shared with sinusoids shows the largest value if tumor cells and sinusoidal endothelial cells adhere (blue curve in figure 3.44(a)). Here the contact area represents the surface area of a tumor cell, which is accessible to blood, i.e. the contact area with sinusoids. If there is no adhesion between tumor cells and sinusoidal endothelial cells, then the contact area is significantly smaller if tumor cells adhere to other tumor cells (green curve in figure 3.44(a)). This is also reflected in the number of sinusoidal endothelial cell (SEC) elements vs. the tumor cell population size (green curve in figure 3.44(b)). If tumor cells cohere (and adhere with hepatocytes) then the tumor forms a compact mass as in this case tumor-tumor cell contacts are energetically favored over tumor-cell-endothelial cell contacts. This explains why the contact area as well and the SEC vs. the tumor cell number are smaller than in the other two cases. If tumor cells do not adhere at all, neither to other tumor cells, to hepatocytes or to sinusoidal endothelial cells (red curve in figure 3.44(a)), then the contact area of hepatocytes to endothelial cells is close to the that of tumor cells that adhere to SECs. The reason is that the pressure generated by proliferating tumor cells in the region of the tumor slightly increases the local cell density, so tumor cells are pushed against SEC. As there are not competing effects such as cohesion between tumor cells (as for the green curve in 3.44), the values for contact area and SEC elements is close to that for the case where tumor cells and SEC adhere (blue curve in 3.44).

As we demonstrate for tumor cells adhering to sinusoidal endothelial cells (SECs) but not to other tumor cells or to hepatocytes, the contact area decreases for larger tumor sizes. For large tumor sizes, vessels are pushed and a vessel depletion zone occurs. However, the vessels are found to still remain within the tumor. Hence the vessel density, calculated from sufficiently large volumes, is still maintained. Only the order of the vessel network is affected. Hence, our simulations suggest that by going from small to large tumors, asymmetries as well as vessel order may decrease while the number of vessels remaining inside the tumor increases as in normal liver.

3.6.4 Tumor Cell motility

Aberrant β-catenin degradation leading to β-catenin entrance into the nucleus has been described as a mechanism promoting tumor cell invasion. For this reason we studied

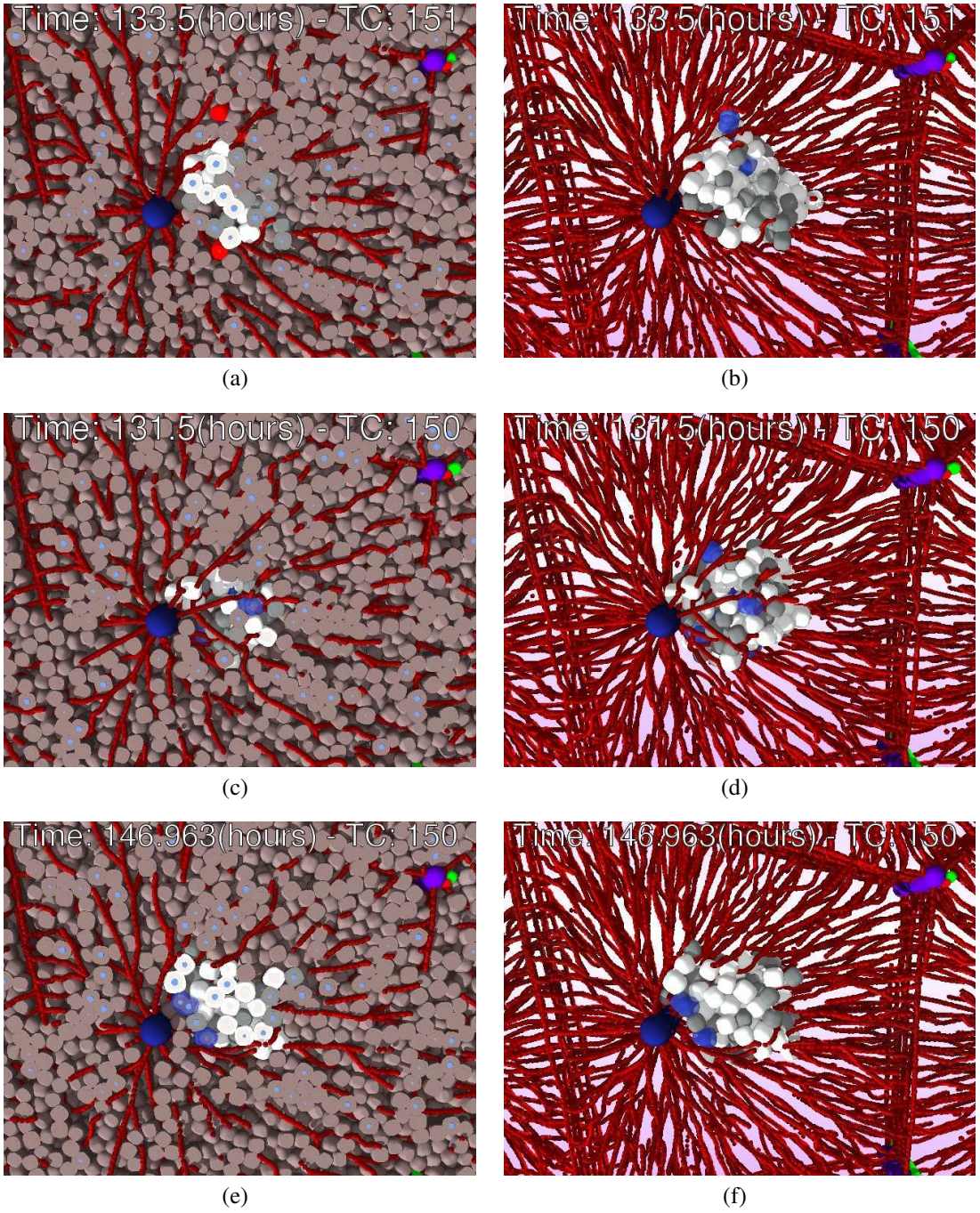

Figure 3.42: Snapshots from simulations. On the left side, the tumor is represented in this environment with healthy cells. On the right side, the corresponding image where only the tumor is represented. Proliferating tumor cells are in white, quiescent tumor cells are in gray, dividing tumor cells are in blue, healthy cells are in brown and red when apoptotic. In (a) and (b), the tumor cells adhere to other cells (healthy or tumorous), in (c) and (d), tumor cells adhere to other tumor cells and to endothelial cells. In (e) and (f), tumor cells do not adhere at all.

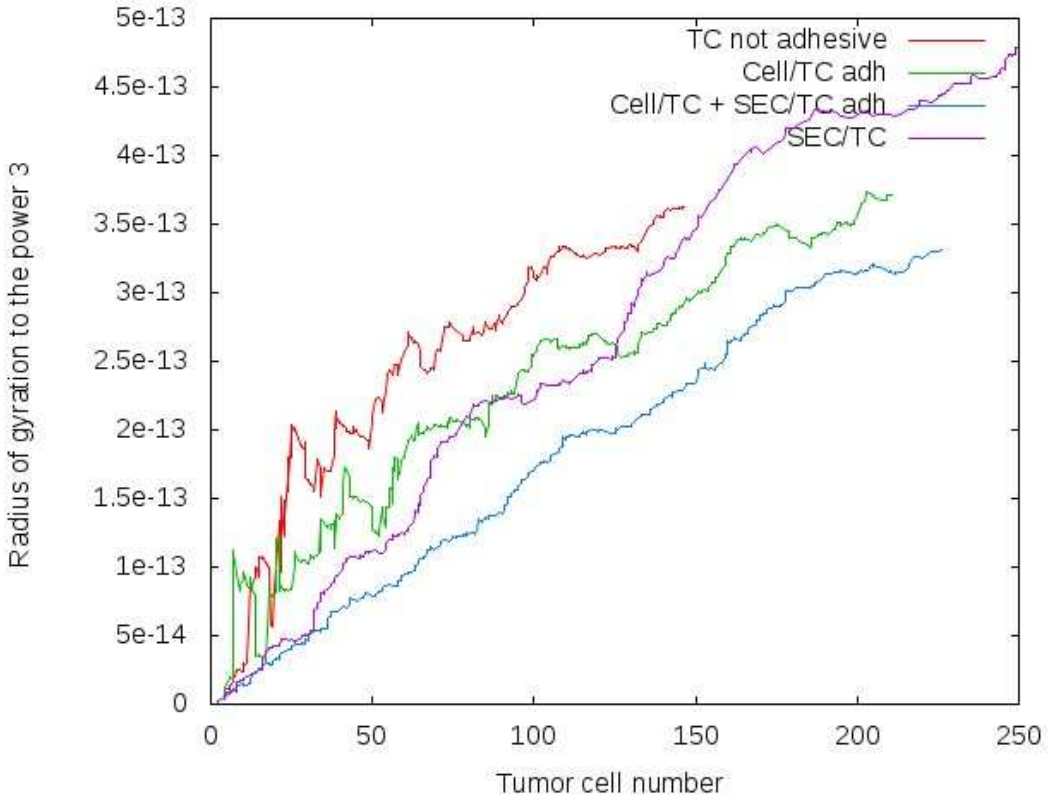

Figure 3.43: Radius of gyration of different tumors with respect to the tumor cell number. The curve legend refers to the adhesion: "TC not adhesive" means no adhesion, neither between tumor cells nor between tumor cells and endothelial cells, "Cell/TC adh" denotes that cell/cell adhesion is present, and "Cell/TC + SEC/TC adh" the presence of adhesion between tumor cells on one hand, and endothelial as well as tumor cells and normal hepatocytes on the other hand. We observe that the compactness of the tumor is dependent on the adhesion mechanisms.

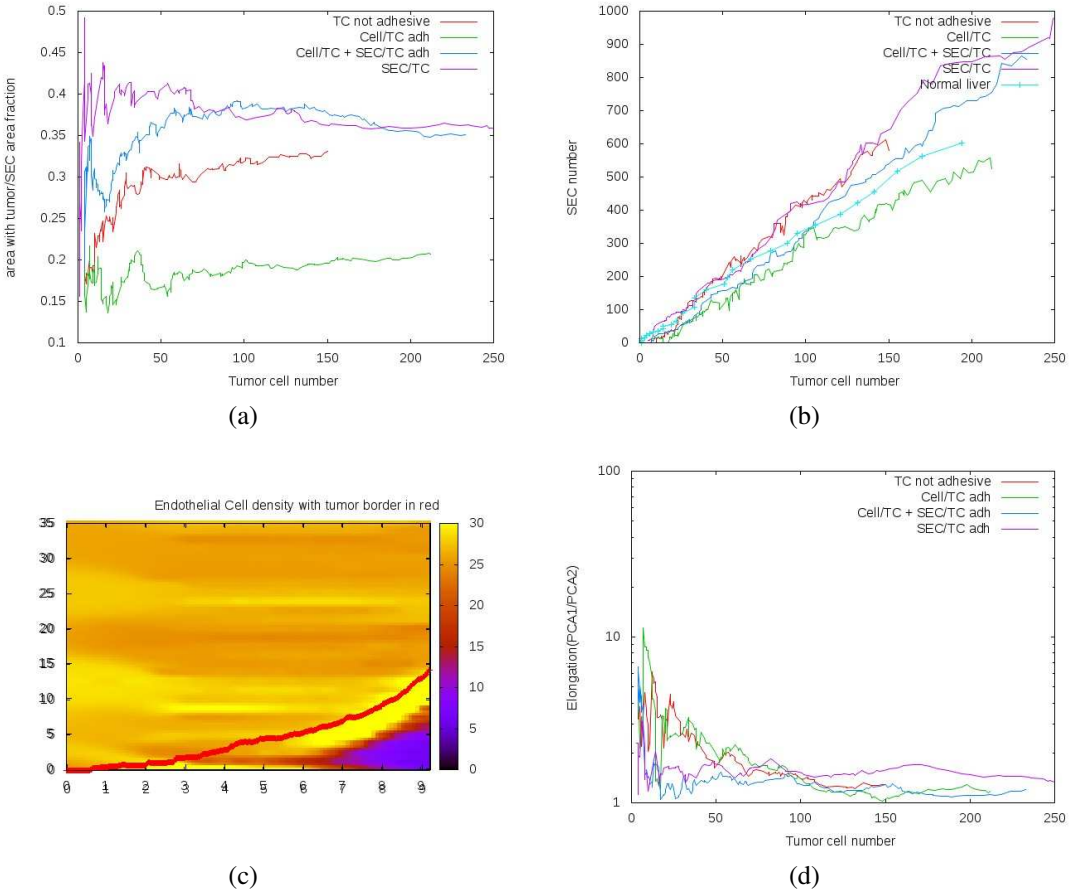

Figure 3.44: (a) Contact area hepatocyte – sinusoid vs. logarithm of tumor cell population size. (b) Number of SEC elements as a function of the tumor cell number. (c) plot of endothelial cell density vs. distance from tumor border (y-axis) and time in days (x-axis: days 1-9) for the case where tumor cells adhere to SECs but not to other tumor cells or to hepatocytes. The red line indicates the tumor border. The tumor develops a depletion zone in the center after about 6 days. At the same time, the endothelial cell density close to the tumor margin but still inside the tumor increases. (d) In all considered cases, the tumor adopt finally (at about $N > 100$ cells) a circular shape even though for the case of only adhesion between tumor cells and SECs a moderate tendency towards growth along the sinusoid can be seen. This can be seen from the "elongation" vs. N plot. The elongation is defined as the ratio of the longest axis divided by the shortest axis. For $N > 100$ tumor cells it is close to 1 saying that the longest and the shortest axes are approximately equally long.

how tumor cell micro-motility may affect the growth speed and phenotype of a tumor. As shown in figure 3.45(a) the speed of growth varies only slightly without any systematic ordering between our reference value for the tumor diffusion constant, and smaller or larger values of the diffusion constant. The observed variability can be explained by stochasticity of the growth and migration process. This is supported by the figure 3.45(b). The third power of the radius of gyration as a function of the tumor cell number shows no clear differences indicating that the relation between tumor shape and tumor cell population number is insensitive to the diffusion constant. Moreover, the linear relationship indicates that tumors are compact at least up to 100 tumor cells. We expect an effect of micro-motility only if cells detach and follow a morphogen gradient as in cancer invasion. Without such a gradient the pressure by the hepatocytes surrounding the tumor inhibit detachment of individual tumor cells from the main tumor and migration into the tissue environment. The fraction of surface area accessible to hepatocytes grows slowly with the tumor cell number and saturates at about 30%. For more than about 120-150 tumor cells the curves flatten. Looking at the simulation videos suggest that at this point the periodic boundary conditions in z-direction slightly modify the curve.

3.6.5 Tumor cell mechanical softness

It is known that some tumor cells are often softer than the cells of the tissue they originate from. For this reason we study here the effect of reduced tumor cell elastic modulus – the Young modulus – on the tumor expansion (figure 3.46). We observed that the tumors are more compact for softer than for stiffer tumor cells. This can be explained as the resistance to deformation decreases with decreasing Young (elastic) modulus. The shape of the tumor remains unaffected by the stiffness of the tumor cells (figure 3.46).

3.6.6 Endothelial cell proliferation

As shown by [19] proliferating hepatocytes during regeneration trigger proliferation of sinusoidal endothelial cells. For this reason we tested the assumption that endothelial cells, once under tension, trigger endothelial cell proliferation in order to relax the tension. In particular, we assume that proliferation is triggered if locally a two-fold stretch occurs. Despite a decreasing vessel density within the tumor resulting from vessels stretched and pushed out of the tumor center by proliferating tumor cells (figure 3.47), proliferation of sinusoidal endothelial cells with this mechanism could not be observed. We believe that the vessel network distributes the constraint over the whole network so that locally too large stretch does not occur. This has been checked with different measures: mean distance among SEC, mean angle, and SEC number (data not shown). The stretch could occur only if the tumor growth was too fast for the vessel network relaxation time. We think that this mechanism does not play a role in the tumor's growth at least on the spatial scale of individual liver lobules neither in its vascularization as long as the local increase of tumor mass is not too fast.

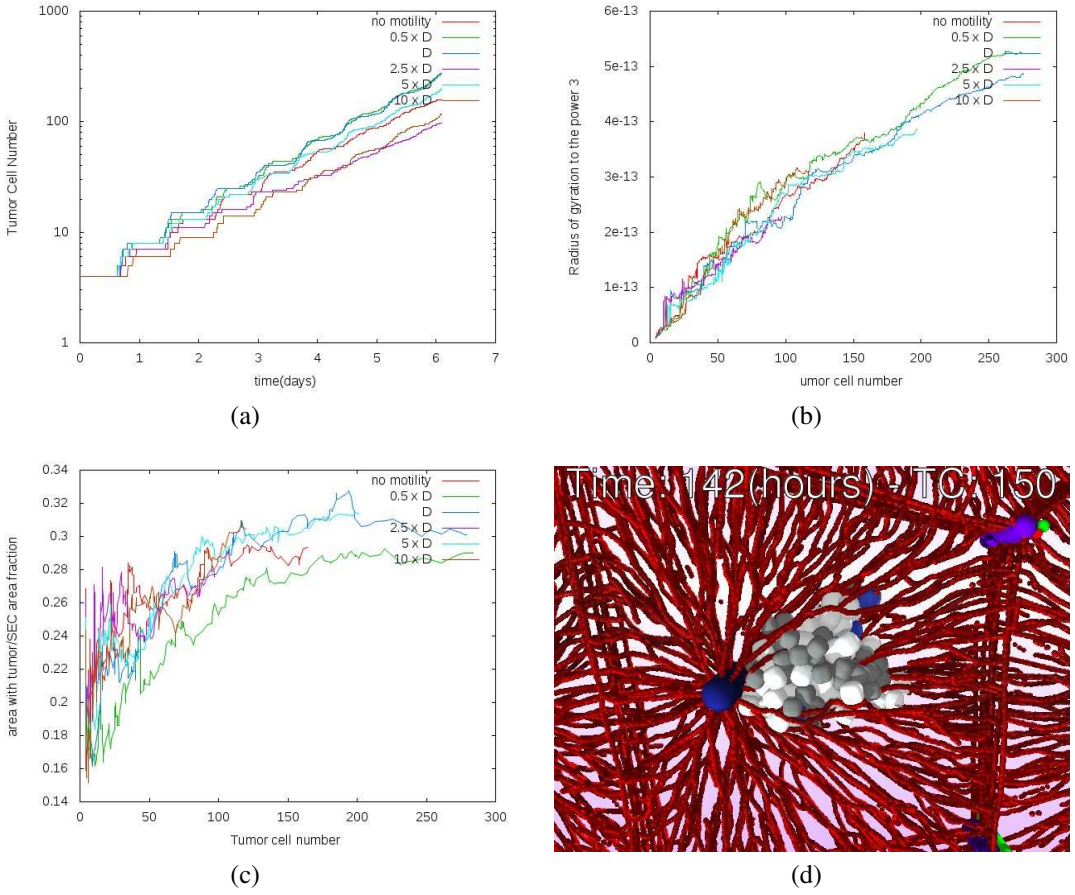

Figure 3.45: (a) log of tumor cell number vs. time. (b) radius of gyration vs. tumor cell number. (c) contact area vs. tumor cells number. (d) snapshot from simulation with micro motility $0.5 \times D$.

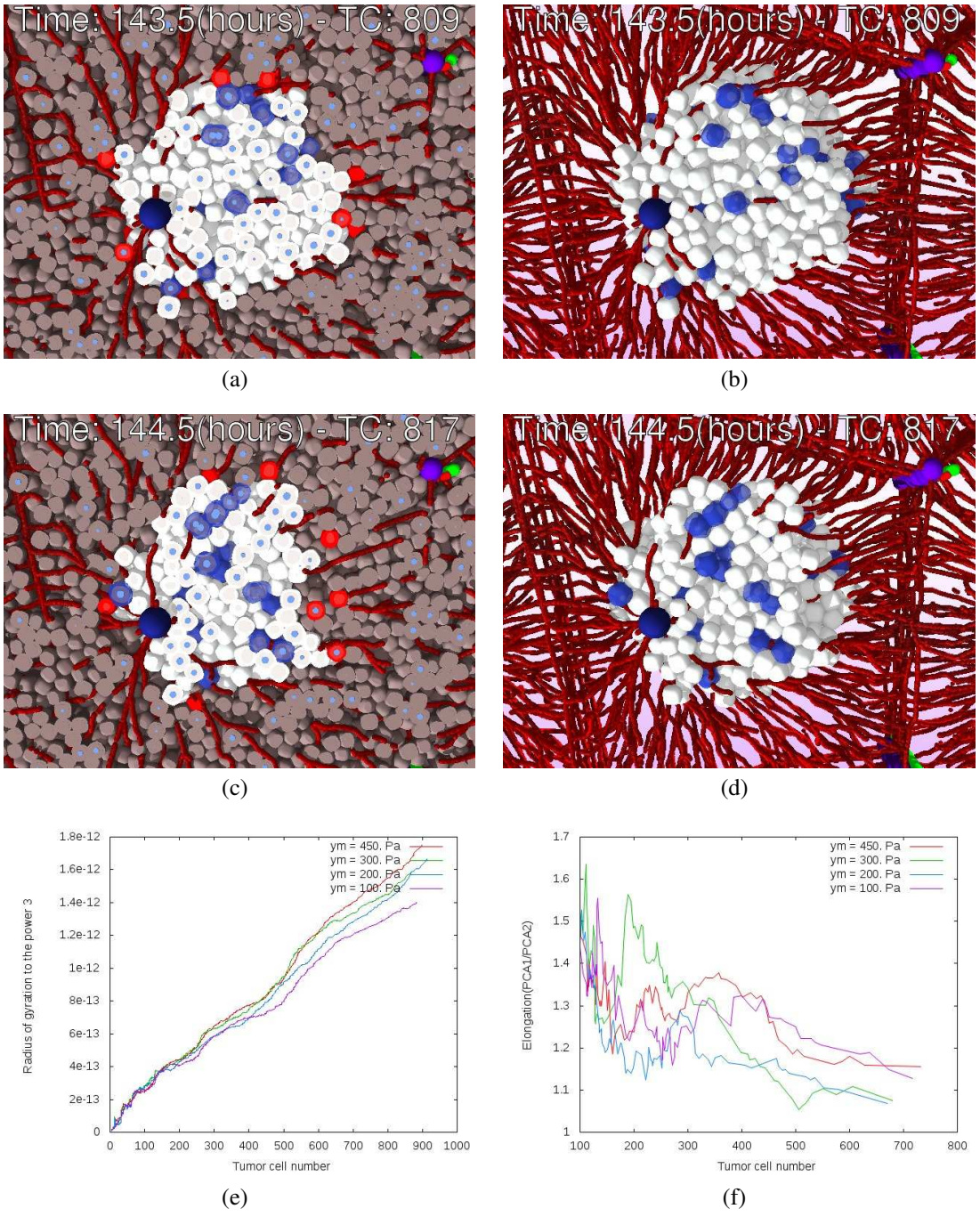

Figure 3.46: Snapshots from simulation of tumor growth with different Young moduli. On the left (a) and (c), the tumor in its environment and the right (b) and (d), the corresponding images where only tumor cells are shown. The first line (a) and (b) shows a simulation with tumor cell Young modulus of 450 Pa, the second line (c) and (d) a simulation with 100 Pa. We observe that the shapes all converge to the sphere despite a difference in volume for the same number of tumor cell although they did not already reach a spherical shape at 700 cells.

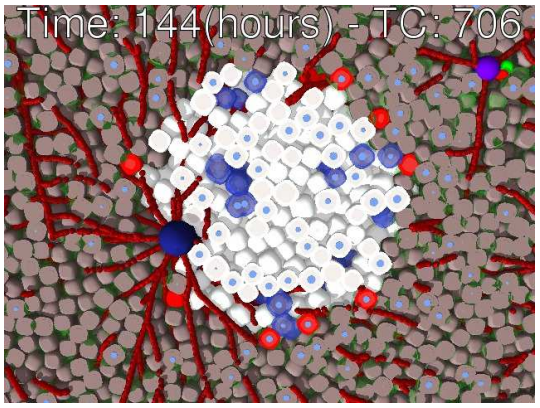

(a)

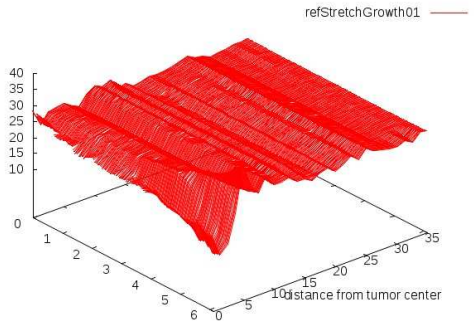

(b)

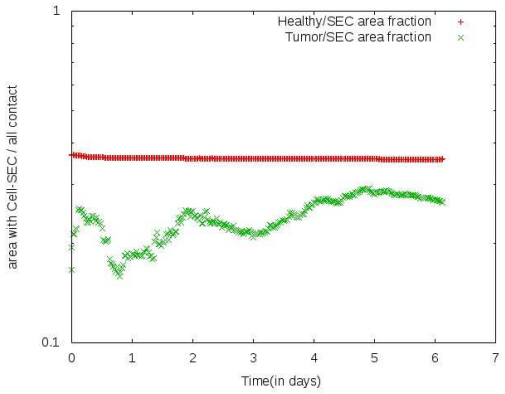

(c)

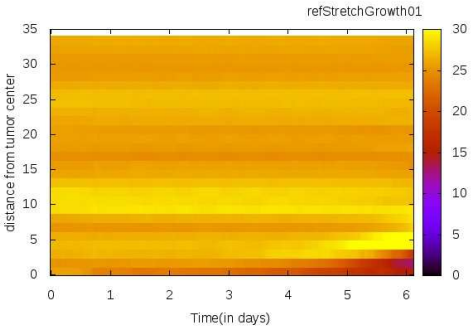

(d)

Figure 3.47: (a) Snapshot from simulation where at a too large stretch endothelial cells divide so that the vessel stress is relaxed. (b) Corresponding vessel density within the tumor respect to time and tumor center distance. Vessels are pushed but not stretched enough such that for the considered tumor sizes, vessel division does not occur. (c) Logarithm of the fraction of the contact area between tumor cells and sinusoidal cells vs. time. The cell cell contact is about 20% below that in normal liver. (d) at about 5-6 days a reduction of sinusoids occur in the tumor, pushing and stretching vessels in agreement with the picture (b).

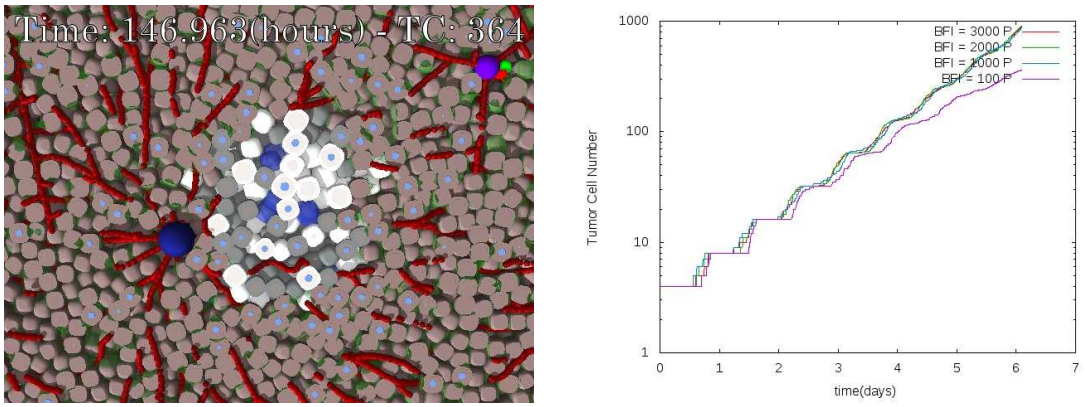

(a) (b)

Figure 3.48: Screenshot from simulation with BFI = 100 Pa. The large number of quiescent tumor cells (in gray) explains the deviation of the growth from the exponential.

3.6.7 Healthy cell death

Tumor development in the mouse model studied in this consortium indicates occurs over several months. For example, mice have been sacrificed after 9 months after APC knockout and tumors been found [15]. In our models we had assumed that tumor cells of the expanding tumor exert pressure on the surrounding hepatocytes triggering hepatocyte apoptosis above a threshold pressure. On the other hand, tumor cells do not re-enter the cell cycle if the pressure exerted on them exceeds another threshold value that we referred to as BFI (see 3.2). If BFI is small, tumor cells have an increasing probability to not re-enter the cell cycle. In order to demonstrate the effect of this parameter on the tumor growth we varied the BFI between 100Pa and 3000Pa. A large BFI facilitates tumor cell proliferation even at large pressures. Figure 3.48(b), shows the growth of the cell population size vs. time in a plot of log(N) vs. time. For small tumors growth is exponential. As the tumor size increases, a deviation from exponential growth is observed if the BFI is small (300 Pa). With increasing tumor population size, the pressure inside the tumor increases eventually exceeding the value for BFI. The smaller the BFI, the smaller is the tumor size at which the pressure in the tumor center exceeds the BFI value. Accordingly, the crossover from exponential to sup-exponential growth is expected to occur at larger tumor sizes if the BFI is large and at smaller tumor sizes if the BFI is small. However, eventually, it must always occur. On the other hand, we did not find any effect of the BFI on the tumor phenotype.

3.6.8 Tumor cell-cycle entrance propensity

To further explore if the relaxation matters in the appearing tumor phenotype, we simulated tumor cells with different propensity to divide (figure 3.49). At the end of the mitosis, the two new cells decide independently to enter or not the cell-cycle (if they undergo a pressure below the BFI). Once the cell made its choice it is definitive, it stays

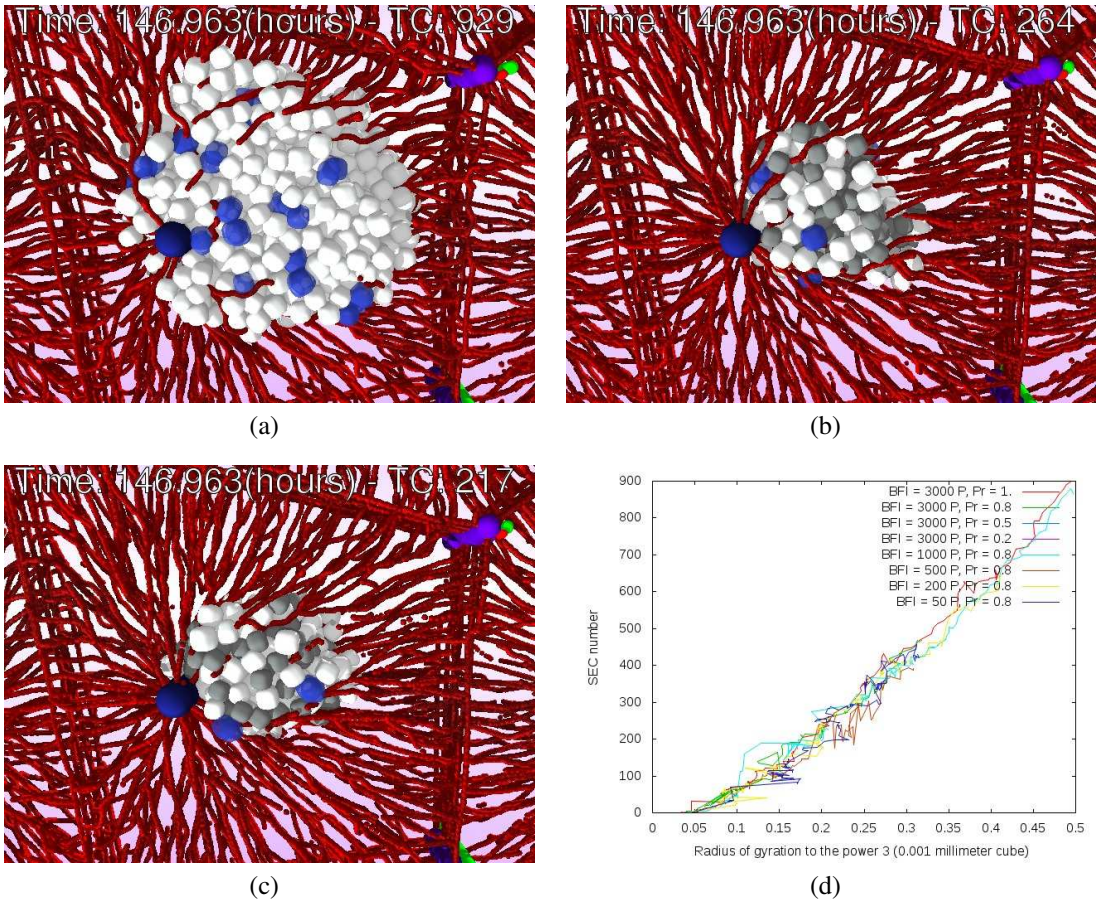

(a) (b) (c) (d)

Figure 3.49: Screenshots from simulation with different probability to proliferate and different BFI (only tumor cells represented). (a) reference simulation with probability 1. And BFI 3000 Pa. (b) Probability to re-enter the cell-cycle is 0.8 and BFI is 1000 Pa. (c) Probability to divide is 0.8 and BFI 200 Pa. For all simulations, the healthy cell BFA is 200 Pa. We could not observe significant differences among the simulations. We show here only the vessel density within the tumor respect to the radius of gyration.

quiescent. We tested different probability combined with different BFI. Those simulations confirmed the previous ones; the mechanical relaxation at the studied tumor sizes is fast enough to be insensitive to the tumor growth law (which is exponential) and thus cannot explain difference in the tumor phenotypes.

3.6.9 Beyond small tumor nodules

We studied the effect of larger tumors in figure 3.50(a) for tumors where tumor cells (TCs) adhere to sinusoidal endothelial cells (SECs) but not to other tumor cells. This mechanism has been found in Section 3.5 to resemble a well differentiated phenotype. The results for TC-TC adhesion and no adhesion, neither among TCs nor between TCs and SECs have

been discussed in Section 3.5 and are only shown for comparison. It turns out that with increasing tumor size vessels are pushed out of the center (figure 3.50(b)). However, they are not moved to the tumor border, but stay within the tumor. As the sinusoidal network is modified inside the tumor, the angle distribution of the vessel elements is modified (figure 3.50(c)). However, as the SEC depletion zone in the tumor center is accompanied by a SEC high density zone at its border but still within the tumor, the total number of SECs inside the tumor changes with the tumor cell population size as for small tumor sizes (figure 3.50(d)). In figure 3.51, we show a 2D projection of SEC in contact with tumor cells and within the tumor.

3.6.10 Simulation of drug injection

The model setting

In this final section we made a first very simple step towards including cell death as it occurs during drug therapy in a simplified caricature of a tumor. However, the model framework permits readily an application of the framework to treated tumor nodules in the multi-lobule model. In this section we considered tumor cells as not adhesive (Hertz force) while (healthy) hepatocytes were assumed to be adhesive and modeled by the JKR-model. Several other options and parameters were as in previous simulations. We here did not model the blood vessels as there influence on cell death due to drug effects are small as long as the tumor is sufficiently vascularized which can be assumed to be the case for tumors not exceeding the size of a lobule. Consequently, cell division cannot be oriented along vessels so is random and uniformly distributed, no morphogen attraction, no hepatocyte - sinusoid adhesion, and no tumor cell - sinusoid adhesion is considered. The vessel plays an important role in remodeling the tissue architecture so is interesting to consider them in re-growth. However, in any case as the simulations considering sinusoids, central and periportal veins are an order of magnitude slower than those without blood vessels, one would in any case in a first step perform exploring simulations without blood vessels before considering the whole organ model with the correct micro-architecture.

We further assume that healthy hepatocytes are quiescent and die if and only if they have been in contact with a tumor cell and experience a pressure larger than 200 Pa. This pressure effect might rather mimic an apoptotic signal, as usually much larger pressures are needed to kill healthy cells. However, the consequence would be the same. Tumor cells are proliferative unless they experience a pressure higher than 3000 Pa. We considered periodic boundary conditions, where the thickness of the box was 5 cell diameters in z-direction, and 75 cell diameters in x-and y-direction.

Results

Typical spatial tumor profiles in a cross section are shown in figure 3.52 12 hours after drug treatment if no cell, 10% of cells, 90% of cells, or 99% of cells are killed by the drug and phagocytized. Interestingly, even for 90% cells, the emerging tumor depletion zone is filled with cells despite macrophages have not been considered.

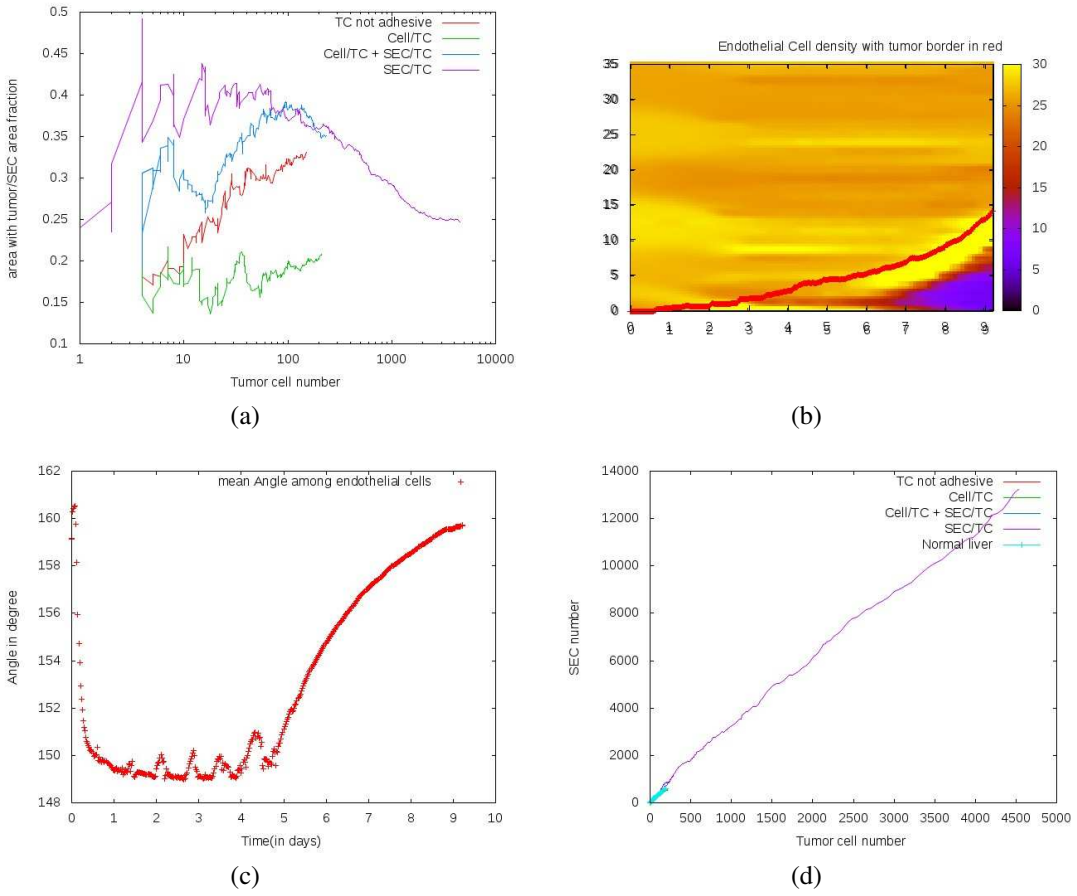

Figure 3.50: (a) The contact area between tumor cells and SECs drops significantly beyond a tumor cell population size of several hundreds of cells. (b) SEC density vs. time in days (x-axis) and distance from tumor center (y-axis). From day 6, a depletion zone appears inside the tumor. However, around the depletion zone, the SEC density is higher than in normal liver tissue. As indicated by the red line the high-density SEC-zone is inside the tumor border (shown by a red line). (c) The depletion zone modifies the angle distribution of the sinusoidal elements indicating that tumor cells bend the vessel network. The oscillations below 5 days indicate transient relaxation effects. (d) The SEC number remains unaffected by the tumor cell population size confirming that the depletion zone is enclosed by a zone of stronger vascularization. Different from the case of soft vessels with low stiffness (Section 3.2) the zone of stronger vascularization is inside the tumor so the total number of SECs forming the sinusoidal network inside the tumor still increases linearly with the tumor cell number with the same slope as for small tumors. Moreover, the number of SECs grows with the number of TCs with the same slope as the number of SECs with the number of hepatocytes in normal non-tumor liver (short light blue line).

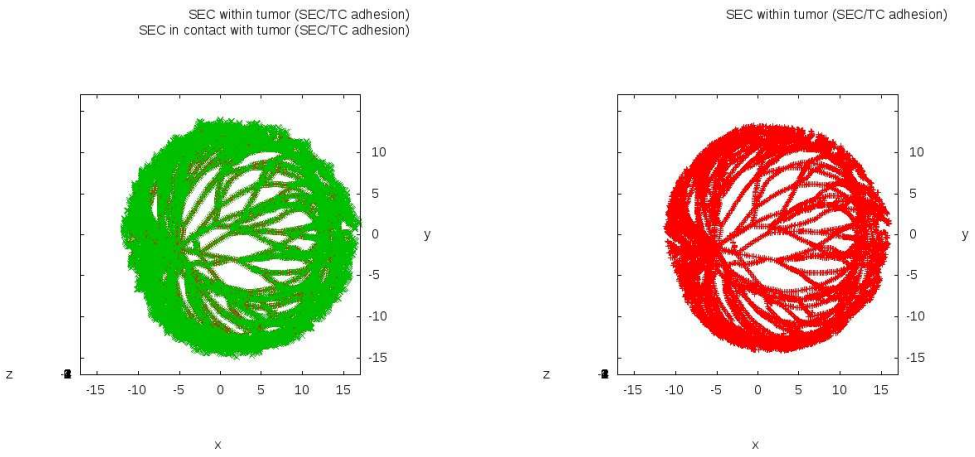

(a) (b)

Figure 3.51: 2D projection in case of SEC/TC adhesion of the SEC in contact with the tumor (green) and within the tumor (red). The tumor is compact and it is possible to compute its the convex hull. We then can distinguish SECs that are inside the convex hull from them that are outside. The convex hull is computed with the tessellation library from Nick Jagiella.

Figure 3.53 shows the corresponding regrowth curves. They are all exponential up to several 10000 cells. The radius of gyration grows linearly for the non-sensitive tumor (0%) killed and the one where 10% was killed. For the tumors with 90% and 99%, respectively, re-growth of the radius of gyration is strongly delayed. This is because the 90% and 99% first re-grows to fill the gap at almost zero cell compression until it starts to sense the presence of the other cells. Hence the compactness of the tumor increases when it feels the presence of the (healthy) hepatocytes.

The different scenarios are reflected in the pattern and pressure profiles after 2 days (figures 3.54,3.55,3.56,3.57). The larger the tumor, the larger is the compression from the surrounding tissue. Consequently, the mechanical stress in the most drug-sensitive tumors (90% and 99%) passes intermediately small values (figures 3.56 ,3.57) while the insensitive tumor (figure 3.54) and the low sensitive tumor (figure 3.55) do not. For the most drug sensitive tumor (99%), even after 4days the compression is still moderate. This explains the slow convergence to compactness in figure 3.53 for the most sensitive tumor phenotype. However, interestingly, the in all cases re-growth occurs to solid compact tumor phenotypes. We conclude that without a change of the cell phenotype, the external pressure exerted by the surrounding hepatocytes seems to be sufficient to ensure maintenance of a solid tumor phenotype.

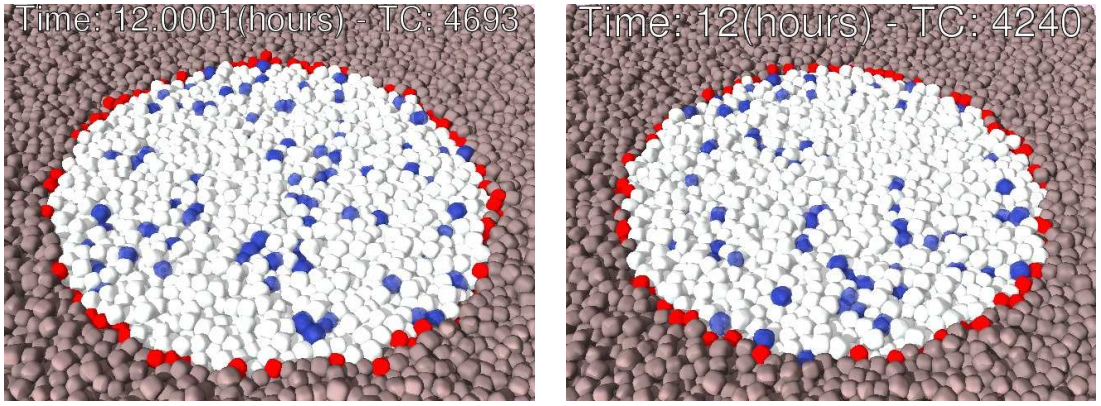

Figure 3.52: Simulations 12hours after drug injection (death is immediate). (a) 0% killed, (b) 10% killed, (c) 90% killed, (d) 99% killed. Brown cells: healthy cells, white cells: proliferating tumor cells, gray cells: quiescent tumor cells (not appearing here), red cells: apoptotic cells, blue cells: tumor cells in mitosis.

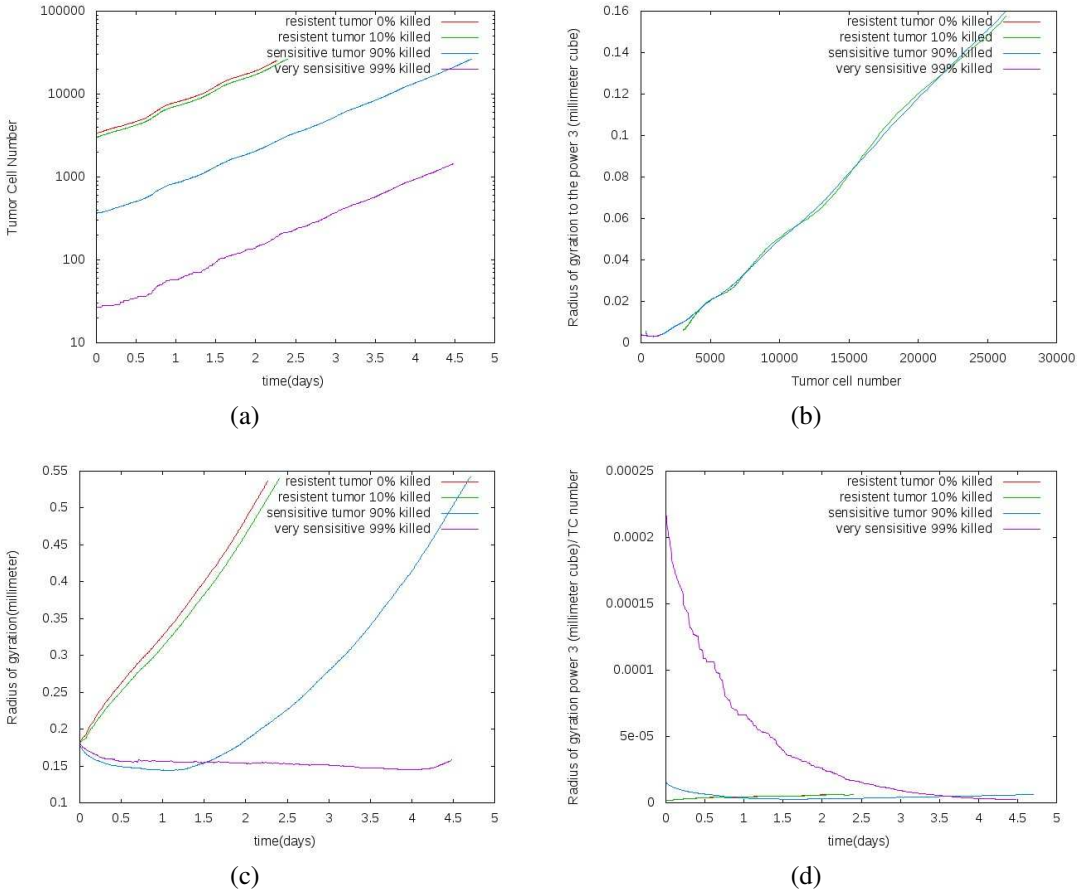

Figure 3.53: Plots of the 4 different cases. Growth curves are parallel (a) and compactness equivalent for the same number of tumor cells (b). (c) For about 4 days the radius of gyration is very low in the 99% case because the tumor is sparse after drug injection. Only then regrowth of the radius of gyration starts despite the number of cells is already increasing. This is reflected also in the compactness measure (d) vs. time. With increasing time the third power of the radius of gyration divided by the number of cells divided by the time decreases for the almost depleted tumor until the depletion zone generated by the drug is filled with tumor cells again (Figure 3.52).

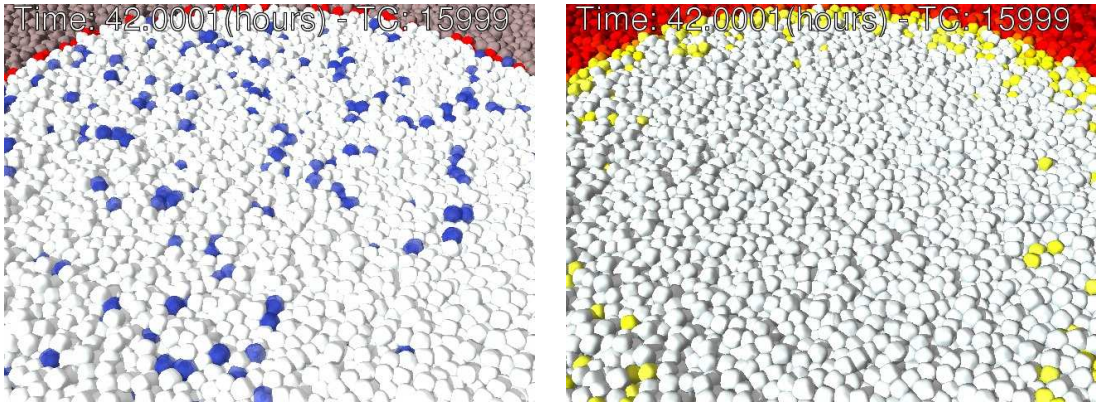

(a) (b)

Figure 3.54: (a) Simulation with resistant tumor after 2 days. (b) The corresponding pressure. (same legend for all images)

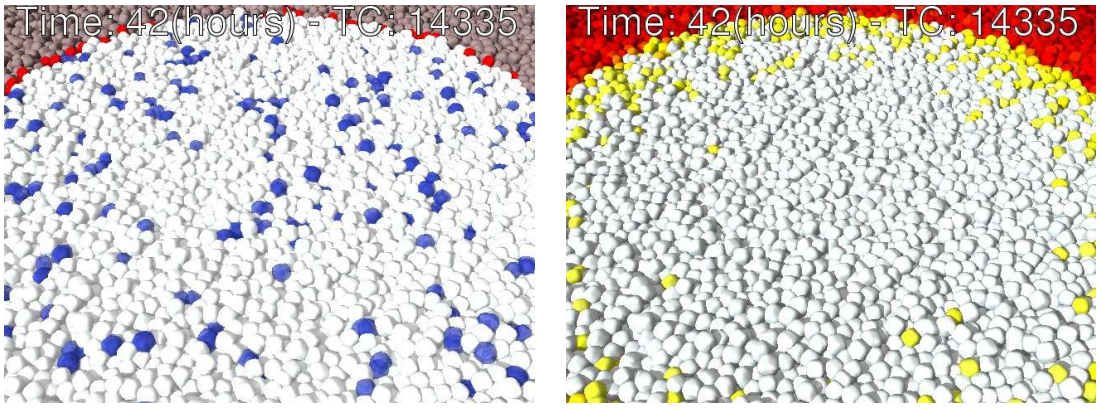

(a) (b)

Figure 3.55: Simulations with 10% killed at the beginning. No detectable difference in tumor pressure can be found after 2 days (compare right picture to figure 3.54(b)).

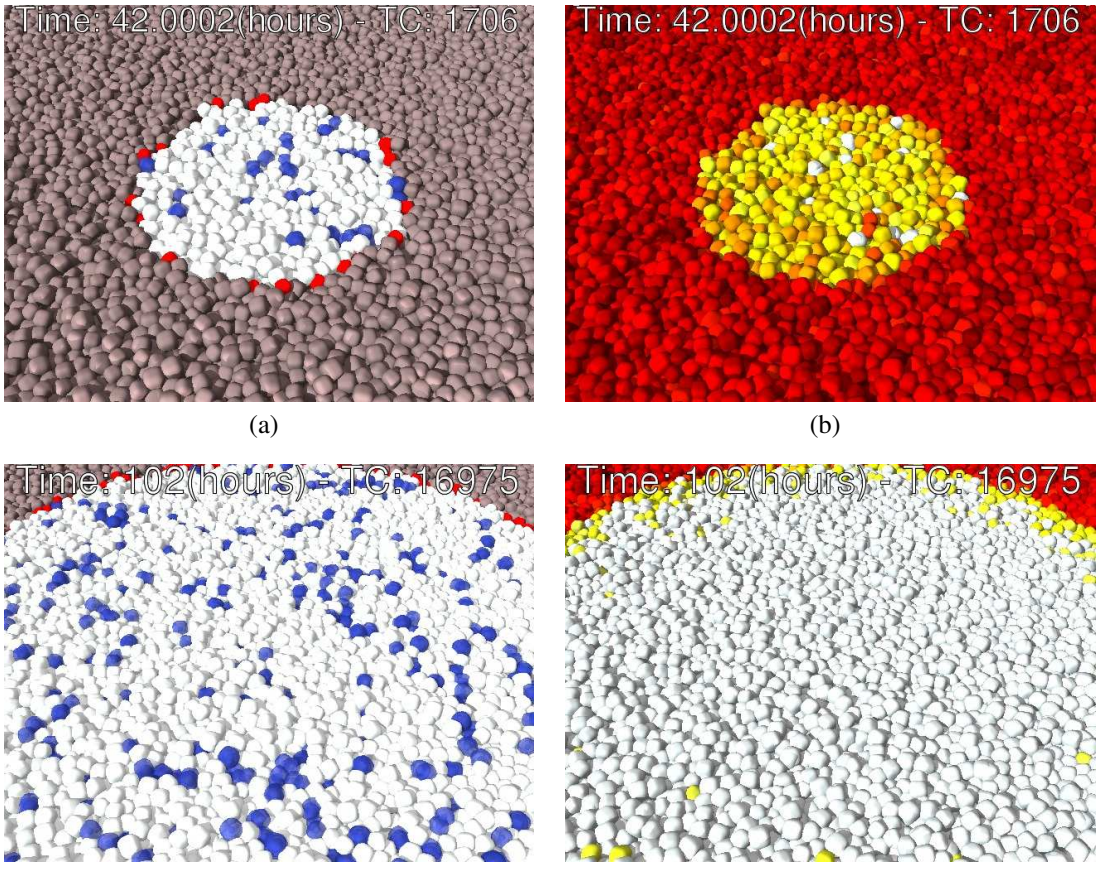

Figure 3.56: Simulations with 90% killed (2 time points). After 2 days the pressure is much lower than for the insensitive (0% cell kill) and low sensitive (10%) cell kill tumor. However, after 4 days the pressure profile becomes indistinguishable from the low sensitive tumor at day 2 (compare figure 3.55(b)).

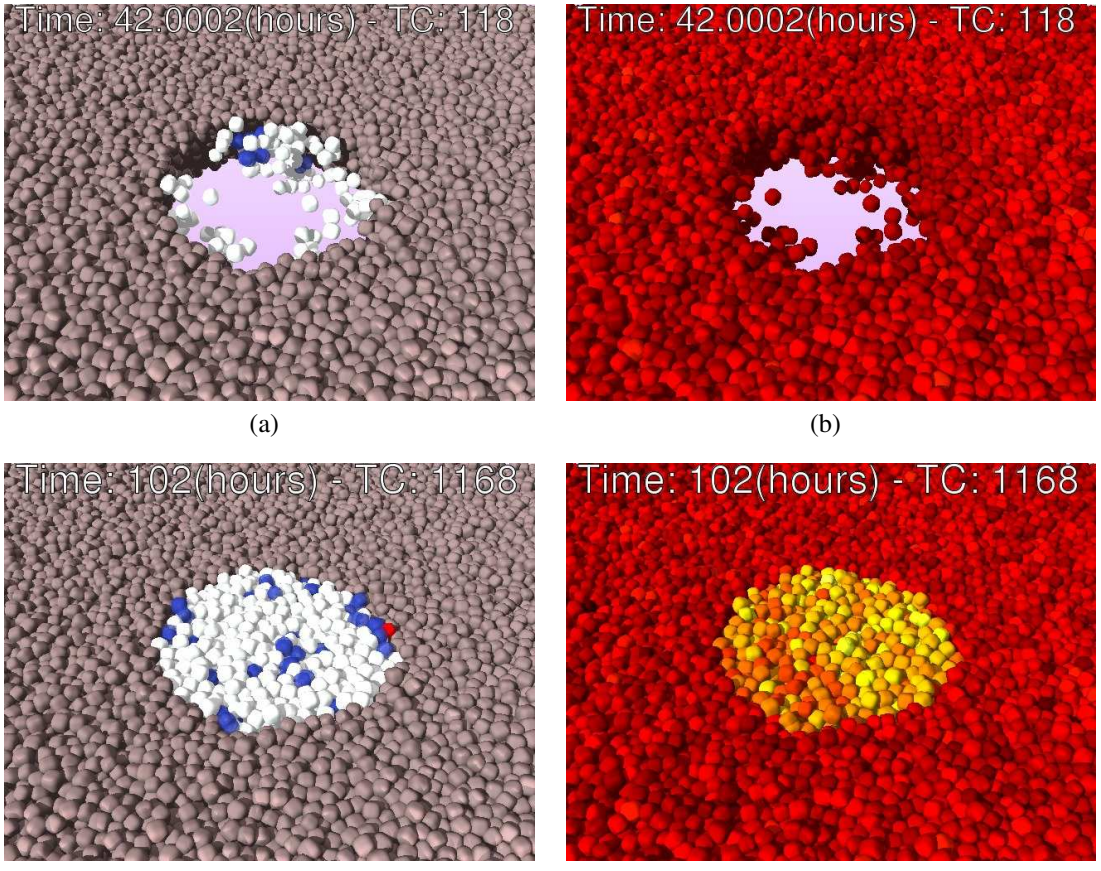

(a) (b)

(c) (d)

Figure 3.57: Simulations with 99% killed at the beginning (2 time points).). After 2 days and even after 4 day the pressure is much lower than for the insensitive (0% cell kill) and low sensitive (10%) cell kill tumor (compare figure 3.56(b)). Nevertheless the tumor regrows to a compact solid tumor.

Conclusion:
In the simulation results presented above, most parameters have only a modest influence on either tumor growth kinetics or phenotype. However, building on precise exploration of simulated tumor phenotypes, we could exclude some that were originally thought as good candidates and understand better the mechanisms needed to reproduce experimental data. We could show that the effect of proteolytic enzyme in the liver, the cell motility, the cell mechanical softness, the endothelial cell proliferation, the healthy cell death and the cell rates are negligible in physiological range in multi-lobule environment. We could also show the consistency of the model for pressure threshold and for large tumors. For this study, we introduced new measures like endothelial cell densities in tumors, endothelial cells in contact with tumor cells, etc. These new measures permitted to find quantitative differences between tumor cell phenotypes. Finally, we performed a first step towards simulating the impact of a drug therapy and we present the first results in an environment consisting only of hepatocytes.

Chapter 4

Summary and other applications

4.1 Summary

The model that we developed and presented in this thesis takes place in the realm of systems biology research, a relatively recent domain of science that works on different scales. It approaches problems like in experimental sciences does, but in contrast to which the experiments are conducted in computer software. In many contexts and especially in biology, agent-based models are good candidates for this type of modeling. They provide a direct approach in which all individual information is immediately available. We implemented and adapted an agent-based model, validated *in vitro* and *in vitro* [43, 41], to apply it to the study of liver tumor. In this model, cells are represented as dumb-bell and each element follows this equation of motion that takes into account the mechanical properties of the elements:

$$(6\pi\eta_0 r_i)\left(\frac{A_i^{cs}}{A_i}\underline{v}_i + \frac{a_i}{2}\hat{\underline{a}}_i \times (\underline{F}_i^{(1)} - \underline{F}_i^{(2)})\right) + \sum_j \underline{\underline{\Gamma}}_{cc}\frac{A_{ij}}{A_i}(\underline{v}_i^{ij} - \underline{v}_j^{ij}) = \sum_j \underline{F}_{jkr}^{ij} + \underline{F}_i^{\text{active}} \quad (4.1)$$

Model simulations are very demanding. They imply a large number of elements and ask for numerical accuracy and rigorous conditions. A large part of the work has been necessarily invested in implementation and optimization. Efficient algorithms have been created to work with recent techniques of parallelization and provide software able to solve rigorously the large system of equations. We managed to create the first liver model able to analyze multiple cancer phenotypes in 3D in a multi-lobule environment. Moreover, the implementation is generic. It makes the code easily adaptable to other applications. Today the software is already applied to close models.

The spatial arrangement of liver constituents ensures that the liver functionality is optimized. Modifications in liver architecture decrease performance of the organ. Liver function is guaranteed by different cell types and their complex organization. Cancer introduces perturbations leading to disorder in the tissue. To explain this disorder the mathematical model was enhanced to reflect liver architecture and how architecture emerges

from the interplay of physical forces between the liver constituents (polarity, tight-junctions, vessel stiffness,...). We based our work on data from [15] where the authors demonstrated that (*i*) *APC* is functional in the liver and (*ii*) aberrant β-Catenin signalling is a genetic event able to initiate the development of HCC. In the case of a high dose of *AdCre* injection, they showed a threshold effect of *APC* depletion in liver (70%) to trigger hepatocyte proliferation. In the case of diluted dose injection, they produced and analyzed different HCC phenotypes (well and poorly differentiated). We adapted the mathematical model to take into account this biological information and suggest explanations to these experimental results. During the research process, we iterated with our partners to identify the plausible mechanisms. We finally established step by step a reference model and tested the different combinations.

The first results presented have been obtained in monolayer culture. The results show that considering the spatial arrangement of cells instead of only individual cells can make a big difference: hepatocyte proliferation could be explained only with homogeneous concentrations of growth factors. Moreover, information from higher scales can help to identify missing control units or links on the intracellular molecular scale. Both steps studying the impact of cell-level parameters on the tumor phenotype and integrating the intracellular molecular model into each individual cell need to be performed separately. The reason is that not all influences of the intracellular activation patterns on the cell-level parameters are known, so an integrated multi-scale model representing the Wnt/Ras-modules within each cell and coupling them to the known cell parameters proliferation and apoptosis may be insufficient to explain the experimentally observed growth pattern. Indeed, proliferation and apoptosis alone seem insufficient to explain the occurrence and the pattern of the well-differentiated and poorly differentiated tumor phenotypes. Interactions between sinusoidal endothelial cells and tumor cells are likely to be crucial to understand emergence of well and poorly differentiated tumor phenotypes. This could only be found from studying the effect of cell-level parameters on the tumor phenotype independently of the intracellular molecular alphabet. On the other hand knowing the possible cell level parameters capable to explain the experimentally observed phenotypes gives valuable hints to additional functions of Wnt- or Ras- pathway activation effects, or to alternative pathways that may be activated during carcinogenesis.

Simulations performed in liver suggest that the homogeneity of the vessel network depends on the ratio among the vessel stiffness and the velocity and strength of the growth. With the experimental value of 1000 Pascal for the vessel stiffness, a totally uncontrolled proliferation creates vessel depletion within the tumor. To calibrate the model, one needs quantitative data on vessel architecture in well-differentiated tumors and data on the tumor development.

APC depletion in cell has a strong oncogenic effect that affects many aspect of the cells. In particular APC depletion could be a possible cause for the emergence of aggressive tumors able to destroy the lobular vasculature. In this case, SEC death is sufficient to reproduce poorly differentiated tumor phenotypes, whatever are the other mechanisms and parameters of tumor phenotype as well as the molecular origin of the SEC death. In

order to find the proper parameters tumor growth rate and destruction pressure threshold calibration of the model parameters with biological data that are not yet present would be necessary.

Tumor cell phenotypes that could be quantified may disappear at later stage of tumorous development. It is important not to look only at the final stage of the tumor (as experimentalists as well as clinicians usually do) but on the whole development phase. The whole analysis over time of the model permits to distinguish differences in cell phenotypes that end with the same tumor pattern. Before converging to a spherical symmetry, the tumor asymmetry reflects the tumor cell phenotype. Our simulations suggest that HSA is not enough to explain the pattern of initiated cells in [35]. These cells must not be to dedifferentiated and possess at least two hepatocyte mechanisms: HSA and SEC adhesion.

Most parameters have only a modest influence on either tumor growth kinetics or phenotype. However, building on precise exploration of simulated tumor phenotypes, we could exclude some that were originally thought as good candidates and understand better the mechanisms needed to reproduce experimental data. We could show that the effect of proteolytic enzyme in the liver, the cell motility, the cell mechanical softness, the endothelial cell proliferation, the healthy cell death and the cell rates are negligible in physiological range in multi-lobule environment. We could also show the consistency of the model for pressure threshold and for large tumors. For this study, we introduced new measures like endothelial cell densities in tumors, endothelial cells in contact with tumor cells, etc. These new measures permitted to find quantitative differences between tumor cell phenotypes. Finally, we performed a first step towards simulating the impact of a drug therapy and we present the first results in an environment consisting only of hepatocytes.

4.2 Other on-going applications

The model implementation has already been distributed to simulate related problems (cell/tumor growing population). The necessary adaptations are currently made in a collaborative work.

1. **Syne2Arti:** François Bertaux, Szymon Stoma and Gregory Batt (Inria) applied the model in Syne2Arti (Synthetic networks to artificial tissues) ANR project, which aims to develop methods to support the rational design of artificial tissues by combining computational biology and synthetic biology approaches. Cells are engineered such that the expected behavior of the tissue emerges from cell interactions. In particular, focus is made on a tissue homeostasis system: the goal is to design *in silico* and construct in vivo a tissue that autonomously maintains its cell density at a desired level. Here, the software provides a realistic framework for cell growth, division and motion. It also permits to implement easily various intra-cellular models inside each cell, allowing to realize *in silico* experiments (at the "Petri dish" scale) for each set of intra-cellular components that could be added into cells (4.1).

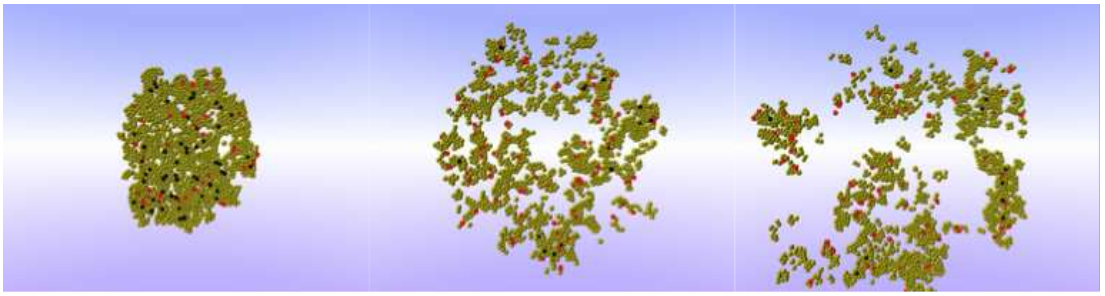

Figure 4.1: Other application of the model and code: a simulation of population evolving in a Petri dish for the Syne2Arti ANR project.

2. **Game of life project:** François Bertaux, Szymon Stoma and Gregory Batt (Inria) in collaboration with a synthetic biology group in MIT, the Weiss lab. Yeast cells has been engineered to play the famous Conway's "game of life" cellular automaton, where cells decide to die when they have either too much or too few neighbors, and divide in-between. Here, cells produce a diffusive molecule that is released in the medium, permitting to create concentration gradients related to the spatial configuration of cells. This molecule binds to receptors at each cell surface and induces death pathways when binding is either too high or too low. The software is used in combination with image analysis procedures to guide experiments and help the tuning of the system. More precisely, it is first calibrated to reproduce growth of the yeast strain constructed where "killing" and "communication" modules are off. In a second step, experiments involving those two modules are conducted, and obtained results allow characterizing their model parameters using *in silico* computations of identical experiments (4.2).

3. Ibrahim Cheddadi is currently building a continuous model of cell aggregates that is compared to the ABM model presented here. The comparison focuses on the mechanical properties of both models; the purpose is to suggest hybrid model to combine the advantages of both approaches.

4. Annabelle Ballesta and François Bertaux started a collaboration to produce tumor spheroid and understand the results of [48].

5. Chadha Chettaoui used the model to model the trophoblast formation in bovine.

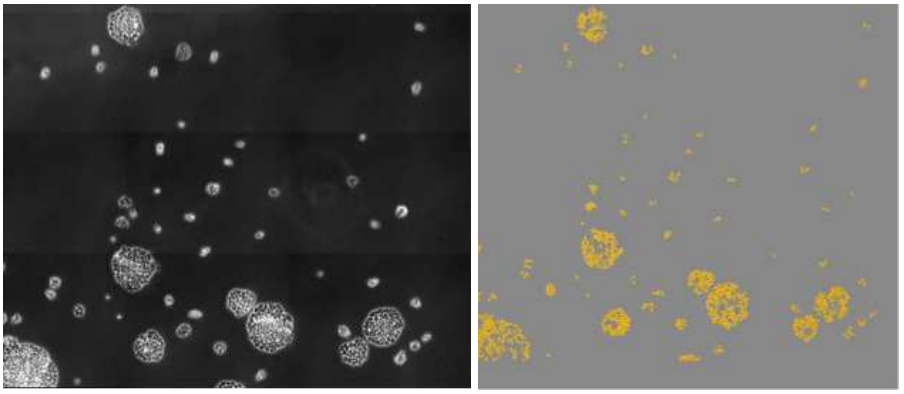

Figure 4.2: *in silico* seeding of cells according to experimental data

Chapter 5

Appendix

5.1 Collaborations

- System toxicology group at Ifado. Responsible: Pr. Jan Hengstler. Address: Leibniz-Institut für Arbeitsforschung an der TU Dortmund Ardeystr. 67 D - 44139 Dortmund. email: hengstler@ifado.de, webpage: www.ifado.de
- INSERM U1016, CNRS UMR 8104, Université Paris Descartes at Institut Cochin, Department of Endocrinology, Metabolism and Cancer, Team : Oncogenesis of digestive epithelia. Address:24, rue du fbg St Jacques 75014 PARIS. Sabine Colnot email: sabine.colnot@inserm.fr
- Group of Systems Biology of Molecular Networks, in Laboratory of Molecular Tumor Pathology (Charité) and the Institute of Theoretical Biology (HU Berlin). Address: Charite - Universitätsmedizin Berlin Institut für Pathologie Chariteplatz 1D 10117 Berlin. webpage: sys-bio.net. Nils Blüthgen. email: nils@sys-bio.net
- Izbi, Group: Multicellular systems biology. Address: Interdisciplinary Center for Bioinformatics University of Leipzig Härtelstr. 16-18 D-04107 Leipzig Germany. webpage: www.msysbio.com. Stefan Höhme, email: hoehme@izbi.uni-leipzig.de
- INRIA Address: Domaine de Voluceau BP 105 78153 ROCQUENCOURT FRANCE. Team BANG. webpage: www.inria.fr. Collaborative Members: Dirk Drasdo, Nick Jagiella, Chadha Chettaoui, François Bertaux, Ibrahim Cheddadi, Annabelle Ballesta.

5.2 Parameters and model options

5.3 switches

The simulator takes as an input a set of switches that defines the model assumptions. The list below shows the possible combination of assumptions. Most of them can be selected independently from the others.

Name in the simulator	Model assumption
__X_PERIODIC	Set the domain periodic in X direction
__Y_PERIODIC	Set the domain periodic in Y direction
__Z_PERIODIC	Set the domain periodic in Y direction
__POLAR_ADHESION	Modulate the force with the polarity of the cells
__PRESSURE_GRADIENT	Pressure gradient for the preferred random move
__ONLY_REPULSION	Take only the repulsive pressure into account in the pressure computation
__KEEP_BONDS_FORCE	Tumor cell does not destroy adhesion among healthy hepatocytes
__DESTROY_BONDS_FORCE	Tumor cell does destroy adhesion among healthy hepatocytes when touches one
__TUMOR_SEC_ADHESION_FORCE	Model of adhesion between tumor cells and SEC
__TUMOR_ADHESION	Define if the tumor cell is adhesive or not to other cells
__BENDING_FORCE	Tissue property of the trophoblast to make it grow as a sphere
__CONTACT_INHIBITION	Define a contact inhibition rule for cell division in Bax* model
__SEC_STRETCH_GROWTH	Endothelial cells can proliferate when they are too stretched
__SEC_LENGTH_GROWTH	Endothelial links grow if they are in contact with tumor cell and divide when they are too stretched
__ENDOTHELIAL_DEATH	Endothelial cells can die due to pressure
__MORPHOGEN_ATTRACTION	Add a morphogen attraction between SEC and Cell0
__TUMOR_MORPHOGEN_ATTRACTION_ONLY	Restrict morphogen attraction to tumor cells only
__DIVISION_DIRECTION_RANDOM	Align cells division randomly
__SINUSOID_DIVISION_DIRECTION	Align cells with the closest sinusoid at birth (else random)

__DIVISION_DIRECTION_NEIGHBOR	Align cells with the closest at birth (else random)
__DIVISION_POLARITY_DIRECTION	Divide in the mother cell polarity direction (no random)
__CELL_CELL_DIFFUSION	Compute diffusion of Wnt and GF from cell to cell
__MEDIUM_DIFFUSION	Add free diffusion of a messenger in the medium
__SUB_SUB_FRICTION	Compute friction between sub-element
__EXACT_SOLUTION	Define a matrix, a Cholesky factorization of the matrix and a copy of the solution.
__ITERATIVE_SOLUTION	Use the speed of the last iteration and make iterations
__MOVE_ONLY_CELLS	Move only cells in liver model where there exists other types. For some tests: should be off always and removed
__SET_ZDIRECTION_ZERO	An easy way to get monolayer: put everything in z coordinate to 0.
__SET_YDIRECTION_ZERO	An easy way to get monolayer (if combined with z = 0, 1D model for mechanical analysis): put everything in y coordinate to 0.

5.4 parameters

index	Name	value	unit
hepatocyteInitialDiameter	23.3	micrometer	[42]
centralVeinInitialDiameter	42	micrometer	[42]
sinusoidInitialDiameter	7.0832	micrometer	[42]
medium_viscosity_bio	1000	$N \cdot s \cdot m^{-2}$	[24]
single_bond_energy_bio	1.10^{-19}	Newton	[8]
diffusion_constant_cells_bio	1.10^{-16}	$m^2 \cdot s^{-1}$	[23]
cell_cell_adhesion_density_bio	1e+15	m^{-2}	[13]
cycletime_bio	57600	second	–
mitosistime_bio	7200	second	–
cycletime_variance_bio	7200	second	–
youngModuleBioHepatocyte	450	$N \cdot m^{-2}$	[59]
poissonRatio	0.4	no dimension	[3]
hepatocyteDistanceAfterDivision	18.64	micrometer	–
springConstantSinusoids	1000	Pascal	[9]
cell_cell_friction_bio	3.10^{07}	$N \cdot s \cdot m^{-3}$	[24]
cell_sinusoid_friction_bio	3.10^{07}	$N \cdot s \cdot m^{-3}$	–
youngModuleBioSinusoid	600	$N \cdot m^{-2}$	–
youngModuleBioVein	1000	$N \cdot m^{-2}$	–
pressureHepatocytesToQuiescence	-500	Pascal	–
pressureHepatocytesToDie	200	Pascal	–
pressureTumorToQuiescence	3000	Pascal	–
pressureTumorToDie	300000	Pascal	–
lysisBioTime	7200	second	–
apoptosisBioTime	1800	second	–
apoptosisVarianceBioTime	3600	second	–
sphaseBioDuration	14400	second	–
morphogenAttractionRange	1.5	Cell diameter	–
morphogenAttractionStrength	50	Newton	–
pressureEndothelialCellToDie	200	Pascal	–
probaCycleEntrance	1	no dimension	–
xliverSize	1.74983	millimeter	–
yliverSize	1.71954	millimeter	–
zliverSize	0.163333	millimeter	–

List of Figures

List of Tables

List of Algorithms

Glossary

β-Catenin β-Catenin is a protein that plays a role in various aspects. It acts on adhesion : cell junction, contact inhibition; it is involved in liver biology including liver development liver regeneration following partial hepatectomy, HGF-induced hepatomegaly, liver zonation, and pathogenesis of liver cancer; especially, it is involved in the Wnt STP [76, 83]. 52, 57, 59, 69, 72, 73, 75, 76, 82, 96, 132, 141

DAPI DAPI is a fluorescent stain that binds strongly to DNA. It is used extensively in fluorescence microscopy. Since DAPI will pass through an intact cell membrane, it may be used to stain both live and fixed cells. For fluorescence microscopy, DAPI is excited with ultraviolet light. When bound to double-stranded DNA its absorption maximum is at 358 nm and its emission maximum is at 461 nm. (This emission is fairly broad, and appears blue/cyan.) DAPI will also bind to RNA, though it is not as strongly fluorescent. Its emission shifts to around 500 nm when bound to RNA. DAPI's blue emission is convenient for microscopists who wish to use multiple fluorescent stains in a single sample. Apart from labeling cell nuclei, the most popular application of DAPI is in detection of mycoplasma or virus DNA in cell cultures . 60

DPPIV Dipeptidyl peptidase-4 (DPP4), also known as adenosine deaminase complexing protein 2 (ADA) or CD26 (cluster of differentiation 26) is a protein that, in humans, is encoded by the DPP4 gene. The protein encoded by the DPP4 gene is an antigenic enzyme expressed on the surface of most cell types and is associated with immune regulation, signal transduction and apoptosis. It is an intrinsic membrane glycoprotein and a serine exopeptidase that cleaves X-proline dipeptides from the N-terminus of polypeptides. Furthermore, it appears to work as a suppressor in the development of cancer and tumors. CD26/DPPIV plays an important role in tumor biology, and is useful as a marker for various cancers, with its levels either on the cell surface or in the serum increased in some neoplasms and decreased in others . 59, 60, 96, 97

ICAM-1 (Inter-Cellular Adhesion Molecule 1) also known as CD54 (Cluster of Differentiation 54) is a human gene. The protein encoded by this gene is a type of intercellular adhesion molecule continuously present in low concentrations in the membranes of leukocytes and endothelial cells. 59, 60

APC Adenomatous polyposis coli(APC) is a protein that in humans is encoded by the APC gene. APC is classified as a tumor suppressor gene. Tumor suppressor genes prevent the uncontrolled growth of cells that may result in cancerous tumors. The APC protein helps control how often a cell divides, how it attaches to other cells within a tissue, or whether a cell moves within or away from a tissue. This protein also helps ensure that the chromosome number in cells produced through cell division is correct. The APC protein accomplishes these tasks mainly through association with other proteins, especially those that are involved in cell attachment and signaling. The activity of one protein in particular, β-Catenin, is controlled by the APC protein. 4, 5, 15, 16, 57, 59, 95, 98, 132

AdCre Cre Recombinase Adenovirus (AdCre) recombines a pair of short target sequences called the Lox sequences. This system can be implemented without inserting any extra supporting proteins or sequences. The Cre enzyme and the original Lox site called the LoxP sequence are derived from a bacteriophage P1. It is widely used to carry out deletions, insertions, translocations and inversions in the DNA of cells. It allows the DNA modification to be targeted to a specific cell type or be triggered by a specific external stimulus. 57–60, 96, 132

Apc Knock-out Cell where APC gene has been removed and cannot encode APC proteins. 75, 84, 85, 96, 148

in silico is an expression used to mean "performed on computer or via computer simulation". The phrase was coined as an analogy to the Latin phrases *in vivo*, *in vitro*, and *in situ*, which are commonly used in biology. 11, 16, 51, 52, 63, 133–135

in vitro (Latin: within glass) Refers to studies in experimental biology that are conducted using components of an organism that have been isolated from their usual biological context in order to permit a more detailed or more convenient analysis than can be done with whole organisms. Colloquially, these experiments are commonly referred to as "test tube experiments". 63, 131

in vivo Latin for "within the living") is experimentation using a whole, living organism as opposed to a partial or dead organism. Animal testing and clinical trials are two forms of in vivo research. In vivo testing is often employed over in vitro because it is better suited for observing the overall effects of an experiment on a living subject. This is often described by the maxim *in vivo veritas*. 63

ABM Agent-Based Model. 15, 134

Apc$^{-/-}$ We denote by this symbol, the APC depleted cells (see *Apc Knock-out*. 16, 59, 69, 75, 89

Apc$^{lox/lox}$ We denote by this symbol, the cells where APC can be potentially removed after tamoxifen injection. 16, 69, 70

ARC Association pour la recherche contre le cancer. 52

BFA Biomechanical force for apoptosis. 66, 107

BFI Biomechanical force for inhibition. 66, 92, 107

chemoattractant Chemical substance that induces chemoattraction. 29

chemoattraction The movement of a cell in response to a chemical stimulant, the chemoattractant. 29, 67, 149

CSC Compressed Storage Column. 43

CSR Compressed Storage Row. 43

G+ placental glutathione S-transferase-positive. 101

GF stands for growth factor. A growth factor is a naturally occurring substance capable of stimulating cellular growth, proliferation and cellular differentiation. Usually it is a protein or a steroid hormone. Growth factors are important for regulating a variety of cellular processes. Growth factors typically act as signaling molecules between cells. 29

GST-P placental glutathione S-transferase. 101

HCC Hepatocellular carcinoma. 52, 57, 59, 69, 100, 132

hepatocyte Hepatocyte is the main cell type in liver, see Section 3.1.2. 53

HSA Hepatocyte sinusoid alignment. 66, 91, 92, 98, 100, 102–105, 133

IARC international agency for research on cancer. 52

IfADo Leibniz-Institut für Arbeitsforschung an der TU Dortmund. 59, 61, 62

INSERM Institut national de la santé et de la recherche médical. 57

JKR Johnson-Kendall-Roberts. 39

morphogen A substance governing the pattern of tissue development, and the positions of the various specialized cell types within a tissue. It spreads from a localized source and forms a concentration gradient across a developing tissue. 29, 67

NNM N-nitrosomorpholine. 101

Ras is the name given to a family of related proteins. All Ras protein family members belong to a class of protein called small GTPase, and are involved in transmitting signals within cells. Ras is the prototypical member of the Ras superfamily of proteins, which are all related in 3D structure and regulate diverse cell behaviors. Because these signals result in cell growth and division, overactive Ras signaling can ultimately lead to cancer. Ras is the most common oncogene in human cancer - mutations that permanently activate Ras are found in 20-25% of all human tumors and up to 90% in certain types of cancer (e.g. pancreatic cancer). For this reason, Ras inhibitors are being studied as a treatment for cancer, and other diseases with Ras overexpression. 4, 5, 69, 70

SEC sinusoidal endothelial cell. 53, 55, 60, 67, 68, 90, 91, 98, 103, 105, 111, 133

STP signaling transduction pathway. 52, 69, 70, 147

TGF-α Transforming growth factor alpha (TGF-*alpha*) is upregulated in some human cancers. It induces epithelial development. It is closely related to EGF, and can also bind to the EGF receptor with similar effects.. 72, 83, 84

Wnt The Wnt proteins are a group of secreted lipid-modified. These proteins activate various pathways in the cell that can be categorized into the canonical and non-canonical Wnt pathways. Through these signaling pathways, Wnt proteins play a variety of important roles in embryonic development, cell differentiation, and cell polarity generation [60]. The Wnt signaling pathway is a network of proteins best known for their roles in embryogenesis and cancer, but also involved in normal physiological processes in adult animals. 4, 5, 29, 52, 69, 70, 147

Bibliography

[1] Braeuning A. and Schwarz M. Zonation of heme synthesis enzymes in mouse liver and their regulation by β-catenin and ha-ras. *Biological Chemistry*, 391(11):1305, 2010.

[2] T. Alarcon, H.M. Byrne, and P.K. Maini. A mathematical model of the effects of hypoxia on the cell-cycle of normal and cancer cells. *J. Theor. Biol.*, 229:395 – 411, 2004.

[3] J. Alcaraz, L. Buscemi, M. Grabulosa, X. Trepat, B. Fabry, R. Farre, and D. Navajas. Microrheology of human lung epithelial cells measured by atomic force. *Biophys. J.*, 84:2071–2079, 2003.

[4] A.R.A. Anderson and M.A.J. Chaplain. Continuous and discrete mathematical models of tumour-induced angiogenesis. *Bull. Math. Biol.*, 60:857–899, 1998.

[5] John D. Barrow. *The constants of nature*. Jonathan Cape Ltd, 2002.

[6] E. Barthel. Adhesive elastic contacts: Jkr and more. *Journal of Physics D: Applied Physics*, 41(16):163001, 2008.

[7] Markus Basan, Thomas Risler, Jean-François Joanny, Xavier Sastre-Garau, and Jacques Prost. Homeostatic competition drives tumor growth and metastasis nucleation. *HFSP J*, 3(4):265–272, Aug 2009.

[8] D. Beysens, G. Forgacs, and J.A. Glazier. Cell sorting is analogous to phase ordering in fluids. *Proc. Natl. Acad. Sci. USA*, 97(17):9467 – 9471, 2000.

[9] F. Braet, C. Rotsch, E. Wisse, and M. Radmacher. Comparison of fixed and living liver endothelial cells by atomic force microscopy. *Applied Physics a-Materials Science & Processing*, 66:S575–S578, 1998. Times Cited: 47.

[10] J. Castelneau. Zero user equal zero bug, software engineering. private communication, 2010.

[11] Philippe Chafey, Laetitia Finzi, Raphael Boisgard, Michèle Caüzac, Guillem Clary, Cédric Broussard, Jean-Paul Pégorier, François Guillonneau, Patrick Mayeux, Luc Camoin, Bertrand Tavitian, Sabine Colnot, and Christine Perret. Proteomic analysis

of β-catenin activation in mouse liver by dige analysis identifies glucose metabolism as a new target of the wnt pathway. *PROTEOMICS*, 9(15):3889–3900, 2009.

[12] H. Chaté. Emergence of Collective Behavior in Large Chaotic Dynamical Systems. *International Journal of Modern Physics B*, 12:299–308, 1998.

[13] S.E. Chesla, P. Selvaraj, and C. Zhu. Measuring two-dimensional receptor-ligand binding kinetics by micropipette. *Biophys. J.*, 75:1553–1557, 1998.

[14] Y. S. Chu, S. Dufour, J. P. Thiery, E. Perez, and F. Pincet. Johnson-kendall-roberts theory applied to living cells. *Physical Review Letters*, 94(2), 2005. Times Cited: 30.

[15] S. Colnot, T. Decaens, M. Niwa-Kawakita, C. Godard, G. Hamard, A. Kahn, M. Giovannini, and C. Perret. Liver-targeted disruption of apc in mice activates beta-catenin signaling and leads to hepatocellular carcinomas. *Proceedings of the National Academy of Sciences of the United States of America*, 101(49):17216–17221, 2004. Times Cited: 86.

[16] Alix de La Coste, Béatrice Romagnolo, Pierre Billuart, Claire-Angélique Renard, Marie-Annick Buendia, Olivier Soubrane, Monique Fabre, Jamel Chelly, Cherif Beldjord, Axel Kahn, and Christine Perret. Somatic mutations of the β-catenin gene are frequent in mouse and human hepatocellular carcinomas. *Proceedings of the National Academy of Sciences*, 95(15):8847–8851, 1998.

[17] J.C. Dallon and H.G. Othmer. How cellular movement determines the collective force generated by the dictyostelium discoideum slug. *J. theor. Biol.*, 231:203–222, 2004.

[18] J.K.G. Dhont. *An Introduction to Dynamics of Colloids*. Elsevier, Amsterdam, 1996.

[19] Bi-Sen Ding, Daniel J. Nolan, Jason M. Butler, Daylon James, Alexander O. Babazadeh, Zev Rosenwaks, Vivek Mittal, Hideki Kobayashi, Koji Shido, David Lyden, Thomas N. Sato, Sina Y. Rabbany, and Shahin Rafii. Inductive angiocrine signals from sinusoidal endothelium are required for liver regeneration. *Nature*, 468(7321):310–315, Nov 2010.

[20] D. Drasdo. On selected individual-based approaches to the dynamics in multicellular systems. In W. Alt, M. Chaplain, M. Griebel, and J. Lenz, editors, *Multiscale Modelling and Numerical Simulations*, pages 169–203. Birkhäuser, 2003.

[21] D. Drasdo. Coarse graining in simulated cell populations. *Adv. Complex Syst.*, 8(2-3):319–363, 2005.

[22] D. Drasdo, S. Hoehme, and M. Block. On the role of physics in the growth and pattern formation of multi-cellular systems: What can we learn from individual-cell based models? *J. Stat. Phys*, 128:287–345, 2007.

[23] Dirk Drasdo and Stefan Hoehme. A single-cell-based model of tumor growth in vitro: monolayers and spheroids. *Phys Biol*, 2(3):133–147, Sep 2005.

[24] J. Galle, G. Aust, G. Schaller, T. Beyer, and D. Drasdo. Single-cell based mathematical models to the spatio-temporal pattern formation in multi-cellular systems. *Cytometry Teil A*, pages 704–710, 2006.

[25] J. Galle, M. Hoffmann, and G. Aust. From single cells to tissue architecture-a bottom-up approach to modelling the spatio-temporal organisation of complex multi-cellular systems. *J Math Biol*, 58(1-2):261–283, Jan 2009.

[26] Erich Gamma, Richard Helm, Ralph Johnson, and John Vlissides. *Design patterns: elements of reusable object-oriented software*. Addison-Wesley Longman Publishing Co., Inc., Boston, MA, USA, 1995.

[27] R. A. Gatenby and P. K. Maini. Mathematical oncology: Cancer summed up. *Nature*, 421:321, 2003.

[28] Robert A. Gatenby. A change of strategy in the war on cancer. *Nature*, 459(7246):508–509, 05 2009.

[29] Robert A. Gatenby and Edward T. Gawlinski. The glycolytic phenotype in carcinogenesis and tumor invasion. *Cancer Research*, 63(14):3847–3854, 2003.

[30] Rachel H. Giles, Johan H. van Es, and Hans Clevers. Caught up in a wnt storm: Wnt signaling in cancer. *Biochimica et Biophysica Acta (BBA) - Reviews on Cancer*, 1653(1):1 – 24, 2003.

[31] Ralf Gödde and Haymo Kurz. Structural and biophysical simulation of angiogenesis and vascular remodeling. *Developmental Dynamics*, 220(4):387–401, 2001.

[32] Gene H. Golub and Charles F. Van Loan. *Matrix computations (3rd ed.)*. Johns Hopkins University Press, Baltimore, MD, USA, 1996.

[33] Carl A. Goresky. A linear method for determining liver sinusoidal and extravascular volumes. *American Journal of Physiology – Legacy Content*, 204(4):626–640, 1963.

[34] François Graner and James A. Glazier. Simulation of biological cell sorting using a two-dimensional extended potts model. *Phys. Rev. Lett.*, 69:2013–2016, Sep 1992.

[35] Bettina Grasl-Kraupp, Georg Luebeck, Alexandra Wagner, Alexandra Löw-Baselli, Mathisca de Gunst, Thomas Waldhör, Suresh Moolgavkar, and Rolf Schulte-Hermann. Quantitative analysis of tumor initiation in rat liver: role of cell replication and cell death (apoptosis). *Carcinogenesis*, 21(7):1411–1421, 2000.

[36] Mel Greaves and Carlo C. Maley. Clonal evolution in cancer. *Nature*, 481(7381):306–313, 01 2012.

[37] Jean Gruenberg and Harald Stenmark. The biogenesis of multivesicular endosomes. *Nat Rev Mol Cell Biol*, 5(4):317–323, 04 2004.

[38] D. Hanahan and R. A. Weinberg. Hallmarks of cancer: The next generation. *Cell*, 144(5):646–674, 2011. Times Cited: 64.

[39] Hans and Clevers. Wnt/*beta*-catenin signaling in development and disease. *Cell*, 127(3):469 – 480, 2006.

[40] G. Helmlinger, P.A. Netti, H.C. Lichtenfeld, R.J. Melder, and R.K. Jain. Solid stress inhibits the growth of multicellular tumor spheroids. *Nat Biotech*, 15(8):778–783, 1997.

[41] S. Hoehme and D. Drasdo. Biomechanical versus nutrient control: what determines the growth dynamics of mammalian cell populations ? *Mathematical Population Studies.*, 2009.

[42] S. Hoehme, J.G. Hengstler, M. Brulport, M. Schäfer, A. Bauer, R. Gebhardt, and D. Drasdo. Mathematical modelling of liver regeneration after intoxication with ccl4. *Chem Biol Interact*, 168(1):74–93, 2007.

[43] Stefan Hoehme, Marc Brulport, Alexander Bauer, Essam Bedawy, Wiebke Schormann, Matthias Hermes, Verena Puppe, Rolf Gebhardt, Sebastian Zellmer, Michael Schwarz, Ernesto Bockamp, Tobias Timmel, Jan G. Hengstler, and Dirk Drasdo. Prediction and validation of cell alignment along microvessels as order principle to restore tissue architecture in liver regeneration. *Proceedings of the National Academy of Sciences of the United States of America*, 107(23):10371–10376, 2010. Times Cited: 5.

[44] Stefan Hoehme and Dirk Drasdo. A cell-based simulation software for multi-cellular systems. *Bioinformatics*, 26(20):2641–2642, 2010. Times Cited: 1.

[45] S. Huang and D.E. Ingber. The structural and mechanical complexity of cell-growth control. *Nature Cell Biol.*, 1:E131–E138, 1999.

[46] James Boyer Irwin M. Arias, Harvey J. Alter. *The liver: biology and pathobiology*. Wiley-Blackwell, 2009.

[47] Yousef Jamali, Mohammad Azimi, and Mohammad R. K. Mofrad. A sub-cellular viscoelastic model for cell population mechanics. *PLoS ONE*, 5:e12097, 08 2010.

[48] Eui Kyong Jeong, Su Yeon Lee, Hyun Min Jeon, Min Kyung Ju, and Ho Sung Kang Cho Hee Kim. Role of extracellular signal-regulated kinase (erk)1/2 in multicellular resistance to docetaxel in mcf-7 cells. *International Journal of Oncology*, 37(3):655–661, 2010.

[49] K.L. Johnson, K. Kendall, and A.D. Roberts. Surface energy and the contact of elastic solids. *Proc. Roc. Soc. A*, 324:301 – 313, 1971.

[50] Gareth Wyn Jones and S. Jonathan Chapman. Modeling growth in biological materials. *SIAM Review*, 54(1):52–118, 2012.

[51] Parag Katira, Muhammad H. Zaman, and Roger T. Bonnecaze. How changes in cell mechanical properties induce cancerous behavior. *Phys. Rev. Lett.*, 108:028103, Jan 2012.

[52] Szymon M. Kiełbasa, Holger Klein, Helge G. Roider, Martin Vingron, and Nils Blüthgen. Transfind–predicting transcriptional regulators for gene sets. *Nucleic Acids Research*, 38(suppl 2):W275–W280, 2010.

[53] H. Kitano. Computational systems biology. *Nature*, 420(6912):206–210, 2002. Times Cited: 531.

[54] Ulrike Korf, Sophia Derdak, Achim Tresch, Frauke Henjes, Sabrina Schumacher, Christian Schmidt, Bettina Hahn, Wolf D. Lehmann, Annemarie Poustka, Tim Beissbarth, and Ursula Klingmüller. Quantitative protein microarrays for time-resolved measurements of protein phosphorylation. *PROTEOMICS*, 8(21):4603–4612, 2008.

[55] A. Krinner. *Spherical individual cell-based model*. PhD thesis, Universität Leipzig, 2010.

[56] D. Landau. *Theory of Elasticity*. Pergamon, 1975.

[57] C. Le Bris. *Systèmes multiéchelles: modélisation et simulation*, volume 47 of *Mathématiques et Applications*. Springer, 2005.

[58] D. S. Lee, H. Rieger, and K. Bartha. Flow correlated percolation during vascular remodeling in growing tumors. *Physical Review Letters*, 96(5), 2006. Times Cited: 21.

[59] M. Lekka, P. Laidler, D. Gil, J. Lekki, Z. Stachura, and A.Z. Hrynkiewicz. Elasticity of normal and cancerous human bladder cells studied by scanning force microscopy. *European Biophysics Journal*, 28(4):312–316, 1999.

[60] Catriona Y. Logan and Roel Nusse. The wnt signaling pathway in development and disease. *Annual Review of Cell and Developmental Biology*, 20(1):781–810, 2004.

[61] Paul Macklin, Steven McDougall, Alexander R. A. Anderson, Mark A. J. Chaplain, Vittorio Cristini, and John Lowengrub. Multiscale modelling and nonlinear simulation of vascular tumour growth. *Journal of Mathematical Biology*, 58(4-5):765–798, 2009. Times Cited: 54.

[62] Marie and Annick Buendia. Genetics of hepatocellular carcinoma. *Seminars in Cancer Biology*, 10(3):185 – 200, 2000.

[63] S. R. McDougall, A. R. A. Anderson, M. A. J. Chaplain, and J. A. Sherratt. Mathematical modelling of flow through vascular networks: Implications for ibmour-induced angiogenesis and chemotherapy strategies. *Bulletin of Mathematical Biology*, 64(4):673–702, 2002. Times Cited: 113.

[64] Patrick Mehlen, Céline Delloye-Bourgeois, and Alain Chédotal. Novel roles for slits and netrins: axon guidance cues as anticancer targets? *Nat Rev Cancer*, 11(3):188–197, 03 2011.

[65] A. Munjiza and K. R. F. Andrews. Nbs contact detection algorithm for bodies of similar size. *International Journal for Numerical Methods in Engineering*, 43(1):131–149, 1998. Times Cited: 55.

[66] A. Munjiza, E. Rougier, and N. W. M. John. Mr linear contact detection algorithm. *International Journal for Numerical Methods in Engineering*, 66(1):46–71, 2006. Times Cited: 6.

[67] Denis Noble. Claude bernard, the first systems biologist, and the future of physiology. *Experimental Physiology*, 93(1):16–26, 2008.

[68] M. R. Owen, T. Alarcón, P. K. Maini, and H. M. Byrne. Angiogenesis and vascular remodelling in normal and cancerous tissues. *J Math Biol*, 58(4-5):689–721, 2009.

[69] Jignesh R. Parikh, Bertram Klinger, Yu Xia, Jarrod A. Marto, and Nils Blüthgen. Discovering causal signaling pathways through gene-expression patterns. *Nucleic Acids Research*, 38(suppl 2):W109–W117, 2010.

[70] A. Quarteroni, R. Sacco, and F. Saleri. *Méthodes numériques: algorithmes, analyse et applications*. Springer, 2007.

[71] Ignacio Ramis-Conde, Mark A J Chaplain, Alexander R A Anderson, and Dirk Drasdo. Multi-scale modelling of cancer cell intravasation: the role of cadherins in metastasis. *Physical Biology*, 6(1):016008, 2009.

[72] Ignacio Ramis-Conde, Dirk Drasdo, Alexander R.A. Anderson, and Mark A.J. Chaplain. Modeling the influence of the e-cadherin-β-catenin pathway in cancer cell invasion: A multiscale approach. *Biophysical Journal*, 95(1):155 – 165, 2008.

[73] B. Ribba, K. Marron, Z. Agur, T. Alarcón, and P.K. Maini. A mathematical model of doxorubicin treatment efficacy for non-hodgkin's lymphoma: investigation of the current protocol through theoretical modelling results. *Bull Math Biol.*, 67(1):79–99, 2005.

[74] Bjarne Stroustrup. *The C++ Programming Language, Third Edition*. Addison-Wesley Longman Publishing Co., Inc., Boston, MA, USA, 3rd edition, 1997.

[75] Kristin R. Swanson, Russell C. Rockne, Jonathan Claridge, Mark A. Chaplain, Ellsworth C. Alvord, and Alexander R.A. Anderson. Quantifying the role of angiogenesis in malignant progression of gliomas: In silico modeling integrates imaging and histology. *Cancer Research*, 71(24):7366–7375, 2011.

[76] Michael D. Thompson and Satdarshan P. S. Monga. Wnt/β-catenin signaling in liver health and disease. *Hepatology*, 45(5):1298–1305, 2007.

[77] M. Tokoro. *Open systems science : from understanding principles to solving problems*. Amsterdam : IOS Press, 2010.

[78] Cyril Torre, Samira Benhamouche, Claudia Mitchell, Cécile Godard, Philippe Veber, Franck Letourneur, Nicolas Cagnard, Sébastien Jacques, Laetitia Finzi, Christine Perret, and Sabine Colnot. The transforming growth factor-α and cyclin d1 genes are direct targets of β-catenin signaling in hepatocyte proliferation. *Journal of Hepatology*, 55(1):86 – 95, 2011.

[79] Cyril Torre, Christine Perret, and Sabine Colnot. Transcription dynamics in a physiological process: β-catenin signaling directs liver metabolic zonation. *The International Journal of Biochemistry & Cell Biology*, 43(2):271 – 278, 2011. Directed Issue: Liver Growth, Development, and Disease – Dedicated to Robert Henry (Rob) Costa.

[80] Maria C. Villarroel, N.V. Rajeshkumar, Ignacio Garrido-Laguna, Ana De Jesus-Acosta, Sian Jones, Anirban Maitra, Ralph H. Hruban, James R. Eshleman, Alison Klein, Daniel Laheru, Ross Donehower, and Manuel Hidalgo. Personalizing cancer treatment in the age of global genomic analyses: Palb2 gene mutations and the response to dna damaging agents in pancreatic cancer. *Molecular Cancer Therapeutics*, 10(1):3–8, 2011.

[81] Karl Willert, Jeffrey D. Brown, Esther Danenberg, Andrew W. Duncan, Irving L. Weissman, Tannishtha Reya, John R. Yates, and Roel Nusse. Wnt proteins are lipid-modified and can act as stem cell growth factors. *Nature*, 423(6938):448–452, 05 2003.

[82] Olaf Wolkenhauer, Charles Auffray, Simone Baltrusch, Nils Blüthgen, Helen Byrne, Marta Cascante, Andrea Ciliberto, Trevor Dale, Dirk Drasdo, David Fell, James E Ferrell, Daniel Gallahan, Robert Gatenby, Ulrich Günther, Brian D Harms, Hanspeter Herzel, Christian Junghanss, Manfred Kunz, Ingeborg van Leeuwen, Philippe Lenormand, Francis Levi, Michael Linnebacher, John Lowengrub, Philip K Maini, Arif Malik, Katja Rateitschak, Owen Sansom, Reinhold Schäfer, Karsten Schürrle, Christine Sers, Santiago Schnell, Darryl Shibata, John Tyson, Julio Vera, Michael White, Boris Zhivotovsky, and Robert Jaster. Systems biologists seek fuller integration of systems biology approaches in new cancer research programs. *Cancer Res*, 70(1):12–13, Jan 2010.

[83] Wen Yang, He-Xin Yan, Lei Chen, Qiong Liu, Ya-Qin He, Le-Xing Yu, Shu-Hui Zhang, Dan-Dan Huang, Liang Tang, Xiao-Ni Kong, Chao Chen, Shu-Qin Liu, Meng-Chao Wu, and Hong-Yang Wang. Wnt/?-catenin signaling contributes to activation of normal and tumorigenic liver progenitor cells. *Cancer Research*, 68(11):4287–4295, 2008.